Since 1955

Strojniški vestnik
Journal of Mechanical Engineering

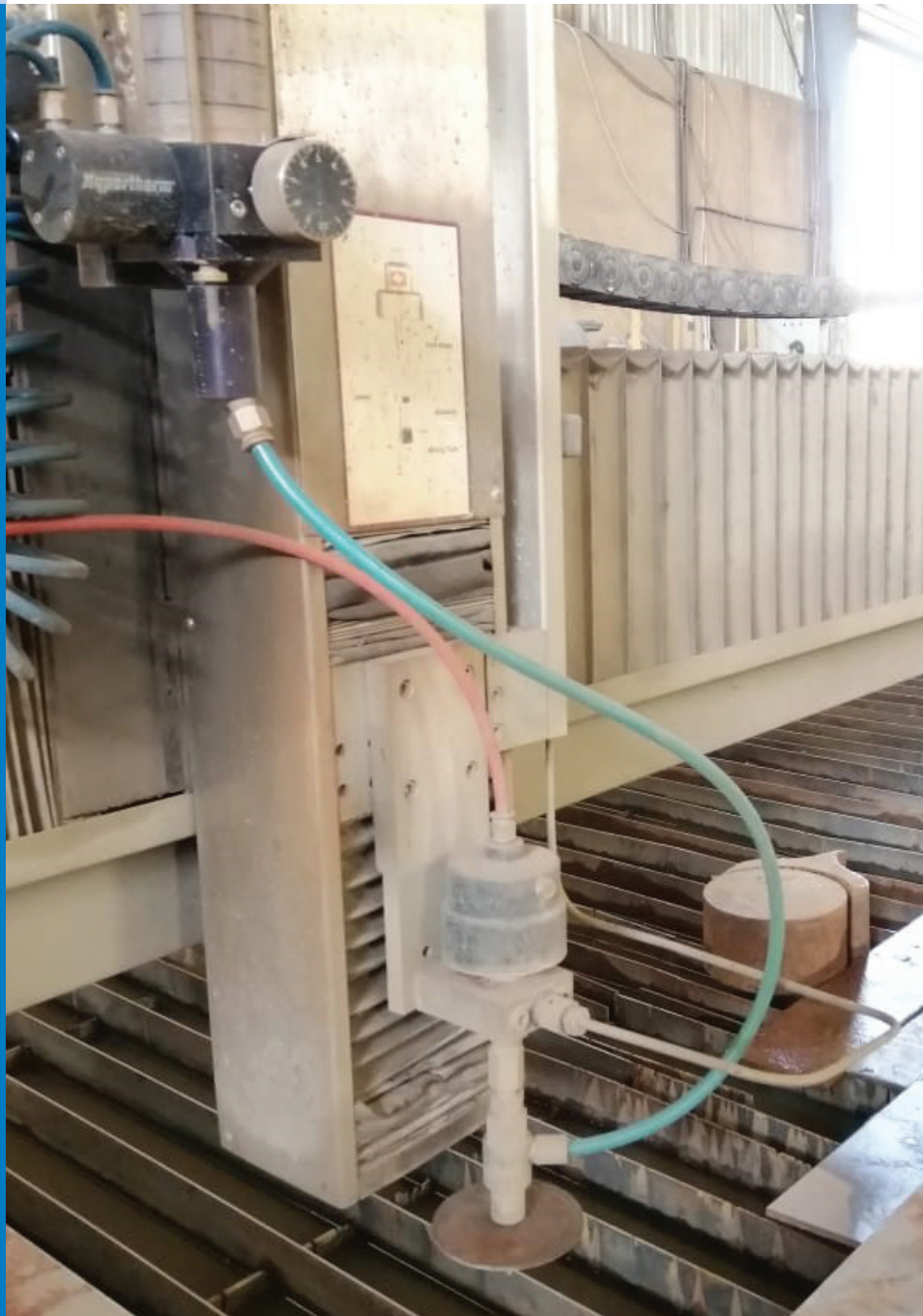

no. 4
year 2021
volume 67

Strojniški vestnik – Journal of Mechanical Engineering (SV-JME)

Aim and Scope
The international journal publishes original and (mini)review articles covering the concepts of materials science, mechanics, kinematics, thermodynamics, energy and environment, mechatronics and robotics, fluid mechanics, tribology, cybernetics, industrial engineering and structural analysis.
The journal follows new trends and progress proven practice in the mechanical engineering and also in the closely related sciences as are electrical, civil and process engineering, medicine, microbiology, ecology, agriculture, transport systems, aviation, and others, thus creating a unique forum for interdisciplinary or multidisciplinary dialogue.
The international conferences selected papers are welcome for publishing as a special issue of SV-JME with invited co-editor(s).

Editorial Office
University of Ljubljana, Faculty of Mechanical Engineering
SV-JME, Aškerčeva 6, SI-1000 Ljubljana, Slovenia
Phone: 386 (0)1 4771 137
Fax: 386 (0)1 2518 567
info@sv-jme.eu, http://www.sv-jme.eu

Print: Demat d.o.o., printed in 250 copies

Founders and Publishers
University of Ljubljana, Faculty of Mechanical Engineering, Slovenia
University of Maribor, Faculty of Mechanical Engineering, Slovenia
Association of Mechanical Engineers of Slovenia
Chamber of Commerce and Industry of Slovenia, Metal Processing Industry Association

Cover:
Abrasive water jet cutting machine. The cutting performed by an AWJ cutting machine (Jiangsu, China (Mainlan)) with ±0.1 mm of precision and repeatability. The maximum values of lateral speed and water pressure in this machine are
15 m/min and 200 MPa, respectively.

Image courtesy:
Al-Balqa Applied University, Al-Huson University College, Department of Mechanical Engineering, Jordan

General information
Strojniški vestnik – Journal of Mechanical Engineering is published in 11 issues per year (July and August is a double issue).

Institutional prices include print & online access: institutional subscription price and foreign subscription €100,00 (the price of a single issue is €10,00); general public subscription and student subscription €50,00 (the price of a single issue is €5,00). Prices are exclusive of tax. Delivery is included in the price. The recipient is responsible for paying any import duties or taxes. Legal title passes to the customer on dispatch by our distributor. Single issues from current and recent volumes are available at the current single-issue price. To order the journal, please complete the form on our website. For submissions, subscriptions and all other information please visit: *http://www.sv-jme.eu.*

You can advertise on the inner and outer side of the back cover of the journal. The authors of the published papers are invited to send photos or pictures with short explanation for cover content.

We would like to thank the reviewers who have taken part in the peer-review process.

ISSN 0039-2480, ISSN 2536-2948 (online)

The journal is subsidized by Slovenian Research Agency.

Strojniški vestnik - Journal of Mechanical Engineering is available on *https://www.sv-jme.eu.*

Contents

Strojniški vestnik - Journal of Mechanical Engineering
volume 67, (2021), number 4
Ljubljana, April 2021
ISSN 0039-2480

Published monthly

Papers

Strojniški vestnik - Journal of Mechanical Engineering 67(2021)4, 135-141
DOI:10.5545/sv-jme.2021.7141
Original Scientific Paper
Received for review: 2021-02-22
Received revised form: 2021-03-30
Accepted for publication: 2021-04-07

Studying the Performance of Cutting Carbon Fibre-Reinforced Plastic Using an Abrasive Water Jet Technique

Ahmed A. Hussien[1,*] – Isam Qasem[1] – Pramodkumar S. Kataraki[2] – Wael Al-Kouz[3] – Ayub Ahmed Janvekar[4]

[1] Al-Balqa Applied University, Al-Huson University College, Department of Mechanical Engineering, Jordan
[2] REVA University, School of Mechanical Engineering, India
[3] German Jordanian University, Department of Mechanical and Maintenance Engineering, Jordan
[4] VIT University, School of Mechanical Engineering, India

In recent years, composite materials such as carbon-fibre-reinforced plastic (CFRP) have been widely used in medical devices, industries, marine and aerospace applications due to their high resistance-to-weight ratio toughness, corrosion resistance, and other novel properties. The machining of these composite materials using conventional machines results in poor precision and surface finishing due to excess heat generation at the tool-material contact zone. The drawbacks of the conventional machining process can be overcome with the adoption of a novel cutting technique using pressurized water, which can dissipate the heat generated by the impact of abrasive particles against the material in order to eliminate the poor precision and surface finishing caused by overheating. In this experimental study, the performance of surface quality (roughness and kerf angle) of CFRP machining using an abrasive water jet technique has been studied for a wide range of cutting parameters, such as water pressure and cutting speed.

Keywords: composite materials, CFRP, abrasive water jet, surface quality, roughness, kerf angle

Highlights

- *An abrasive water jet (AWJ) technique can be used for machining composite materials such as carbon-fibre-reinforced plastic (CFRP).*
- *The roles of some cutting parameters, such as water pressure and cutting speed on surface quality have been studied.*
- *The enhancement of cutting surface quality depends on increasing water jet pressure and decreasing the cutting rate.*

0 INTRODUCTION

In recent years, carbon-fibre-reinforced plastic (CFRP) composite material has been utilized in various engineering and medical applications, such as the aerospace industry, renewable energy, medical devices, and the automotive industry [1]. The maximum utilization of CFRP has been due to their high strength with low weight, anti-corrosion and negligible effect on thermal expansion [2] and [3].

CFRPs are carbon/graphite fibres reinforced polymers. The polymers used in this composite can be epoxy, vinyl ester, polyester, or nylon. CFRPs are usually used in aerospace and automotive industries due to the superior properties, such as high specific strength and modulus, chemically stability, high corrosion and fatigue resistance, etc. [4].

Many researchers have been concerned about the difficulties of machining CFRP, especially thermal damage and low surface quality during manufacturing process [5] and [6]. The complexity of machining different materials' thermal and mechanical properties and the inhomogeneity and anisotropy of CFRPs influences the selection of the machining process and of the tools used. For example, cutting high strength and heat resistance of carbon fibres required a more hazardous environment and thermal-associated wear processes, which caused unexpected matrix crack and delamination [4]. Therefore, for enhancing the functional performance after machining CFRP, post-finishing processes include super-finishing, contour milling, honing, mass finishing, lapping, polishing, and drilling have been used. These processes required significant efforts and cost [7] and [8].

Therefore, advanced machining techniques using abrasive high-pressure water jet machining process are widely utilized to cut the high strength materials without thermal damage; this advanced machining technique is called abrasive water jet (AWJ). The main advantages of using AWJ in the manufacturing process are fewer recast layers, high cutting precision, and low cutting forces, and the lack of excess heat generated [9]. This machining technique has been adopted in production to process high-strength materials, such as stone, composite material, glass, etc. [10] to [12].

Manufacturing of the composite materials using conventional machining process faced many difficulties such as workpiece damage, crack formation in workpieces, and low surface finish quality. Thus, it has led to the utilization of abrasive water jet method to machine the composite materials [13] and [14].

*Corr. Author's Address: Al-Huson University College, Al-Balqa Applied University, Irbid, 21110, Jordan, ahmed.hussien@bau.edu.jo

To meet the expectations of best surface finish quality during manufacturing process using the AWJ technique, various parameters related to the quality of surface finish has been discussed. Bañon et al. [15] discussed in their comprehensive review the different defects generated on CRFP with AWJ machining. Damage caused by delamination, fibre fraying, degradation, or micro-cracks effects on the machining surface quality, which depends on the thickness of the material. In addition, macro-geometric deviations caused variations of kerf widths at three zones on the cutting surface, which produced taper angles. Therefore, many researchers have utilized experimental approaches to optimize these parameters for the best-expected surface finish quality results [16].

Popan and Popan [17] used the AWJ technique to manufacture a composite material containing many layers of CFRP. They studied and analysed the surface roughness surface quality and dimensional accuracy using a highly accurate microscope. Their experimental results after cutting the complex part reveals that using AWJ process in manufacturing composite materials is the best solution to avoid, tool wear, material mass delamination and abrasive inclusions.

Selvam et al. [18] investigated the performance in manufacturing the hybrid composite materials using AWJ technique. The hybrid composite materials containing 54 % e- glass fibres and carbon fibres manufactured with a hand lay-up method were used in experimental investigation. The study mainly focused on significant cutting parameters: water pressure, traverse speed, and abrasive mass flow rate on kerf taper angle and average surface roughness. The results showed that the traverse speed was a most important factor in obtaining high surface quality. This was due to the number of colliding and impact of abrasive particles with the side of the working material.

Xiao et al. [19] experimentally investigated the cutting quality of CFRP using a multi-pass of the AWJ technique. The composite material used in their experiment contained 60 % carbon-fibre with cross-ply at different angles. They evaluated the surface roughness, kerf taper angle and material mass delamination by changing the values of traverse speed, water pressure, and impact angle on multi-pass cutting using AWJ. They selected the values of traverse speed and water pressure at 1100 mm/min to 2300 mm/min and 180 MPa to 230 MPa, respectively. They concluded that the appropriate values of transverse speed and water pressure could improve the efficiency of surface quality. In addition, the modified AWJ machining can be applied to other materials, such as ceramic and metal.

The surface quality of the machining surface of hybrid structure that contains CFRP/Steel using AWJ have been examined by Bañon et al. [20]. There results showed that the lowest roughness and profile height of cutting surface accrues when hydraulic pressure of 420 MPa and a travel speed of 50 mm/min.

Unde et al. [21] asserted that the reinforcement orientations have a notable effect on surface quality in the manufacturing of CFRP composite materials using AWJ. They investigated the effect of surface methodology on surface quality during the machining process on composite materials. The results revealed that the lowest values of surface roughness occurred to the laminate with a fibre orientation of 90^{o} compared to 60^{o} and 45^{o}, which was due to lower shear plane resistance.

The literature mainly concentrated on studies to find the advantages of machining fibre-carbon-reinforced plastics using AWJ. However, the challenges of material delamination and surface quality still are based on different cutting parameters, including traverse speed, water flow rate, and water pressure in addition to the orientations and thickness of composite materials. Hence, greater research is necessary to find the optimum ranges of these parameters to meet the requirements of surface quality.

In this study, a hand lay-up of fabricated carbon-fibre-reinforced plastics at different orientation angles was subjected to abrasive water-jet machining in order to evaluate the surface roughness and kerf taper with a wide range of cutting parameters, including traverse speed and water pressure.

1 MATERIAL PREPARATION AND EXPERIMENTAL PROCEDURE

The work composite material is a carbon-fibre-reinforced plastic with a size of 300 mm × 300 mm × 7 mm. All the tested samples were manufactured using a hand lay-up based on a compression moulding method [22]. This method is very simple and gives an effective production of complex arrangement in short time.

The weight fraction of carbon fibres was 60 %, and the fibre orientations were 0°/90°/0°/90° for the all tested samples. Table 1 illustrates the materials of the tested samples.

Preparation was carried out in two stages; first, the mould was allowed to intake well-prepared resin mixture. Next, the fibre was placed over them carefully. This process was repeated continuously

in suitable interval of time gap. Once the required thickness was achieved, the stacking sequence was completed. The next stage was curing, in this CFRP laminates was exposed to pressure which is under compression mode. Dead weight was placed over the mould to bring necessary pressure.

Table 1. *The materials consist of tested samples* **[23]** *and* **[24]**

Material	Type	Properties	
Carbon fiber	Bidirectional (T300)	Nominal diameter [μm]	7
		Density [g/cm^3]	1.76
		Areal weight [g/m^2]	200
		Tensile strength [MPa]	3530
		Tensile modulus [GPa]	230
Epoxy resin	Araldite LY-556	Clear, Pale yellow liquid	
		Density at 25 °C [g/cm^3]	1.2
		Viscosity at 25 °C [Pa·s]	12
Hardener	Aradur HY-951	Viscosity at 25 °C [mPa·s]	10–20
		Density at 20 °C [g/cm^3]	0.95–1.05
		mixed to a ratio of 10:1 by weight	

The cutting was performed using an AWJ cutting machine (Jiangsu, China (Mainlan)) with ±0.1 mm of precision and repeatability (Fig. 1). The maximum values of lateral speed and water pressure in this machine are 15 m/min and 200 MPa, respectively. The values of process parameters were kept constant during the experiment as recommended by the manufacturer. The constant process parameter is shown in Table 2.

Fig. 1. *Abrasive water jet cutting machine*

The quality of the cutting surface obtained by AWJ machining process was examined and evaluated at different cutting parameters. The effect of different values of traverse speed and water pressure on kerf taper angle and surface roughness were investigated. Five different values of these parameters were taken into consideration for each measurement. The water pressure ranged from 100 MPa to 200 MPa while the traverse speeds ranged from 100 mm/min to 200 mm/min.

Table 2. *Constant process parameters*

Parameter	Value
Thickness, [mm]	7
Abrasive flow rate, [g/min]	300
Impinging angle, [deg]	90
Orifice diameter, [mm]	0.25
Stand off distance, [mm]	3
Abrasive type	Garnet #80
Abrasive grain size	80 mesh
Nozzle diameter, [mm]	0.79

Evaluating the surface quality of the surfaces produced during AWJ manufacturing can be done by measuring surface roughness and kerf taper angle. In this experiment, the surface roughness R_a value was measured using a portable roughness tester RT10 with measure range ±150 µm and resolution of 5 nm. According to Hloch and Valíček **[25]**, the cutting surface using AWJ generates three distinguished geometrical zones, namely the initial region, the surface cut (smooth zone), and the bottom (rough cutting region). These zones were related to many parameters includes material properties and cutting parameters. The output results of surface roughness of smooth cutting zone (maximum of 3 mm in the depth direction) were showed at various water jet parameters in a quantitative manner. The recorded value of every measurement was the mean of at least three repeated measurements.

Furthermore, the tapering effects in cutting zone at different values of cutting parameters is measured in this research. It can be characterized by measuring the upper and lower kerf width in the complete geometry of cutting, Eq. (1) **[26]**:

$$K_t = tan^{-1}\left(\frac{\left(w_{top} - w_{bottom}\right)\times 180}{2\pi t}\right), \qquad (1)$$

where K_t is a kerf taper angle [°], t is a material thickness [mm], w_{top} and w_{bottom} are top and bottom kerf width [mm], respectively.

Fig. 2 shows CFRP samples after the cutting process. The distance between each cutting line was at least 20 mm. The measurements were obtained at the middle of the cutting line to avoid the start cutting process on the material.

Fig. 2. *Illustrates CFRP material*

2 RESULTS AND DISCUSSION

This research aimed to investigate the effect of cutting parameters of AWJ machine on the surface quality of carbon FRPC material experimentally. The influence of cutting factors, namely traverse speed and water pressure on surface roughness and kerf taper, is discussed in this section. Also, R_a and kerf taper angle were measured for every cutting surface at different water pressure and traverse speed values.

The effect of traverse speed on kerf taper angle at lower and higher values of water pressure are introduced in Fig. 3. The experiment reveals that as traverse speed increased, the kerf ratio decreased for all water pressure values. This is due to the increase in the cutting rate, and this leads to a lesser affected of hitting particles during the cutting process, which caused the width of the kerf taper to decrease [27].

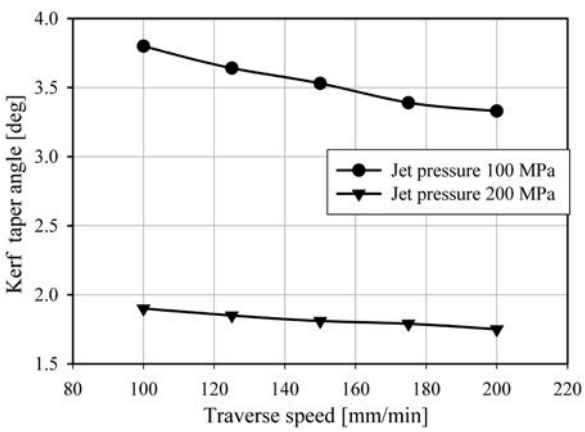

Fig. 3. *Kerf taper angle vs traverse speed at different water pressure levels*

On the other side, increasing the water pressure caused a decrease of the kerf taper angle, as shown in Fig. 3. In addition, the curve behaviour of different values of cutting speed is the same but at different magnitudes. Increasing the pressure of impinged particles leads to increased kinetic energy; this could be caused by reducing the kerf taper ratio [26]. Therefore, localized machining could be occurring at high velocity, and energy abrasive particles crash into the surface of CFRP composite materials. That caused a lower kerf width. Gnanavelbabu [28] observed lower kerf taper at high water pressure when machining aluminium metal matrix composites. The enhancement of kerf taper could be reached up to 50 % when the water pressure changed from 100 MPa to 200 MPa, as shown in Fig. 4. Minimizing the value of kerf taper angle is necessary to produce high quality cutting surface. Therefore, increasing both water pressure and cutting rate can be meet the required of manufacturing CFRP laminates at extraordinary quality. These results have been confirmed in previous research done by Vigneshwaran et al. [29]. They studied the effect of jet pressure on kerf taper angle during machining of red mud-filled sisal polyester hybrid composite using AWJ. They revealed that kerf taper reduced at higher pressure. From the Figs. 3 and 4, it is evident that the effect of changing water pressure on kerf taper is more significant of changing cutting rate.

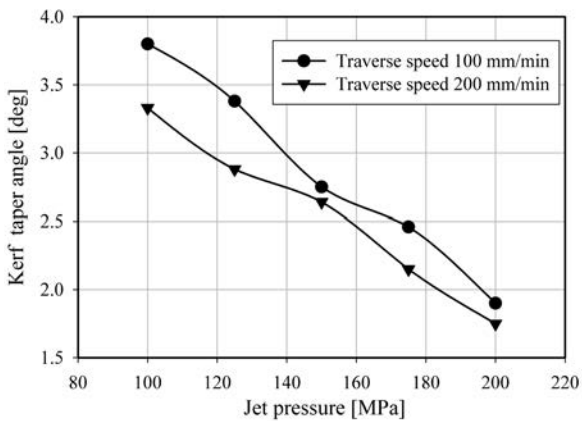

Fig. 4. *Kerf taper angle vs. water pressure at different traverse speed*

Fig. 5 illustrates the effect of surface roughness at different values of traverse speed at lowest and highest water pressure. It can be noted that increasing cutting rate caused increasing surface roughness. During the cutting process, the particles of hardener materials become unstable, especially at a high cutting rate. This leads to observe irregular holes and cavities on the cutting surfaces [30]. Thus, increasing the speed of machining CFRP laminates causes high surface roughness. Pahuja and Ramulu [31] showed that increasing cutting rate caused high surface roughness regardless of the stacking configuration. This is due to the loss of kinetic energy. However, the surface roughness can be enhanced by increasing the water

pressure as shown in Fig. 6. The results reveal that, at high water pressure, collisions between high-energy water particles and composite materials caused high erosions with fewer cavitation and waviness patterns on the cutting surfaces [28].

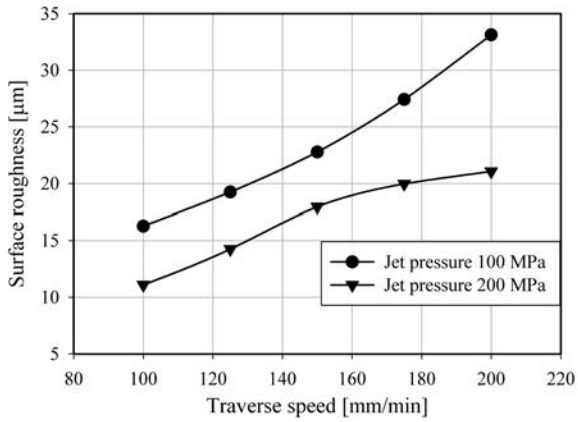

Fig. 5. *Surface roughness vs. traverse speed at different water pressure*

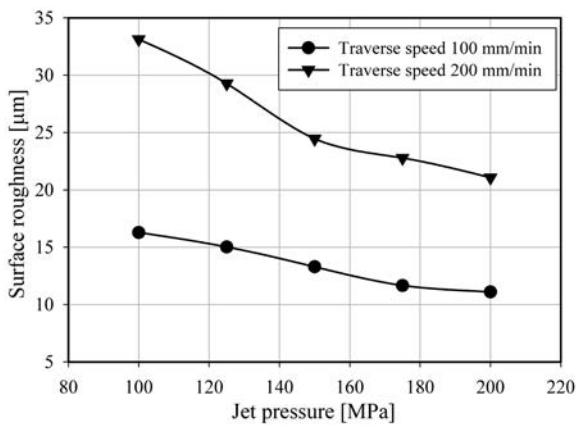

Fig. 6. *Surface roughness vs. water pressure at different traverse speed*

Finally, correlations were produced based in experimental results to predict the surface roughness and kerf taper angle by changing the values of water pressure and cutting rate. The curve-fitting toolbox of MATLAB was utilized to find the relationship between independent input process parameters and the experimental responses. A second-order polynomial curve-fitting model was selected based on previous research done by [5] and [32]. The regression models have acceptable ranges of the sum of square regression, the sum of square error, and root mean square error. The predicted correlations of surface roughness and kerf taper angle, with the goodness-of-fit variables were shown in Eqs. (2) and (3), respectively:

$$R_a = 8.895 + 0.2039T_s - 0.1254W_P + 6.876\times10^{-5}T_s^2 - 6.45\times10^{-4}T_sW_P + 5.015\times10^{-5}W_P^2. \quad (2)$$

The sum of squared errors, SSE = 10.22, *R*-square = 0.9835, adjusted *R*-square = 0.9753, and root mean square error, *RMSE* = 1.011.

$$K_t = 6.643 - 0.01214T_s - 0.02053W_P + 1.319\times10^{-5}T_s^2 + 3.45\times10^{-5}T_sW_P - 5.634\times10^{-6}W_P^2. \quad (3)$$

SSE = 0.03247, *R*-square = 0.9961, Adjusted *R*-square = 0.9942, and RMSE = 0.05698, where R_a, K_t, T_S and W_P are surface roughness, kerf taper angle, traverse speed, and water pressure, respectively.

The realistic correlations in Models 2 and 3 can adequately predict the surface roughness and kerf taper angle, respectively. The considering experimental values of water pressure and traverse speed and predicted values for Eqs. (2) and (3) are shown in Figs. 7 and 8, respectively.

It can be noted from Fig. 7 that the minimum value of R_a occurred at the highest water pressure (200 MPa) and the lowest traverse speed (100 mm/min). This is due to the rise of kinetic energy, which caused concentrated breakage forces for carbon fibre as well as polymer matrix in a relatively long time of cutting [18].

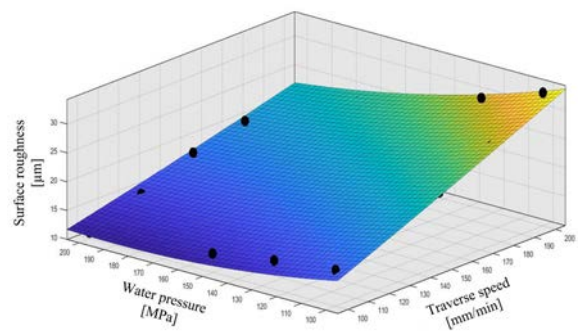

Fig. 7. *Surface roughness with traverse speed and water pressure*

The 3D graph of kerf taper angle with water pressure and traverse speed is shown in Fig .8. This figure illustrates that the relations between kerf taper and traverse speed is directly proportional, while the effect of water pressure to kerf taper angle is indirectly proportional, because the increasing cutting rate caused less contact time between the cutting process and CFRP, which means less delamination of the cutting material [26].

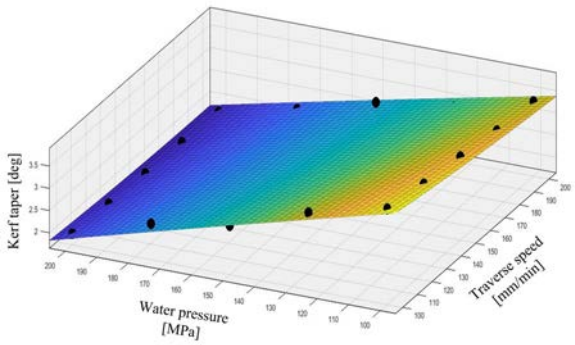

Fig. 8. *Kerf taper with traverse speed and water pressure*

3 CONCLUSIONS

In this experimental research, hand lay-up of fabricated CFRP at different orientation angles was subjected to AWJ machining. The effects of water jet pressure and traverse speed on surface roughness and kerf taper angle were studied. The results reveal that these cutting parameters have an important role in reaching the desired surface quality. The investigated cutting area was in the middle of the cut surface at different locations (smooth zone). Both the surface roughness and kerf taper could be enhanced with increasing water jet pressure and decreasing the cutting rate. Mainly, this is due to the effect of the kinetic energy observed from impinged particles and the structure of CFRP. Increasing the jet pressure caused increased pressure to increase its kinetic energy while increasing traverse speed caused loss of kinetic energy. Second-order polynomial curve-fitting models were produced using MATLAB regression analysis to predict the surface roughness and kerf taper angle within the range of experimental values of water pressure and cutting rate. Future objectives of the presented work will be focused on larger sets of experimental data and investigation with multiple variables. In addition, relevant information shall be added by enabling various parameters, such as stand-off distance and abrasive grain size.

4 REFERENCES

[1] Geier N., Davim J.P., Szalay T. (2019). Advanced cutting tools and technologies for drilling carbon fibre reinforced polymer (CFRP) composites: A review. *Composites Part A: Applied Science and Manufacturing*, vol. 125, art. ID 105552, **DOI:10.1016/j.compositesa.2019.105552**.

[2] Krishnaraj, V., Prabukarthi, A., Ramanathan, A., Elanghovan, N., Kumar, M.S., Zitoune, R., Davim, J. (2012). Optimization of machining parameters at high speed drilling of carbon fiber reinforced plastic (CFRP) laminates, *Composites Part B: Engineering*, vol. 43, no. 4, p. 1791-1799, **DOI:10.1016/j.compositesb.2012.01.007**.

[3] Popan, I.A., Balc, N., Popan, A., Carean, A. (2018). Experimental study on reverse engineering in case of composite materials cut by water jet cutting. *MATEC Web of Conferences*, vol. 178, art. ID 03004, **DOI:10.1051/matecconf/201817803004**.

[4] Che, D., Saxena, I., Han, P., Guo, P., Ehmann, K.F. (2014). Machining of carbon fiber reinforced plastics/polymers: a literature review. *Journal of Manufacturing Science and Engineering*, vol. 136, no. 3, **DOI:10.1115/1.4026526**.

[5] Bañon, F., Sambruno, A., Batista, M., Simonet, B., Salguero, J. (2020). Study of the surface quality of carbon fiber–reinforced thermoplastic matrix composite (CFRTP) machined by abrasive water jet (AWJM). *The International Journal of Advanced Manufacturing Technology*, vol. 107, p. 3299-3313, **DOI:10.1007/s00170-020-05215-y**.

[6] Thakur, R., Singh, K.K. (2020). Abrasive water-jet machining of fiber-reinforced composites: A state-of-the-art review. *Journal of the Brazilian Society of Mechanical Sciences and Engineering*, vol. 42, art. ID 381, **DOI:10.1007/s40430-020-02463-7**.

[7] Ruiz-Garcia, R., Mayuet Ares, P.F., Vazquez-Martinez, J.M., Salguero Gómez, J. (2019). Influence of abrasive waterjet parameters on the cutting and drilling of CFRP/UNS A97075 and UNS A97075/CFRP stacks. *Materials*, vol. 12, no. 1, art. ID 107, **DOI:10.3390/ma12010107**.

[8] Hashimoto, F., Chaudhari, R.G., Melkote, S.N. (2016). Characteristics and performance of surfaces created by various finishing methods. *Procedia CIRP*, vol. 45, p. 1-6, **DOI:10.1016/j.procir.2016.02.052**.

[9] Mayuet Ares, P.F., Girot Mata, F., Batista Ponce, M., Salguero Gómez, J. (2019). Defect analysis and detection of cutting regions in CFRP machining using AWJM. *Materials*, vol. 12, no. 24, art. ID 4055, **DOI:10.3390/ma12244055**.

[10] Natarajan, Y., Murugesan, P.K., Mohan, M., Khan, S.A.L.A. (2020). Abrasive water jet machining process: A state of art of review. *Journal of Manufacturing Processes*, vol. 49, p. 271-322, **DOI:10.1016/j.jmapro.2019.11.030**.

[11] Kmec, J., Gombár, M., Harničárová, M., Valíček, J., Kušnervá, M., Kříž, J., Kadnár, M., Karková, M., Vagaská, A. (2020). The predictive model of surface texture generated by abrasive water jet for austenitic steels. *Applied Sciences*, vol. 10, no. 9, art. ID 3159, **DOI:10.3390/app10093159**.

[12] Naresh Babu, M., Muthukrishnan, N. (2014). Investigation on surface roughness in abrasive water-jet machining by the response surface method. *Materials and Manufacturing Processes*, vol. 29, no. 11-12, p. 1422-1428, **DOI:10.1080/10426914.2014.952020**.

[13] Vigneshwaran, S., Uthayakumar, M., Arumugaprabu, V. (2018). Abrasive water jet machining of fiber-reinforced composite materials. *Journal of Reinforced Plastics and Composites*, vol. 37, no. 4, p. 230-237, **DOI:10.1177/0731684417740771**.

[14] Dandekar, C.R., Shin, Y.C. (2012). Modeling of machining of composite materials: a review. *International Journal of Machine Tools and Manufacture*, vol. 57, p. 102-121, **DOI:10.1016/j.ijmachtools.2012.01.006**.

[15] Bañon, F., Sambruno, A., González-Rovira, L., Vazquez-Martinez, J.M., Salguero, J., (2021). A review on the abrasive

water-jet machining of metal–carbon fiber hybrid materials. *Metals*, vol. 11, no. 1, art. ID 164, **DOI:10.3390/met11010164**.

[16] Eneyew, E.D., Ramulu, M. (2014). Experimental study of surface quality and damage when drilling unidirectional CFRP composites. *Journal of Materials Research and Technology*, vol. 3, no. 4,p. 354-362, **DOI:10.1016/j.jmrt.2014.10.003**.

[17] Popan, I.A., Popan, A. (2017). Experimental study on manufacturing complex parts from composite materials using water jet cutting. *Acta Technica Napocensis Series: Applied Mathematics, Mechanics, And Engineering*, vol. 60, no. 2, p. 251-254.

[18] Selvam, R., Karunamoorthy, L., Arunkumar, N. (2017). Investigation on performance of abrasive water jet in machining hybrid composites. *Materials and Manufacturing Processes*, vol. 32, no. 6, p. 700-706, **DOI:10.1080/10426914.2016.1198039**.

[19] Xiao, S., Wang, P., Gao, H., Soulat, D. (2019). A study of abrasive water-jet multi-pass cutting on kerf quality of carbon fiber-reinforced plastics. *The International Journal of Advanced Manufacturing Technology*, vol. 105, no. 11, p. 4527-4537, **DOI:10.1007/s00170-018-3177-1**.

[20] Bañon, F., Simonet, B., Sambruno, A., Batista, M., Salguero, J. (2020). On the surface quality of CFRTP/Steel hybrid structures machined by AWJM. *Metals*, vol. 10, no. 7, art .ID 983, **DOI:10.3390/met10070983**.

[21] Unde, P.D., Gayakwad, M., Patil, N., Pawade, R., Thakur, D., Brahmankar, P. (2015). Experimental investigations into abrasive water-jet machining of carbon fiber reinforced plastic. *Journal of Composites*, vol. 2015, art. ID 971596, **DOI:10.1155/2015/971596**.

[22] Prasad, V., Hunize, C.M., Abhiraj, R., Jospeh, M., Sekar, K., Ali, M. (2019). Mechanical properties of flax fiber reinforced composites manufactured using hand lay-up and compression molding—a comparison. *Advances in Industrial and Production Engineering*, p. 781-789, **DOI:10.1007/978-981-13-6412-9_72**.

[23] Priya, I.I.M., Vinayagam, B. (2018). Enhancement of bi-axial glass fibre reinforced polymer composite with graphene platelet nanopowder modifies epoxy resin. *Advances in Mechanical Engineering*, vol. 10, no. 8, **DOI:10.1177/1687814018793261**.

[24] Muralidhara, B., Babu, S.K., Suresha, B. (2020). The effect of fiber architecture on the mechanical properties of carbon/epoxy composites. *Materials Today: Proceedings*, vol. 22, part. 4, p. 1755-1764, **DOI:10.1016/j.matpr.2020.03.008**.

[25] Hloch, S., Valíček, J. (2012). Topographical anomaly on surfaces created by abrasive water-jet. *The International Journal of Advanced Manufacturing Technology*, vol. 59, p. 593-604, **DOI:10.1007/s00170-011-3511-3**.

[26] Jagadeesh, B., Dinesh Babu, P., Nalla Mohamed, M., Marimuthu, P. (2018). Experimental investigation and optimization of abrasive water jet cutting parameters for the improvement of cut quality in carbon fiber reinforced plastic laminates. *Journal of Industrial Textiles*, vol. 48, no. 1, p. 178-200, **DOI:10.1177/1528083717725911**.

[27] Wang, J., Wong, W. (1999). A study of abrasive water-jet cutting of metallic coated sheet steels. *International Journal of Machine Tools and Manufacture*, vol. 39, no. 6, p. 855-870, **DOI:10.1016/S0890-6955(98)00078-9**.

[28] Gnanavelbabu, A., Rajkumar, K., Saravanan, P. (2018). Investigation on the cutting quality characteristics of abrasive water jet machining of AA6061-B4C-hBN hybrid metal matrix composites. *Materials and Manufacturing Processes*, vol. 33, no. 12, p. 1313-1323, **DOI:10.1080/10426914.2018.1453146**

[29] Vigneshwaran, S., Uthayakumar, M., Arumugaprabu, V. (2020). Prediction and analysis of abrasive water jet machining performance on hybrid composite. *Journal of Testing and Evaluation*, vol. 48, no. 2, p. 1505-1519, **DOI:10.1520/JTE20180593**.

[30] Karabulut, Ş., Karakoç, H., Çıtak, R. (2016). Influence of B4C particle reinforcement on mechanical and machining properties of Al6061/B4C composites. *Composites Part B: Engineering*, vol. 101, p. 87-98, **DOI:10.1016/j.compositesb.2016.07.006**.

[31] Pahuja, R., Ramulu, M., (2019). Surface quality monitoring in abrasive water jet machining of Ti6Al4V–CFRP stacks through wavelet packet analysis of acoustic emission signals. *The International Journal of Advanced Manufacturing Technology*, vol. 104, no. 9, p. 4091-4104, **DOI:10.1007/s00170-019-04177-0**.

[32] Wong, I.M.M., Azmi, A., Lee, C.C., Mansor, A.F. (2018). Kerf taper and delamination damage minimization of FRP hybrid composites under abrasive water-jet machining. *The International Journal of Advanced Manufacturing Technology*, vol. 94, p. 1727-1744, **DOI:10.1007/s00170-016-9669-y**.

Strojniški vestnik - Journal of Mechanical Engineering 67(2021)4, 142-152,

DOI:10.5545/sv-jme.2020.7017 Original Scientific Paper
Received for review: 2020-10-28
Received revised form: 2021-02-01
Accepted for publication: 2021-02-15

HIL Evaluation of a Novel Real-time Energy Management System for an HEV with a Continuously Variable Transmission

Amir Taghavipour* – Ali Alipour
K. N. Toosi University of Technology, Faculty of Mechanical Engineering, Iran

One of the most important challenges facing automotive engineers is reducing vehicle fuel consumption and improving the drivability index. Modern hybrid electric powertrains play an important role in reducing fuel consumption. Continuously variable transmission (CVT) is an automatic transmission that can change the gear ratio seamlessly using a belt and pulleys. CVT performs with infinite gear ratios. Controlling and determining the optimal gear ratio, especially in a complex hybrid powertrain, is a major challenge. Therefore, a multi-parametric model predictive controller with real-time implementation capability is proposed that can handle the energy management task concurrently with gear shifting strategy in a parallel pre-transmission hybrid electric vehicle. The proposed controller hardware-in-the-loop (HIL) validation procedure on the high-fidelity Autonomie model shows significant improvement in fuel economy while maintaining drivability in three different driving schedules. HIL evaluation guarantees the real-time capability and the proposed controller readiness to be implemented to real-world control hardware.

Keywords: hybrid electric vehicle, continuously variable transmission (CVT), Autonomie, energy management system, explicit model predictive control, hardware in the loop

Highlights

- *Proposing a novel control-oriented model for hybrid electric powertrain with a continuously variable transmission.*
- *Developing an optimal energy management system via an explicit model predictive control approach.*
- *Hardware-in-the-loop testing via an experimentally-validated high-fidelity model to represent the real-time capability of the proposed controller.*

0 INTRODUCTION

With the growing environmental concerns about global warming and shortages of global fuel reserves, every possible solution to reduce transportation energy consumption has become a key element in researchers' current debate. Vehicles' fuel consumption plays a crucial role in determining the emission of greenhouse gases from the transportation sector. As a result, vehicles have been increasingly facing stringent emissions and fuel economy standards, which are driven by regulatory and market forces. Among the proposed solutions to improve the efficiency of conventional powertrains, continuously variable transmission (CVT) has been commercialized. A CVT changes gear ratios seamlessly between desired limits, which consequently enhances the fuel economy and dynamic performance of a vehicle by better matching the engine operating conditions to the variable driving scenarios.

In contrast, powertrain electrification has also proven to be an effective solution to the aforementioned problems. New opportunities are expected to appear by using CVT with a hybrid electric powertrain, although the controls design complexity can be a potential drawback. For those hybrid architectures whose internal combustion engine is connected to the wheels, a separate transmission controls the engine operation. Except for the series powertrains, the internal combustion engine (ICE) is controlled mechanically or electrically. For complex hybrid structures, a second electric machine (apart from the traction electric motor) plays a pivotal rule in controlling the engine. Since those drivetrains theoretically provide infinite ranges of imaginary gear ratios, they are called electrical continuously variable transmission (eCVT). However, in most commercialized parallel architectures, a mechanical gearbox such as automatic or dual-clutch transmission regulates the engine status. By replacing those conventional transmissions with a CVT, more flexibility for fuel economy and emissions improvement is provided. However, a sophisticated control scheme should be available to exploit the mentioned flexibility fully.

Among different approaches for control design, model-based methods seem to be promising. In contrast to heuristic methods, they can reduce the time and cost of the control development procedure, and their performance and optimality can be guaranteed for different scenarios facing the powertrain. One of the challenges of using model-based approaches is deriving an appropriate control-oriented model that is simultaneously simple and adequately accurate.

*Corr. Author's Address: K. N. Toosi University of Technology, Address, Tehran, Iran, ataghavi@uwaterloo.ca

The accuracy of the control-oriented model in terms of capturing the essential dynamics of the system contributes to the controller's performance. However, the higher levels of accuracy require more dynamics and, consequently, larger models. These larger models may require more computational time and complexity, which are contradicting factors in the real-time implementation of the controller. Therefore, we should keep the control-oriented model simple enough to maintain the controller's computational burden at a very low level. This trade-off turns out to be the most demanding bottleneck of designing a model-based controller. Acquiring such a model along with a model-based optimal controller that can be implemented in real-time remains a challenge, which we focus on in this research. The development of an optimum CVT control strategy is not an easy task, owing to two partially opposite features that have to be satisfied: The reduction of fuel consumption and the requirement of appropriate drivability/acceleration performance which is dependent on the torque capacity of the CVT system. Accurate and fast control of the rate of speed ratio change is a prerequisite for meeting these goals. Pfiffner and Guzzella [1] have investigated the optimal fuel consumption performance of a vehicle equipped with a CVT under steady and transient conditions. Three basic modes for optimal control are introduced, and then the optimal performance conditions are calculated by defining the optimization problem to reduce specific fuel consumption, inputs of load and pedal functions and gear ratio change. The results showed that the optimization procedure improved fuel economy by 4 % for the supercharged engine and 6 % for the spark-ignition engine. Hatakana et al. [2] presented the receding horizon control strategy and introduced this controller as a new control scheme without the need for a control map in order to determine the gear ratio for the CVT system. For this purpose, two spraying and non-spraying modes were considered, and the equations of these two engine states were obtained. Kazemi et al. [3] investigated the optimal gear ratios for the modelled CVT system using nonlinear optimal control rules. They presented a model of the power transmission system and its subsystems. Then, by defining the optimization problem, the optimal gear ratios were calculated, and a fuel consumption reduction of 11 % was reported. However, the real-time implementation issues remained unaffected. Yildiz and Kopmaz [4] have carefully studied the dynamics of CVT and developed a control-oriented model, which has been validated via a test rig in order to design appropriate controller for shifting. Bemporad et al. [5] have proposed a supervisory controller for a powertrain with a CVT transmission, which is scheduled for production by General Motors. The control strategy is an online model predictive control (MPC) that determines the engine torque and CVT track the demanded torque by the driver for improving the fuel economy. Based on extensive in-vehicle testing, the supervisory controller proved to be robust to different environmental conditions and driving manoeuvres. Tao et al. [6] have proposed and hardware-in the loop (HIL) validated control strategy for a CVT transmission and shown the sensitivity of throttle opening and vehicle speed to ratio control; consequently, its fluctuation can be reduced dramatically. All those achievements are contributing to efficiency improvement and jerk reduction. In addition to those studies, various investigations have been carried out to control this gearbox by using various controls, such as proportional–integral–derivative (PID) [7], linear–quadratic regulator (LQR) [8], fuzzy control [9], backstepping control [10].

As for CVT-based hybrid vehicles, Hofman et al. [11] investigated the sizing problem of electric machine for a hybrid vehicle equipped with a CVT regarding the best fuel economy. By studying the parameters of the model, they have developed a quick simulation platform, which is suitable for control design purposes. Ji et al. [12] have proposed a real-time energy management strategy for a CVT-based parallel hybrid electric vehicle. By using AVL-Cruise software as their simulation platform, they could improve the fuel economy by 1.9 % based on an urban dynamometer driving schedule (UDDS). Tang et al. [13] have proposed a Gauss pseudo-spectral MPC strategy for a parallel CVT-based HEV and validated the scheme on a new European drive cycle (NEDC), which shows promising improvement in fuel economy. Li et al. [14] have proposed a strategy for such a powertrain by using the rules from the dynamic programming solution. They also extend their studies on the equivalent consumption minimization strategy (ECMS) implementation on CVT-based HEV and compared the resulted fuel economy based on different ultimate battery states of charge for different drive cycles [15]. Similar studies have been conducted recently for CVT-based plug-in hybrid electric vehicles (PHEVs), which admits the growing attention to find an ultimate solution for controls development. Wang and Frank proposed a control scheme for a CVT-based PHEV indicates that in order to achieve the global optimum, energy management system (EMS) and gear shifting strategy should be done simultaneously [16]. Li et al. [14] have

studied multiple optimal gear-shifting strategies by considering hydraulics and mechanical loss of CVT for a CVT-based PHEV.

The challenge faced by this research is to obtain a simple and adequately accurate control-oriented model for a real-time implementable model-based controller that can handle energy management and CVT gear shifting at the same time. To outperform the other proposed controllers, this approach should be optimal with a minimal computational burden. Thus, we propose a multi-parametric model predictive approach to develop an energy management system for a CVT-based parallel HEV to improve fuel economy further, while maintaining drivability indices and, more importantly, real-time implementation capability of the controller. This controller performance will be validated with the dSPACE HIL platform along with high-fidelity experimentally-validated Autonomie model of the mentioned powertrain through three different driving cycles. The results suggest a considerable improvement in fuel economy compared to the baseline controller and mentioned studies, while the HIL evaluation guarantees the real-time capability and the proposed controller readiness to be implemented to real-world control hardware.

First, the control-oriented model is introduced. Then a brief description of the high-fidelity Autonomie model whose parameters are derived based on the experimental data is delivered. In Section 2, the control design procedure is detailed. and then a brief specification of the HIL platform is presented. Next, the results of the simulation are discussed. Section 5 concludes the article.

1 MODELLING

The performance of a model-based controller is highly dedicated to the dynamics that are included inside it. However, an accurate model can be of higher orders, which imposes a significant computational load on the controller. Thus, the model should be sufficiently simple and accurate to be useful for the development of controls. The trade-off between simplicity and accuracy of the control-oriented model determines the performance and real-time capability of the controller. During the controller development procedure, it should go through multiple virtual simulation stages until it can be qualified to be implemented on the real plant. To this end, a valid simulation platform should be provided at the early stages, so that the controller performance can be tested beforehand, and its issues and flows are revisited and resolved. In this section, we introduce the control-oriented model of the powertrain and then review the experimentally-validated simulation model that is to be used in our HIL procedure.

1.1 Control-oriented Model

As mentioned above, acquiring a simple yet sufficiently accurate control-oriented model is an important step in designing a model-based controller. Here, we introduce a control-oriented model that represents the complexity of the hybrid powertrain, but it only contains the essential dynamics of it according to Eq. (1). The first equation determines the battery dynamics in its simplest shape. The high-voltage battery state of charge (SOC) will be determined by the current drawn from it and its total capacity. Since the traction motor torque is approximately proportional to its current, we can find a way to rewrite this equation with traction motor torque (($T_m = k_m I$)). The second equation is based on the vehicle longitudinal dynamics. In this equation, the engine, traction motor, and brake torque along with CVT ratio determine the variation of the vehicle velocity.

$$\begin{cases} \dot{SOC} = -\dfrac{I}{Q} = -\dfrac{T_m}{k_m Q} \\ \dot{V} = \dfrac{1}{mr_w}\left\{\eta_{cvt}\eta_{DL} i_{FD} i_{cvt}\left(T_m + T_e\right) - T_b\right\} \\ \quad -\dfrac{\rho c_D A_f V^2}{2m} - f_r g \end{cases}, \quad (1)$$

where T_m, T_e *and* T_b are the electric motor, engine, and mechanical brake torque, respectively along with i_{cvt} as the CVT ratio constitute the manipulated inputs. *SOC* and *V* are battery state of charge and vehicle velocity that are the problem state variables. The incorporated parameters are as follows: Q, k_m, m, δ, r_w, η_{cvt}, η_{DL}, i_{FD}, ρ, c_D, A_f, f_r, and g are battery capacity, electric motor coefficient, vehicle mass, rotational inertias equivalent coefficient, wheel effective radius, CVT efficiency, driveline efficiency, final drive ratio, air density, drag coefficient, vehicle frontal area, rolling friction coefficient and gravity constant, respectively.

Although the original nature of these equations is nonlinear, according to Eq. (1), we can approximate them with their linear counterparts around any possible operating point (Eq. (2)).

$$\begin{bmatrix} S\dot{O}C \\ \dot{V} \end{bmatrix} = \begin{bmatrix} 0 & 0 \\ 0 & -\dfrac{\rho c_D A_f \hat{V}}{2m} \end{bmatrix} \begin{bmatrix} SOC \\ V \end{bmatrix} + \begin{bmatrix} -\dfrac{1}{k_m Q} & 0 & 0 & 0 \\ \dfrac{\eta_{cvt}\eta_{DL} i_{FD} \hat{i}_{cvt}}{mr_w} & \dfrac{\eta_{cvt}\eta_{DL} i_{FD} \hat{i}_{cvt}}{mr_w} & \dfrac{\eta_{cvt}\eta_{DL} i_{FD}}{mr_w}\left(\hat{T}_m + \hat{T}_e\right) & -\dfrac{1}{mr_w} \end{bmatrix} \begin{bmatrix} T_m \\ T_e \\ i_{cvt} \\ T_b \end{bmatrix} + \begin{bmatrix} 0 \\ \dfrac{\eta_{cvt}\eta_{DL} i_{FD} \hat{i}_{cvt}}{mr_w}\left(\hat{T}_m + \hat{T}_e\right) + \dfrac{\rho c_D A_f \hat{V}^2}{2m} - f_r g \end{bmatrix}, \quad (2)$$

where $\hat{V}$, $\hat{T}_m$, $\hat{T}_e$, and $\hat{i}_{cvt}$ are the state variable and input at any operating point. The parameters values are listed in Table 1.

Table 1. *Key parameters value*

Parameter	Description	Value
Q	Battery capacity [Ah]	6.53
k_m	Motor torque constant [N·m/A]	0.04
m	Vehicle mass [kg]	1700
r_w	Wheel effective radius [m]	0.35
η_{cvt}	CVT efficiency	0.95
η_{DL}	Driveline efficiency	0.9
i_{FD}	Final drive ratio	6.39
ρ	Air density [kg/m³]	1.4
c_D	Drag coefficient	0.35
A_f	Vehicle frontal area [m²]	3.2
f_r	Rolling resistance coefficient	0.01
g	Gravity acceleration [m/s²]	9.81
$T_{m,\max}$	Motor maximum torque [Nm]	160
$T_{m,\min}$	Motor minimum torque [Nm]	-160
$T_{e,\max}$	Engine maximum torque [Nm]	207
$T_{e,\min}$	Engine minimum torque [Nm]	0
$i_{cvt,\max}$	CVT maximum ratio	2.5
$i_{cvt,\min}$	CVT minimum ratio	0.5
$T_{b,\max}$	Brake maximum torque [Nm]	6000
$T_{b,\min}$	Brake minimum torque [Nm]	0

1.2 Simulation Model

A schematic of the CVT-based parallel hybrid electric vehicle in Autonomie software is shown in Fig 1. The advantage of the Autonomie platform over similar softwares is that it offers a sophisticated model of different powertrains derived from Argonne National Lab test procedures and its capability to be used for performing HIL tests.

According to Fig. 1, the internal combustion engine (ICE) is connected to a traction motor (MOT), which is powered by the high-voltage battery (HVB) via an electrical coupling (ED). Then the output shaft of the power plant is connected to the CVT. The CVT magnifies the torque and transfers it to the final drive (FD) via a mechanical coupling (CP), which drives the vehicle (VM) by the wheels (WH). The vehicle accessories load (ACC) is also considered in the vehicle model. The engine model consists of look-up tables, which are validated based on the experiments. The high-voltage battery is based on a dual polarization circuit, whose parameters are tuned to be as close as possible to the real powertrain. The traction motor is loaded with the efficiencies and possible losses to mimic a realistic electric drive and the CVT module. Each of these components have their own low-level controllers, which will not be altered in this study. The supervisory controller determines the power split between the engine and the traction motor for propelling the vehicle, as well as CVT ratio.

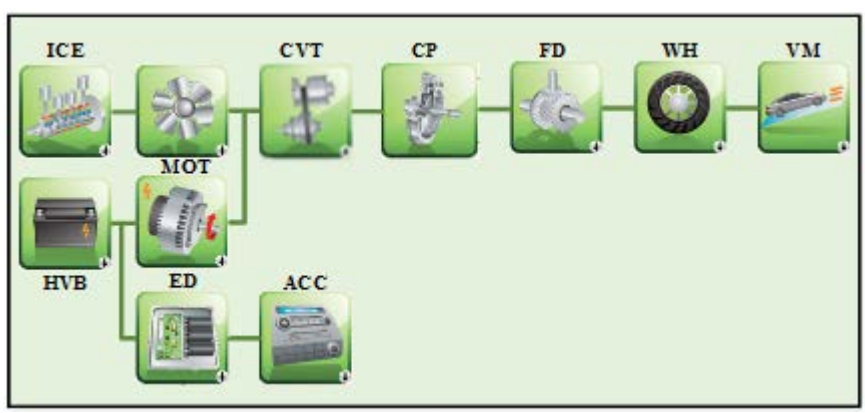

Fig. 1. *Schematic of Autonomie high-fidelity model of a parallel HEV with CVT*

We will bypass the baseline high-level controller and connect the wires to our proposed controller.

2 ENERGY MANAGEMENT SYSTEM

Once the control-oriented model is obtained, the energy management system can be designed. The MPC approach has drawn a great deal of attention in among the relevant researchers and industries. MPC has an almost unique ability to handle hard constraints on control and states during its design procedure. It can predict the behaviour of the system at specified time intervals at the future instance via the control-oriented model [17]. MPC merges the efficiency of an optimal control approach and the robustness of a feedback controller. However, the MPC approach has its own limits and challenges. The key drawback of this approach is its computational burden. However, the solver involved in solving the required optimization problem might be unreliable and bulky for naive control hardware in automotive applications. Those two are considered to be serious problems of MPC in real-time systems. Fortunately, there are solutions to those shortcomings. The computational burden can be alleviated by multi-parametric optimization approaches, which solve the problem offline and results in some affine functions of the parameters. Those functions' parameters can be stored on the hardware along with some look-up tables to represent the MPC solution to the problem. Although the nonlinear problems can be burdensome in this case, researchers can find an approximate solution instead. Another way to tackle the real-time related problems of MPC is to develop specific and simplified mathematical solvers to enjoy the inherent robustness of the online implementation. However, to maintain a small size of the controller and computational time, the former approach is selected.

In this research, the multi-parametric class of MPC is utilized and, to pursue the nonlinearity of the aforementioned control-oriented model, it is linearized for multiple operating point; in the end, a single controller is proposed. Consider the discrete and linear state-space model based on Eq. (2). For handling the tracking feature of the controller, we take the control-oriented model into the error space where the new state variables are the difference between *SOC* and *V*, and their reference values as:

$$\begin{aligned} x(k+1) &= Ax(k) + Bu(k) + F, \\ y(k) &= Cx(k), \end{aligned} \tag{3}$$

where $x(k) \in R^2$ are the state variables, $u(k) \in R^4$ are the manipulated inputs, $y(k) \in R^2$ are the outputs. Let $x_1 = e_{SOC} = SOC - SOC_{ref}$ and $x_2 = e_V = V - V_{ref}$. By considering prediction and control horizon, the prediction equation is obtained. In this equation, the inputs and outputs are:

$$U = \begin{bmatrix} u(k \mid k) \\ u(k+1 \mid k) \\ \vdots \\ u(k+N_c-1 \mid k) \end{bmatrix}, \qquad Y = \begin{bmatrix} y(k+1 \mid k) \\ y(k+2 \mid k) \\ \vdots \\ y(k+N_p \mid k) \end{bmatrix}, \tag{4}$$

where $u\,(k_i + 1 \mid k_i)$ means the predicted output at $k_i + 1$ step based on the measurement at k_i step, N_c and N_p are the control and prediction horizon length. By applying the input vectors to the system model, the predicted outputs are calculated and stored. In MPC control, optimal system inputs are calculated by minimizing a cost function. According to Eq. (5), the standard form of the cost function is:

$$\begin{aligned} &\min \frac{1}{2} U^T H U + q^T U + r \\ &Z \quad \text{s.t} \quad GU \le W \end{aligned} \tag{5}$$

$Z \in R^s$, $H = H^T > 0 \in R^{s \times s}$, $W \in R^m$, $G \in R^{m \times s}$, $q \in R^s$.

If the objective function is convex, the local optimum point is the global optimum point. The optimal point can be found by solving this optimization problem. Finally, the cost function is formulated according to the expected control objectives. As mentioned before, the advantages of the MPC is the systematic handling of the system constraints. There are three major types of constraints frequently encountered in applications. The first two types deal with constraints imposed on the control variables $u(k)$, and the third type of constraint deals with output $y(k)$ or state variable $x(k)$ constraints [18]. The cost function for minimizing fuel consumption and improve drivability while meeting the hard constraints can be written as:

$$J = \sum_{i=1}^{N_p} x_i^T Q_x x_i + \Delta x_i^T Q_{\Delta x} \Delta x_i + u_i^T R_u u_i + \Delta u_i^T R_{\Delta u} \Delta u_i, \tag{6}$$

where the regulation objective, minimum variation for the states., especially in terms of velocity, minimum effort and its variation are considered via the tuning matrices Q_x, $Q_{\Delta x}$, R_u, and $R_{\Delta u}$, respectively. This optimization problem is subjected to the following constraints, where the parameter values are shown in Table 1.

$$\begin{matrix} T_{m,\min} < T_m < T_{m,\max} \\ T_{\mathrm{e},\min} < T_e < T_{\mathrm{e},\max} \\ i_{cvt,\min} < i_{cvt} < i_{cvt,\max} \\ T_{\mathrm{b},\min} < T_b < T_{\mathrm{b},\max} \end{matrix}, \quad \begin{matrix} 0.2 < SOC < 1 \\ 0 < V \end{matrix}. \tag{7}$$

The computational burden of the aforementioned problem might be an issue for real-time applications, because a constrained optimization problem should be solved at each time step. This requires capable and expensive hardware along with a reliable solver. To avoid those potential problems, we solve the MPC explicitly. In this way, we can find some regions throughout the state space. It can be shown that for a quadratic optimization problem with affine constraints, each region contains an affine function of the related parameters as the solution. In other words, the manipulated inputs are piecewise affine functions of state variables:

$$u = \beta_j x + \gamma_j, \tag{8}$$

where β_j and γ_j are the constants for j^{th} region.

Those constants are different for the regions and can be obtained by solving the MPC problem explicitly. The explicit MPC (eMPC) replaces the need for solving the optimization problem online with storing tables of the affine functions' coefficients and a point location procedure. This approach improves the real-time implementation capability of the controller. At the implementation stage, we need to have the initial state variable (parameter of eMPC) and then find the region that contains it (point location procedure). Once the region is found, the related coefficients (β and γ) are available. To find the manipulated input, the initial state variable is substituted into Eq. (8) [19]. By scaling the state variables and manipulated inputs and solving the problem parametrically, the following regions are derived based on the multi-parametric toolbox (MPT) [20], as shown in Fig. 2. Inside each of 55 regions for prediction horizon with the length of 3 steps, there is an affine function of the parameters, namely, the difference between state variables and reference values. By increasing the prediction horizon length, we obtain more regions for better controller performance. However, this action increases the size of the controller, which might be problematic for the control hardware. In fact, there is a trade-off between simplicity and performance, and the design procedure should be directed in such a way that it addresses those two extremes efficiently.

Those affine functions are depicted in Fig. 3 for four manipulated inputs that are scaled based on their maximum values ($\bar{\alpha} = \alpha / |\alpha_{\max}|$).

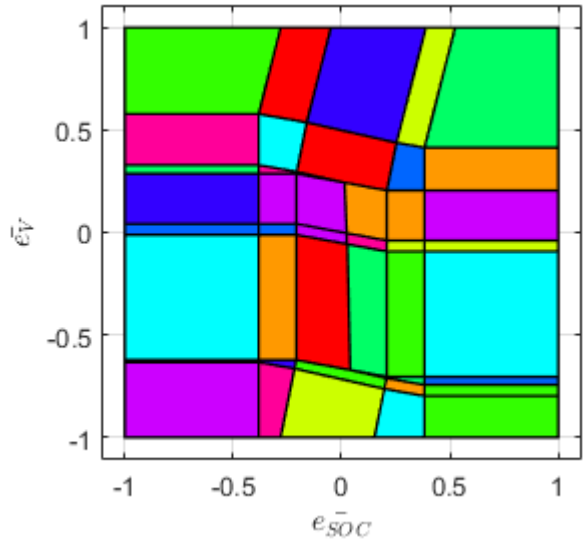

Fig. 2. *Proposed EMS polytopes*

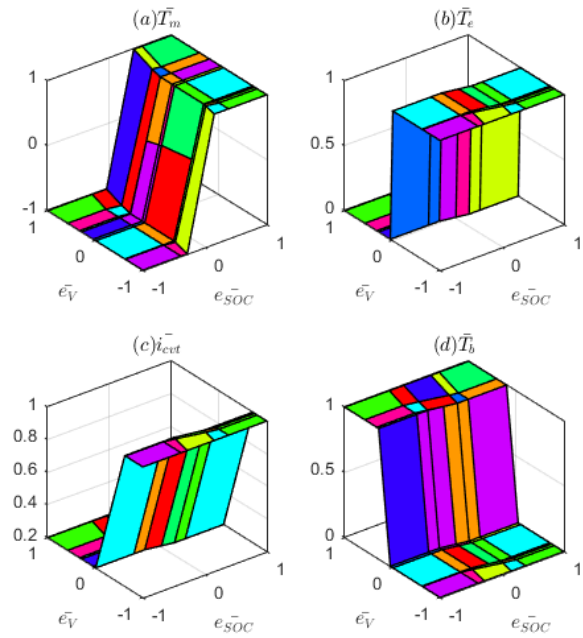

Fig. 3. *Proposed EMS manipulated inputs vs parameters: scaled a) motor torque b) engine torque, c) CVT ratio, and d) braking torque*

As seen, we can divide the parameter regions into four sections.

1. $\bar{e}_{SOC} < 0$ and $\bar{e}_V < 0$: In this region (which represents the toughest scenario for the EMS) the vehicle velocity is demanded to be increased and battery SOC is less than the predefined level. Therefore, the energy management system is not able to count on the electric drive to propel the vehicle. As a result, the braking torque should be

zero, and the electric machine should be set into the generator mode (negative torque) to charge the battery. However, the ICE should be pushed to its limits so that it can propel the vehicle and charge the battery at the same time. Nevertheless, based on the difference between the desired and current velocity, the CVT ratio may vary between its limits. According to Fig. 3c, as the absolute value of $\bar{e}_V$ gets larger, a higher CVT ratio is required to increase the driving torque on the wheels so that the vehicle would reach the required speed more quickly.

2. $\bar{e}_{SOC} > 0$ and $\bar{e}_V < 0$: Although this region resembles the above one, EMS faces a more gentle scenario since the battery state of charge is higher than its reference. Thus, the electric drive can assist the engine in propelling the vehicle. Braking torque is zero again, the engine torque and CVT ratio alter with the magnitude of $\bar{e}_V$, and the motor torque is positive and tops out it maximum value for more severe acceleration.
3. $\bar{e}_{SOC} < 0$ and $\bar{e}_V > 0$: Here, EMS should slow down the vehicle since the current velocity is higher than its reference. In contrast, the SOC level should be increased. Therefore, there is a good chance for regenerative braking and, as shown in Fig. 3a, the electric drive switches to the generator mode. Moreover, the mechanical braking torque would no longer be zero.
4. $\bar{e}_{SOC} > 0$ and $\bar{e}_V > 0$: In this region, the vehicle velocity should be decreased, and there is no need to charge the battery. As such, the engine is off, and the braking torque is high.

By reviewing the aforementioned regions, it turns out that the manipulated inputs trend matches the expectation from EMS. However, the shape of those surfaces determines the optimality and the performance of the controller. To investigate this, we need to implement those curves into the simulation high-fidelity model and check the overall performance over the standard driving schedules. Nonetheless, the convex cost function. as shown in Fig. 4, confirms the optimality of the produced controls scheme.

3 CONTROL PROTOTYPING

The HIL simulation is a more realistic platform to evaluate controller performance as opposed to the model-in-the-loop simulation. In a HIL platform, real signals from a controller are transferred to a test system that mimics reality. For this research, a dSPACE HIL platform has been used. In addition to the simulator, a

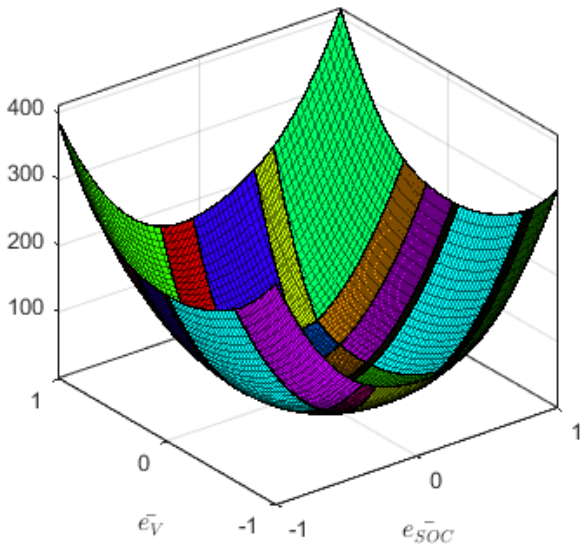

Fig. 4. *Multi-parametric optimization optimal values*

real-time model and prototype hardware are required to augment the controller capability. Fig. 5 depicts the schematic of the HIL test platform.

The virtual simulation model is accommodated to a real-time machine. The Autonomie model of the HEV is stored on the simulator (DS1006) and run in real time. In each time step, the simulator solves the high-fidelity model and sends back the required information to the control hardware via a controller area network (CAN). The most challenging part of an HIL test is to generate a C-code from the controller and to load it onto the control hardware. We considered this hindrance beforehand in the control design stage, at which point we solved the problem to obtain some polytopes along with some piecewise affine functions. Therefore, we face minimal effort to implement the controller onto the control hardware. A few specific libraries in dSPACE are allocated for generating a C-code for different devices, such as MicroAutoBoxII and DS1006 processor boards. As such, by using those functions, a C-code of the proposed control scheme is derived and loaded onto the control hardware (MicroAutoBoxII). For enabling communication with the simulator over the CAN bus, the MicroAutoBox has two bifurcated CAN controllers (four CAN channels) [21]. To facilitate this communication along with uploading the executable files, managing the test, and recording the simulation data, ControlDesk software is utilized.

The specifications of the input and output signals are determined in Table 2. The resulted polytopes of the controller are implemented into the

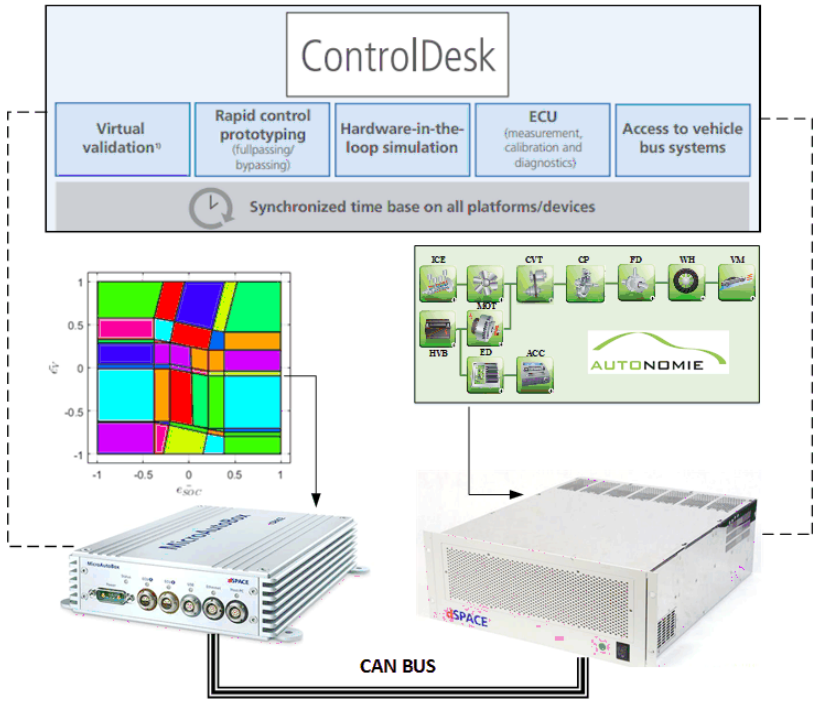

Fig. 5. *dSPACE HIL testing platform schematic*

MicroAutoBox. Basically, most of the ECU's physical memory is occupied by the CAN BUS communication section. Hence, there is a limited physical memory left to fit the controller logic. The total maximum occupied size of the proposed controller is barely around 100 Kb, which is promising.

Table 2. *HIL signals*

CAN Signal	Variable	CAN ID	Bit length
MicroAutoBox Input	SOC	100	16
	Reference SOC	101	16
	Vehicle velocity	102	32
	Desired vehicle velocity	103	32
MicroAutoBox Output	Motor torque	120	32
	Engine torque	121	32
	CVT ratio	122	32
	Braking torque	123	32

The proposed energy management system requires four readings from the real-time machine: the current battery state of charge, the reference SOC, vehicle velocity, and the desired velocity to find e_{SOC} and e_V, respectively. The four measurements are done by the real-time machine using the Autonomie model introduced in Section 1.2. Now multi-parametric EMS looks for the appropriate motor torque, engine torque, CVT ratio and braking torque, which can be directly implemented to the Autonomie model. Moreover, the low-level controllers in the Autonomie model can make the engine and electric motor follow the transferred set points, which are dictated by MicroAutoBox.

Moreover, the controller is supposed to provide the appropriate control action within a period shorter than the model solver step size by considering CAN bus communication delays. Thus, the controller should be faster than the plant, which can be investigated through the HIL procedure. By performing the HIL test for different scenarios, it is observed that the turnaround time is less than 30 microseconds, which proves that the proposed EMS is much faster than real time. In the next section, we review the HIL simulation results.

4 RESULTS AND DISCUSSIONS

To validate the performance of the controller, we have considered three different driving schedules: the highway fuel economy test (HWFET), NEDC and the worldwide harmonized light vehicles test cycle (WLTC). To demonstrate the performance of the proposed approach, a comparison is made with the baseline Autonomie controller. Fig. 6 shows the simulation results for the HWFET cycle. As shown

in Fig. 6a, the drivability performance remains satisfactory, since the controller tracks the velocity set point carefully. Although the final value of SOC for both approaches are the same, there is a difference between the battery SOC trajectory for the proposed controller and the baseline throughout the driving schedule. The proposed EMS has used the battery more frequently than the baseline controller in order to optimize the ultimate fuel economy of the vehicle. A part of this difference is due to the predictive nature of the proposed controller, as it has more knowledge about the future. Since there are some braking occasions ahead, the EMS allows the electric drive to deplete the battery more frequently as compared to the baseline strategy. Fig. 6b depicts the CVT ratio, which results from the proposed EMS, in which the CVT ratio is lower than the baseline controller in total. Because of the highway and the high-speed schedule, the CVT is expected to be tuned into its lower ratios, which is confirmed in the plots. Fig. 6c and d show the engine power and the torque. The engine power for the proposed EMS is slightly lower than the baseline strategy because of the more frequent assistance of the electric drive, which contributes to better fuel economy. This is more visible at the beginning of the drive cycle, for which higher acceleration is demanded. Fig. 6e shows the electric drive power, which is negative for the braking parts of the drive cycle to recuperate a part of mechanical braking energy dissipation.

According to Fig. 7a, the drivability performance of the proposed controller for NEDC schedule is acceptable, but because of the pattern of the driving schedule, the resulted battery SOC for two controllers are close to each other. The major difference in the two controllers is shown in Fig. 7b, where the proposed EMS tends to keep the CVT ratio lower for better engine fuel economy. Consequently, lower engine torque is observed from implementing the baseline strategy in Fig. 7c. However, the total power of the engine throughout the drive cycle is lower for the proposed control scheme as in Fig. 7d. Fig. 7e shows the electric motor assistance especially for the city-driving microcycles.

Similarly, the drivability index is confirmed for the WLTC cycle according to Fig. 8a by implementing the proposed EMS. Once again, the proposed EMS results in a lower CVT ratio more frequently than

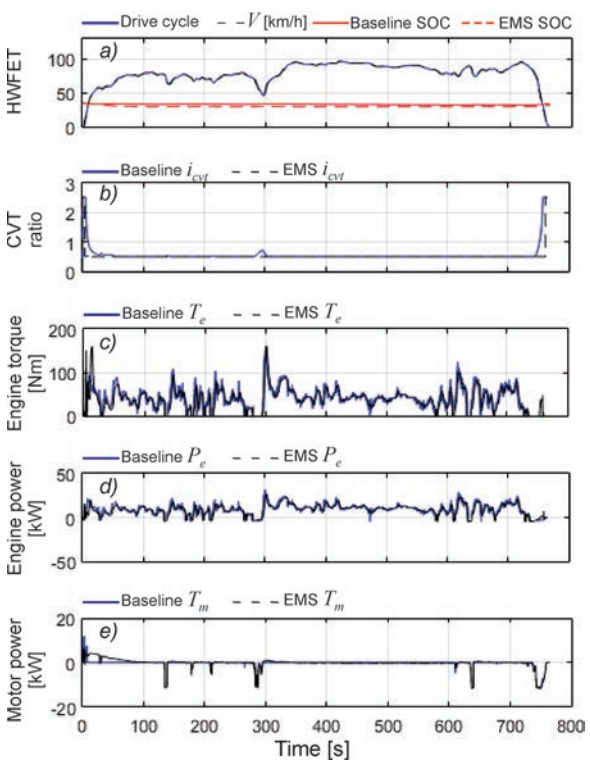

Fig. 6. *HWFET cycle simulation; a) vehicle velocity [km/h] and battery SOC, b) CVT ratio, c) engine torque, d) engine power, e) electric motor power*

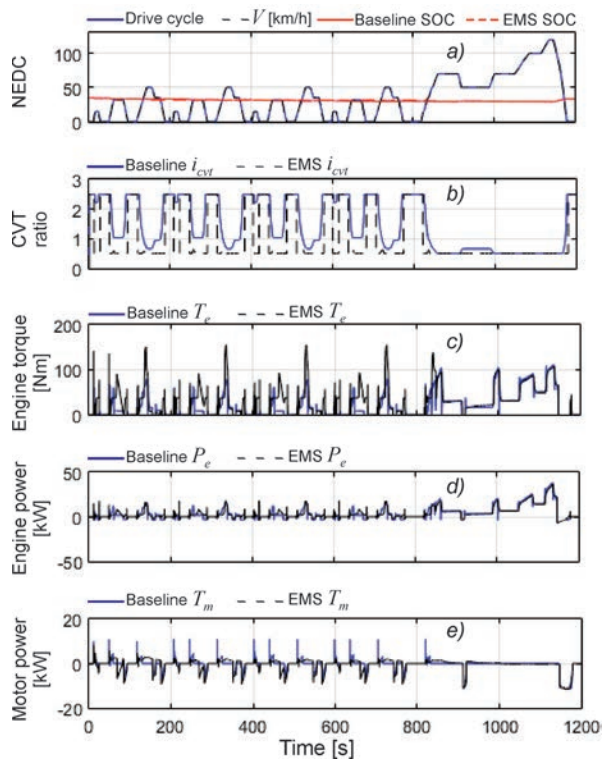

Fig. 7. *NEDC cycle simulation; a) vehicle velocity [km/h] and battery SOC, b) CVT ratio, c) engine torque, d) engine power, e) electric motor power*

the baseline controller in Fig. 8b. As such, the engine has better fuel economy despite operating in regions with higher torques (Fig. 8c). Slightly lower engine power and higher overall power of the electric drive in comparison to the baseline strategy proves the superior fuel economy of the proposed EMS, as in Figs. 8d and e.

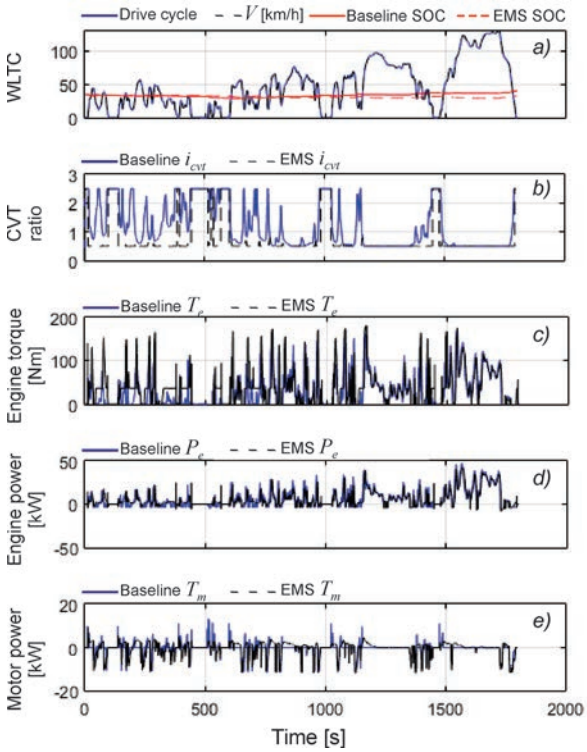

Fig. 8. *WLTC-class 3 simulation; a) vehicle velocity [km/h] and battery SOC, b) CVT ratio, c) engine torque, d) engine power, e) electric motor power*

Based on the travelling distance associated with each of the drive cycles, the fuel economy for the baseline Autonomie controller and the proposed EMS is calculated in Table 3.

Table 3. *Fuel economy values*

Drive cycle	Traveling distance [km]	Fuel economy [l/100 km]		Improvement [%]
		Baseline	Proposed EMS	
HWFET	16.450	4.988	4.796	4
NEDC	11.000	5.788	5.116	11.61
WLTC	23.194	6.083	5.442	10.54

The more realistic Autonomie high-fidelity model ensures the presentation of real-world results for implementing the proposed EMS. As expected for HWFET, the fuel economy improvement for the higher vehicle velocity is limited as the engine is more efficient and experienced less transience, so that little assistance is required from the electric drive. For the mixed city and highway driving of NEDC and WLTC cycles, the proposed EMS results in about 11 per cent lower fuel consumption in comparison to the baseline strategy. To draw a more comprehensive comparison, similar studies are considered as well. Tang et al. [13] have obtained a similar fuel economy for NEDC cycle using a Gauss pseudo-spectral MPC to reduce the computational time for the controller on the same architecture of hybrid vehicle with close parameter values to our study. However, the proposed EMS in this study is completely real-time implementable and downsized for a commercial control hardware. Moreover, its performance and capability are validated with HIL testing via the Autonomie simulation model.

5 CONCLUSIONS

In this research, a real-time implementable multi-parametric predictive energy management system is proposed for parallel hybrid electric vehicles with CVT driveline. To exploit the accuracy of the powertrain model and maintain its simplicity as appropriate for a model-based control approach, a control-oriented model is considered based on the vehicle velocity and onboard high-voltage battery. To investigate the performance of the controller, a hardware-in-the-loop simulation via Autonomie experimentally-validated model of the powertrain is performed. The results of applying the sub-optimal predictive EMS to the mentioned simulation model shows more than 8 % improvement in fuel economy for three standard driving schedules. The proposed EMS can be fully-implemented in control hardware for real-time applications.

6 ACKNOWLEDGMENT

The authors acknowledge the Smart Hybrid and Electric Vehicles Systems (SHEV) lab at the University of Waterloo for providing them with the required platform for performing the simulations.

7 REFERENCES

[1] Pfiffner, R., Guzzella, L. (2001). Optimal operation of CVT-based powertrains. *International Journal of Robust Nonlinear Control*, vol. 11, no. 11, p. 1003-1021, **DOI:10.1002/rnc.642**.

[2] Hatanaka, T., Yamada, T., Fujita, M., Morimoto, S., Okamoto, M. (2009). Explicit receding horizon control of automobiles with continuously variable transmissions. *Nonlinear Model*

Predictive Control, vol. 384, p. 561-569, **DOI:10.1007/978-3-642-01094-1_46**.

[3] Kazemi, R., Raf'at, M., Noruzi, A.R. (2014). Nonlinear optimal control of continuously variable transmission powertrain. *International Scolary Research Notices*, vol. 2014, art. ID 479590, **DOI:10.1155/2014/479590**.

[4] Yildiz, A., Kopmaz, O. (2017). Control-oriented modelling with experimental verification and design of the appropriate gains of a PI speed ratio controller of chain CVTs. *Strojniški vestnik - Journal of Mechanical Engineering*, vol. 63, no .6, p. 374-382, **DOI:10.5545/sv-jme.2016.4184**.

[5] Bemporad, A., Bernardini, D., Livshiz, M., Pattipati, B. (2018). Supervisory model predictive control of a powertrain with a continuously variable transmission. *SAE Technical Paper*, **DOI:10.4271/2018-01-0860**.

[6] Tao, D., Zhifei, L., Yanli, Y. (2019). Research on the novel discretized ratio control strategies and hardware-in-the-loop test for continuous variable transmission system. *International Journal of Modeling, Simulation, and Scientific Computing*, vol. 10, no. 3, **DOI:10.1142/S1793962319500120**.

[7] Mamala, J., Jantos, J. (2009). Shift speed control in CVT powertrain. *International Journal of Vehicle Design*, vol. 54, no. 1, p. 26-34, **DOI:10.1504/IJVD.2010.034868**.

[8] Takiyama, T., Morita, S. (1999). Engine-CVT consolidated control using LQI control theory. *JSAE Review*, vol. 20, no. 2, p. 251-258, **DOI:10.1016/S0389-4304(98)00062-9**.

[9] Kim, T., Kim, H., Yi, J., Cho, H. (2000). Ratio control of metal belt CVT. *SAE Technical Paper*, **DOI:10.4271/2000-01-0842**.

[10] Hu, J., Mei, B., Peng, H., Guo, Z. (2019). Discretely variable speed ratio control strategy for continuously variable transmission system considering hydraulic energy loss. *Energy*, vol. 180, p. 714-727, **DOI:10.1016/j.energy.2019.05.086**.

[11] Hofman, T., Steinbuch, M., van Druten, R., Serrarens, A.F.A. (2009). Design of CVT-based hybrid passenger cars. *IEEE Transactions on Vehicular Technology*, vol. 58, no. 2, p. 572-587, **DOI:10.1109/TVT.2008.926217**.

[12] Ji, J., Park, J., Kwon, O., Kim, H. (2012). An energy management strategy for a CVT based parallel hybrid electric vehicle. *IEEE Vehicle Power and Propulsion Conference*, p. 380-382, **DOI:10.1109/VPPC.2012.6422668**.

[13] Tang, J., Guo, L., Gao, B., Liu, Q., Yu, S., Chen, H. (2016). Energy management of a parallel hybrid electric vehicle with CVT using model predictive control. *35th Chinese Control Conference (CCC)*, p. 4396-4401, **DOI:10.1109/ChiCC.2016.7554036**.

[14] Li, H., Hu, X., Fu, B., Wang, J., Zhang, F., Zhou, Y. (2019). Effective optimal control strategy for hybrid electric vehicle with continuously variable transmission. *Advances in Mechanical Engineering*, vol. 11, no. 3, **DOI:10.1177/1687814018824811**.

[15] Li, H., Zhou, Y., Xiong, H., Fu, B., Huang, Z. (2014). Real-time control strategy for cvt-based hybrid electric vehicles considering drivability constraints. *Applied Sciences*, vol. 9, no. 10, art. ID 2074, **DOI:10.3390/app9102074**.

[16] Wang, Q., Frank, A.A., (2014). Plug-in HEV with CVT: configuration, control, and its concurrent multi-objective optimization by evolutionary algorithm. *International Journal of Automotive Technology*, vol. 15, p. 103-115, **DOI:10.1007/s12239-014-0012-z**.

[17] Del Re, L., Allgöwer, F., Glielmo, L., Guardiola, C., Kolmanovsky, I. (eds.) (2010). *Automotive Model Predictive Control: Models, Methods and Applications*, Springer, London, **DOI:10.1007/978-1-84996-071-7**.

[18] Wang, L. (2009). *Model Predictive Control System Design and Implementation Using MATLAB®*. Springer, London, **DOI:10.1007/978-1-84882-331-0**.

[19] Taghavipour, A., Azad, N.L., McPhee, J. (2015). Real-time predictive control strategy for a plug-in hybrid electric powertrain. *Mechatronics*, vol. 29, p. 13-27, **DOI:10.1016/j.mechatronics.2015.04.020**.

[20] Herceg, M., Kvasnica, M., Jones, C.N., Morari, M. (2013). Multi-parametric toolbox 3.0. *Proceedings of the European Control Conference*, p. 502-510, **DOI:10.23919/ECC.2013.6669862**.

[21] Taghavipour, A., Vajedi, M., Azad, N.L. (2019). *Intelligent Control of Connected Plug-In Hybrid Electric Vehicles*. Springer, Cham, **DOI:10.1007/978-3-030-00314-2**.

Strojniški vestnik - Journal of Mechanical Engineering 67(2021)4, 153-166

DOI:10.5545/sv-jme.2020.7068 Original Scientific Paper
Received for review: 2020-12-16
Received revised form: 2021-03-22
Accepted for publication: 2021-04-07

A Strain-Based Method to Estimate Longitudinal Force for Intelligent Tires by Using a Physics-Based Model

Haichao Zhou[1] – Huiyun Li[1] – Jian Yang[1,*] – Qingyun Chen[1] – Guolin Wang[1] – Tong Han[1] – Jieyu Ren[2] – Te Ma[1]

[1]Jiangsu University, School of Automotive and Traffic Engineering, China
[2]Zhejiang Wanxiang Marelli Shock Absorbers, China

Tires are essential components of vehicles and the only vehicle components in contact with the road. The tire longitudinal force originating from the contact between the tire and road can enhance traction and braking and contribute to the directional stability of vehicles. If the longitudinal tire force can be accurately estimated, vehicle safety can be improved. This study established a longitudinal tire physics-based model combining the brush model with the flexible ring model to develop a strain-based intelligent tire system for estimating the longitudinal tire force. The developed longitudinal dynamic model was used to study tire strain characteristics under pure longitudinal slip conditions. An algorithm was developed for estimating the longitudinal tire force through feature extraction and data fitting of the tire strain. A finite-element tire model was established to simulate the longitudinal force. Comparing the simulated and estimated forces indicated that the proposed algorithm can accurately predict the longitudinal force of intelligent tires and thus provide useful information to vehicle stability control systems.

Keywords: intelligent tire, tire model, strain analysis, longitudinal force, force estimation

Highlights

- *A longitudinal tire physics-based model combining the brush model with the flexible ring model is established and validated.*
- *Tire deformation characteristics under pure longitudinal slip conditions are analysed, and the effects of the longitudinal forces on radial deformation and circumferential strain are compared and analysed.*
- *The characteristic curve index of radial deformation and circumferential strain under different longitudinal forces are quantitatively analysed.*
- *A strain-based estimation algorithm for longitudinal tire force is proposed, and the simulation results verify the accuracy and credibility of the estimation algorithm.*

0 INTRODUCTION

Tires are the only parts of vehicles that come into contact with the road surface. The tire–road interaction directly affects tire performance and influences vehicle manoeuvrability [1]. The tire-road contact force can be determined by monitoring the interaction between tires and the road, and it can be used to improve the performance of stability controllers in intelligent vehicles [2]. This is why the automotive industry and scholars alike aim to estimate and control the forces accurately between tires and the road to enhance vehicle manoeuvrability and safety [3]. Intelligent tires can improve the safety of vehicles by providing information on tire force, tire load, road surface friction, and several other crucial contact characteristics [4].

Intelligent tires usually refer to tire systems equipped with sensors for monitoring tire dynamic parameters and road conditions to improve the dynamic control systems of vehicles. The sensor types used in such systems include accelerometers, piezoelectric, magnetic, and optical sensors; these sensors are selected for obtaining the surface acoustic waves, acceleration, deformation, and strain of tires [5]. Several intelligent tire systems have been proposed, and the results show that the intelligent tires provide a correlation between strain gauge measurements and tire operational conditions [6].

The most active and passive safety control systems are developed using a vehicle dynamic model, requiring the longitudinal tire forces to determine vehicle parameters, including longitudinal acceleration, braking distance, and slip rate [7]. Moreover, according to linear and nonlinear vehicle dynamic models, the longitudinal force acting on the tire is a major factor affecting the behaviour of a vehicle [8]. Thus, the estimation of the longitudinal force of intelligent tire has a great impact on vehicle handling and safety. By performing a polynomial fit, Yang et al. [9] estimated the longitudinal force using its relationship with the peak ratio between the tire's circumferential tensile strains and the front and rear contact areas. Matsuzaki and Todoroki [10] conducted data fitting for the functional relationship between the peak ratio of the tire circumferential compression strain in the contact patch and the braking torque of the front and rear wheels to monitor the braking behaviour of tires and estimate the longitudinal tire force. However, the function fitting process becomes

*Corr. Author's Address: Jiangsu University, Zhenjiang, China, yangjian@ujs.edu.cn

complicated if several tire deformation features are extracted to assess the tire force. Consequently, the resultant fitting equation may have low accuracy.

Considering the complexity of tire structures and the coupling characteristics of tire forces during rolling conditions, machine-learning algorithms, such as neural network algorithms, are the most widely applied algorithms in tire force estimation. Zhao et al. [11] extracted acceleration signal features for different tire design schemes and estimated the vertical and longitudinal tire forces using a backpropagation neural network. Zhu and Lu [12] used a camera to track the displacement of tread and proposed a neural network algorithm to estimate tire force. However, when estimating tire forces by using machine-learning algorithms, the computing accuracy of the algorithms not only depends largely on the amount and scope of the training data but also requires the use of experimental tests and a simulation model to compute the variables. Developing a comprehensive intelligent-tire-based algorithm is a time-consuming and expensive process. Experimental data on velocity, tire pressure, various road conditions, and tire loading should be used to train the algorithm. The finite-element model (FEM) should be used to test tire component parameters properties, and it must be validated; therefore, FEM requires considerable computer resources.

Estimation algorithms based on tire physics-based models have received increasing attention due to high calculation efficiency and high estimation accuracy. The tire force is calculated according to a model of complex tire behaviors. Zhang and Yi [13] and Zhang et al. [14] developed a new type of pressure-sensitive conductive rubber sensor, and derived a formula for the tire-road friction force estimation based on the local friction force between the tire and road. Yi and Liang [15] implemented a polyvinylidene fluoride (PVDF)-based sensor to estimate tire deformation and motion, from a small vehicle model. They also presented an analytical sensing output model that can be used to capture the wheel/ground friction characteristics. Based on the test results of strain, Garcia-Pozuelo et al. [16] used a fuzzy logic algorithm to estimate tire slip angle and working conditions. Xiong and Tuononen [17] compared the carcass deformation of the flexible ring model with the measured results obtained using an optical laser sensor and proved that the tire flexible ring tire model can be used to predict tire deformation. Garcia-Pozuelo et al. [18] proposed a real-time physical model that reflects the longitudinal dynamics of intelligent tires and analysed the correlation between the measured tire strain and developed physical model to prove that the flexible ring tire model can be used to predict the strain on the inner liner. Thus, that model correlates strain information with dynamic tire parameters, predict changes in strain signals, and can be applied in the development of intelligent tire force estimation algorithms. APOLLO project claimed that strain sensors have merit over accelerometers for wheel force estimation. Also, the noise level of strain sensors is generally lower than the accelerometer noise and measured value is not affected by the tire rotational speed.

In this study, a strain-based tire longitudinal force estimation algorithm based on the physics-based model was developed. First, a longitudinal dynamic tire model was established based on the flexible ring model and brush model; Second, the signal characteristics of the loaded tire were analysed, and the relationships between the strain information and longitudinal force were established according to the flexible ring model to estimate the longitudinal force; Finally, the strain information obtained from the finite-element model was substituted into the proposed algorithm to estimate the longitudinal force. The simulated values of the longitudinal force agreed favourably with the estimated values; thus, the practicability and accuracy of the developed algorithm were verified.

1 ANALYTICAL MODEL OF TIRE LONGITUDINAL FORCE ESTIMATION

1.1 Flexible Ring Tire Model

In this study, the relationship between the strain information of the inner liner and tire dynamic parameters was established according to the flexible ring tire model [19], and the details of the model symbols are provided in the appendices. The flexible ring model provides theoretical support for the development of intelligent tire algorithms. According to differences in stiffness, a tire is simplified into four parts, as shown in Fig. 1., the tread band, tread rubber, sidewall, and wheel. The belt is modelled as a thin ring and meets an assumption of inextensible beams. The sidewall is simplified to radial and tangential springs with radial and tangential damping, respectively, expressing the influence of tire sidewall forces on the belt. The rim is modelled as a rigid circle with mass and inertia. To determine the tire velocity, the ring is represented in terms of cylindrical coordinates. Two reference systems are used to express the dynamic behaviour of the ring, as depicted in Fig. 2. One

system is a rotating reference system, which is a local coordinate system; the other system is a fixed reference system, which is a global coordinate system.

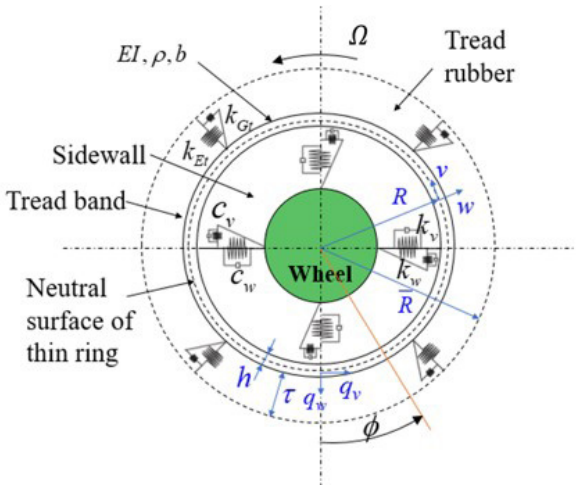

Fig. 1. *Flexible ring tire model*

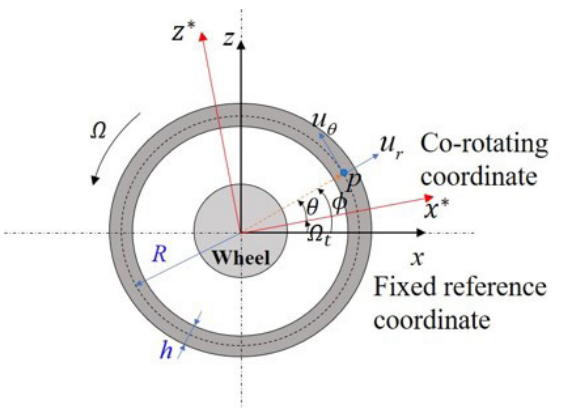

Fig. 2. *Configurations of two tire coordinate systems*

According to Hamilton's principle, the system reaches equilibrium when $\delta S = 0$. The dynamic equation of the tire can be established as Eq. (1):

$$\delta S = \int_{t_1}^{t_2} (\delta L + \delta W) dt, \tag{1}$$

where δW is the imaginary work of the non-conservative force, $L = T - V$ is the Lagrange function, T is the kinetic energy of the system, and V is the potential energy of the system.

According to Hamilton's principle, the following equation is obtained:

$$\begin{cases} L = T_1 + T_2 - S_1 - S_2 \\ \delta W = \delta E_1 + \delta E_2 \end{cases}, \tag{2}$$

where T_1 is the kinetic energy of the ring, T_2 is the kinetic energy of the wheel, S_1 is the strain energy stored in the ring, S_2 is the elastic energy stored in the sidewall, and δE_1 and δE_2 represent the virtual work performed by extensional forces.

Because of the high extensional stiffness of the modern radial tire, the middle surface of the tire carcass is assumed to be inextensible, which means the circumferential length of the neutral surface of the ring is constant during the deformation. According to the Bernoulli-Euler assumption, the ring is an inextensible curved, bending beam [18]. Hence, the radial deformation and tangential deformation at any point on the middle surface of the elastic ring in a circumferential position satisfies $w = -\partial v / \partial \theta$. Under the condition that tire rolling is steady with no external moment acting on ring [20], the final equations of motion of the ring expressed in terms of the rotating coordinate system are derived as follows Eq. (3):

$$\begin{aligned} &-\frac{EI}{R^4}\left(\frac{\partial^2 v}{\partial\theta^2}+2\frac{\partial^4 v}{\partial\theta^4}+\frac{\partial^6 v}{\partial\theta^6}\right)+\frac{\sigma_\theta^0 A}{R^2}\left(v+2\frac{\partial^2 v}{\partial\theta^2}+\frac{\partial^4 v}{\partial\theta^4}\right)\\ &+\rho A\left(\ddot{v}-\frac{\partial^2\ddot{v}}{\partial\theta^2}-4\Omega\frac{\partial\dot{v}}{\partial\theta}+\Omega^2\left(\frac{\partial^2 v}{\partial\theta^2}-v\right)\right)-k_w\frac{\partial^2 v}{\partial\theta^2}\\ &+k_v v-c_w\frac{\partial^2\dot{v}}{\partial\theta^2}+c_v\dot{v}-\frac{p_0 b}{R}\left(v+\frac{\partial^2 v}{\partial\theta^2}\right)=q_v+\frac{\partial q_w}{\partial\theta}, \end{aligned} \tag{3}$$

where σ_θ^0 is the initial stress in the tangential direction of the belt, caused by the inflation pressure; $A = bh$ is the cross-sectional area of the thin ring of the tire.

When using the modal expansion method to solve the tire dynamic equations [21], the equation of motion of the radial deformation w. At the angle ϕ of the neutral surface of the thin ring under the forces Q_w and Q_v can be obtained as Eq. (4), where Q_w and Q_v are the magnitudes of radial and tangential line forces acting at specified stationary angular coordinate ϕ_0.

$$\begin{aligned} &w(\phi) = \\ &\sum_{n=1}^{N} A_n \left[nQ_w \cos n(\phi_0 - \phi + \gamma_n) - Q_v \sin n(\phi_0 - \phi + \gamma_n) \right]. \end{aligned} \tag{4}$$

1.2 Tread Longitudinal Brush Model

When a tire rolls on the road, the distribution of tire contact pressure in the contact patch is nonsymmetrical. The contact pressure is concentrated at a distance Δ in front of the contact centre, as displayed in Fig. 3. Compared with tire contact pressure experiment results, an arbitrary pressure distribution is used to describe the pressure distribution in the contact patch. To facilitate analysis of the ring model, the centre of the contact patch is defined as 0°.

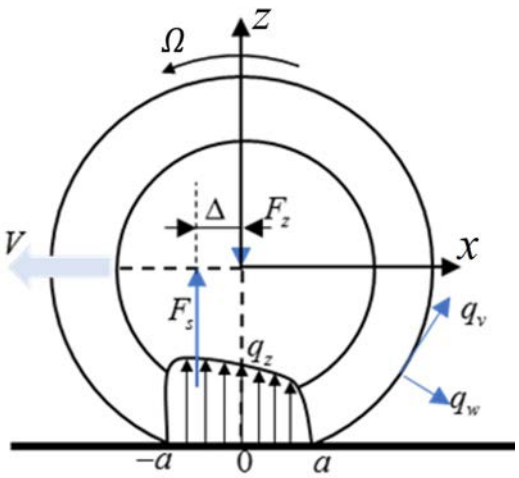

Fig. 3. *Pressure distribution in the contact patch*

According to the Unitire model [22], the normal pressure distribution $q_z(x)$ in the contact patch is expressed as follows Eq. (5):

$$q_z(x) = \frac{F_z}{2a} \cdot \eta\left(\frac{x}{a}\right) = \frac{F_z}{2a} \cdot \eta(u), \tag{5}$$

where $u = x/a$ is the relative coordinate in the contact patch, $2a$ is the contact patch length, and $\eta(u)$ is the arbitrary pressure distribution function. If the vertical load offset is Δ, $\int_{-a}^{a} q_z(x) \cdot dx = F_z$ and $\int_{-a}^{a} q_z(x) \cdot x \cdot dx = F_z \cdot \Delta$, then $\eta(u)$ should satisfy the following conditions:

$$\begin{cases} \eta(1) = \eta(-1) = 0 \\ \eta(u) \geq 0, u \in [-1,1] \\ \eta(u) = 0, u \notin [-1,1] \\ \int_{-1}^{1} \eta(u) du = 2 \\ \int_{-1}^{1} \eta(u) \cdot u \cdot du = 2 \cdot \frac{\Delta}{a} \end{cases}. \tag{6}$$

For the general tire loading conditions, $\eta(u)$ is expressed as Eq. (7):

$$\eta(u) = A \cdot (1 - u^{2n}) \cdot (1 - Bu), \tag{7}$$

According to the boundary conditions expressed in Eq. (6), A and B can be expressed as Eq. (8):

$$A = \frac{2n+1}{2n}, \tag{8}$$

$$B = -\frac{3 \cdot (2n+3)}{2n+1} \cdot \frac{\Delta}{a}. \tag{9}$$

To determine the common contact pressure distribution of the radial tires, the following parameters are used: $n = 2$ and $\Delta/a = 0.04$. The contact pressure in contact patch is illustrated in Fig. 4.

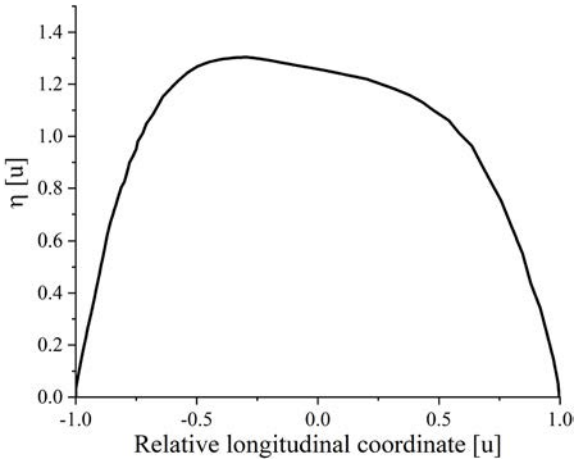

Fig. 4. *Pressure distribution in contact patch*

The rectangular coordinates of the pressure distribution function [Eq. (5)] are converted into angular coordinates [Eq. (10)] as follows:

$$q_z(\phi) = \frac{F_z}{2R|\phi_f|} \cdot \frac{5}{4}(1 - u_f^4) \cdot (1 + \frac{21}{125} \cdot u_f), \tag{10}$$

where ϕ_f is the leading contact angle, ϕ is an arbitrary angle in the contact patch, and $u_f = \phi/\phi_f$.

For a loaded tire under longitudinal slip conditions, the lateral and camber characteristics are neglected, and the brush of the tread can only move in the longitudinal direction. The longitudinal slip ratio S_x can be expressed as follows [23]:

$$S_x = \frac{-V_{sx}}{\Omega R_e} = -\frac{V\cos\alpha - \Omega R_e}{\Omega R_e} \quad S_x \in (-\infty, +\infty), \tag{11}$$

where Ω is the wheel angular speed; R_e is the effective rolling radius, which is set as the mean radius of the ring R; V_{sx} is the longitudinal travel speed of the tire with respect to the road surface; V is the wheel travelling speed; and $\alpha = 0$ is the lateral angle.

The tire carcass is rigid, the tire elasticity is concentrated on the tread, the tread unit is replaced by a row of bristles, and the contact patch length of the bristles is $2a$. With the development and advancement in the finite element method, the finite element analysis technology has been widely applied in the tire industry with high accuracy, and the contact patch length can be obtained using experimental test or finite element analysis. The contact patch length in this study was obtained using numerical simulation. To validate the tire FEM, the same tire, which is painted red, is tested on the self-developed tire test bench, as shown in Fig.

5a. The vertical load is applied by moving the lead screw, and the sensor provides the vertical force in real time. The bottom part of the tire was painted with red ink and then pressed against a sheet of white paper, which was placed on the support plate. The grounding footprint from test and simulation are shown in Fig. 5b. The simulation results are in good agreement with the test results under the vertical force 4000 N, and the maximum relative error of tire footprint was 1.74 % in the contact patch width. This implied that tire grounding characteristics ensure that tire FEM model is accurate, and it can be used to verify the tire estimation algorithm of the longitudinal force in the subsequence analysis.

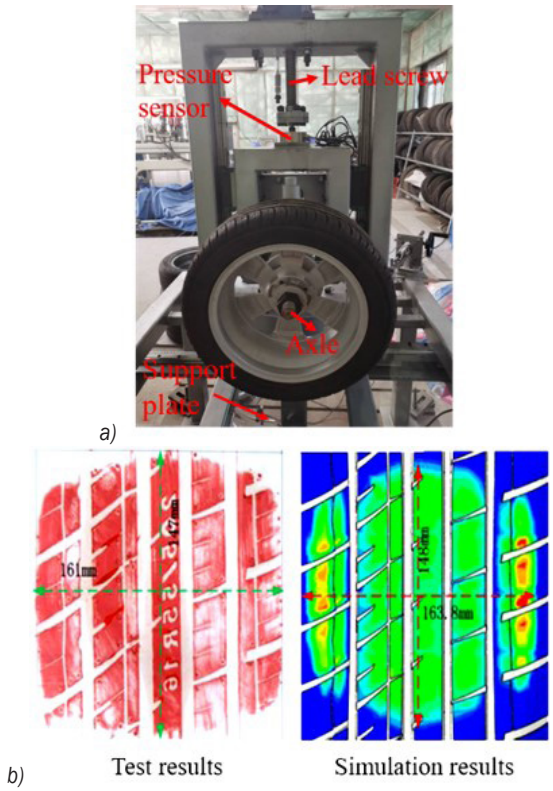

Fig. 5. *Comparison of tire grounding footprint; a) tire stiffness test bench; and b) footprint parameters*

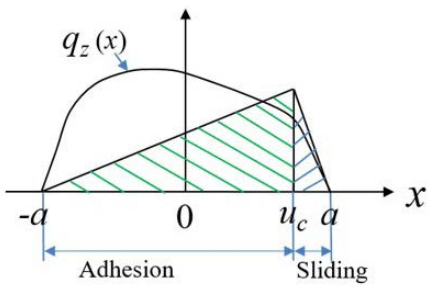

Fig. 6. *Contact area of a tire brush model*

Thus, the contact patch length of the bristles 2*a* is 148 mm. Due to the effect of the friction of the road surface, the grounding area of the brushes is divided into the adhesion region and slip region, as shown in Fig. 6.

Assuming that the longitudinal stress is caused by the deformation of the unit bristles in the contact patch, the longitudinal distribution force of the tread brush in the contact patch can be expressed as follows:

$$q_x(x) = \begin{cases} -(a-au)k_x S_x & \text{adhesion zone} \\ -\mu_x q_z(x)\,\mathrm{sgn}(S_x) & \text{slid zone} \end{cases},$$

where k_x is the tangential stiffness of the bristle, which is set as the tread tangential stiffness k_G, and μ is the tire–road friction coefficient.

The split point u_c divides the entire contact area into an adhesion zone and a sliding zone, and it is the sliding start point. When a sliding phenomenon occurs in the contact area, the split point u_c can be derived from the Eq. (12):

$$k_x \cdot (a-au) S_x = \frac{\mu F_z}{2a}\eta(u_c). \tag{12}$$

At this time, the total longitudinal force F_x of tire in the contact patch is the sum of the longitudinal forces of two parts of the adhesion zone and slid zone as shown in Eq. (13).

$$F_x = -\int_{-1}^{u_c} k_x (a-au)\cdot S_x \cdot a\,du - [\mathrm{sgn}(S_x)]\cdot \int_{u_c}^{1} q_z(u)\cdot \mu_x \cdot a\,du. \tag{13}$$

According to the coordinate transformation, the longitudinal force is expressed as a function of the angular coordinates as follows:

$$q_x(\phi) = \begin{cases} -R(|\phi_f| - \phi)k_x S_x, & \text{Adhesion} \\ -\mu q_z(\phi)\,\mathrm{sgn}(S_x), & \text{Sliding} \end{cases}.$$

The force components of the neutral surface in the radial and tangential directions (Fig. 1) can be derived as follows:

$$\begin{cases} q_w(\phi) = -q_z\cos\phi + q_x\sin\phi \\ q_v(\phi) = q_x\cos\phi + q_z\sin\phi \end{cases}. \tag{14}$$

According to Eq. (14), the radial deformation and circumferential strain of the neutral surface are expressed as shown in Eqs. (15) and (16).

Where N_ϕ is the number of equally divided units of the tire tread in the contact patch, $\Delta\phi$ is the separation angle between every two adjacent tread units, and $q_w(\phi_i)$ and $q_v(\phi_i)$ are, respectively, the radial and tangential forces acting on the tire.

The above work indicates that the strain and longitudinal force can be estimated by combining the flexible ring model with the brush model. Therefore, the estimation process of tire longitudinal force using the strain is illustrated in Fig. 7, and the application flow is subsequently described. Firstly, the tire contact angle of a loaded vertical force is obtained using the flexible ring model, and the vertical force distribution force is modelled with a parabolic function of the angular coordinate; Secondly, based on the brush tire model, the longitudinal force distribution is obtained with the slip ration and friction coefficient, and then, the longitudinal force distribution is divided into the radial and tangential directions; Lastly, the radial deformation and the circumferential strain of the ring are computed and obtained using Eqs. (15) and (16).

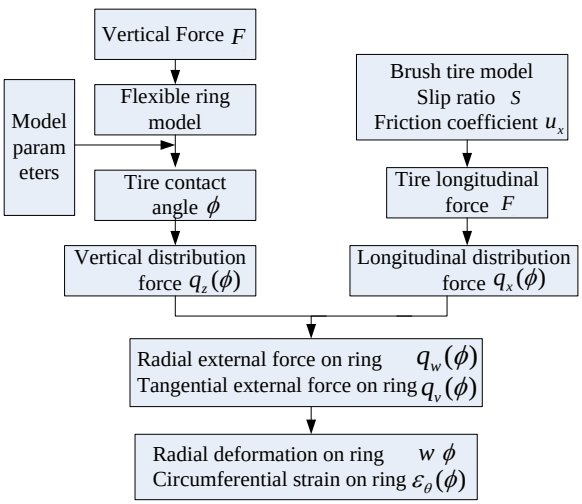

Fig. 7. *Schematic of tire longitudinal force estimation*

$$w(\phi)=\sum_{i=1}^{N_\phi}\sum_{i=1}^{\infty} nA_n\left[nq_w(\phi_i)\cos(n(\phi_i-\phi))-q_v(\phi_i)\sin(n(\phi_i-\phi))\right]\cdot\Delta\phi, \quad (15)$$

$$\varepsilon_\theta(\phi)=-\frac{y}{R^2}\sum_{i=1}^{N_\phi}\sum_{n=1}^{\infty} n^3\cdot A_n\left[nq_w(\phi_i)\cos(n(\phi_i-\phi))-q_v(\phi_i)\sin(n(\phi_i-\phi))\right]\cdot\Delta\phi. \quad (16)$$

For a loaded tire, there is a contact length in the contact area, and the carcass and tread present deformation, as shown in the following Fig. 8, where ϕ_f and ϕ_r are the leading contact angle and the rear contact angle, respectively. The force distribution $q_w(\phi)$ caused by carcass deformation can be expressed as follows:

$$q_w(\phi)=k_{Et}\cdot\left[-w(\phi)-d_0+\overline{R}(1-\cos\phi)\right]. \quad (17)$$

Assuming just the vertical force is given, the force distribution $q_w(\phi)$ at both ends of the contact area is zero: $q_w(\phi_f)=q_w(\phi_r)=0$. Then the amount of sinking of the tire $d_0=R(1-\cos\phi_f)-w(\phi_f)$ is obtained. At the same time, within the tire contact area, the flexible model satisfies the following boundary conditions:

$$\begin{cases}\chi_1=\int_{\phi_f}^{\phi_r} q_w(\phi)d\phi-F_z=0\\ \chi_2=\left[w(\phi_f)-\overline{R}(1-\cos\phi_f)\right]\\ \quad -\left[w(\phi_r)-\overline{R}(1-\cos\phi_r)\right]=0\end{cases}. \quad (18)$$

Based on the given model parameters of the flexible mode, the initial values of ϕ_f and ϕ_r are set, the radial deformation $w(\phi)$ and force distribution $q_w(\phi)$ can be obtained. The vertical force is estimated by integrating the force distribution within the contact angle. Taking the boundary conditions as criteria, if the error between the estimation of the vertical force and the given vertical force meets a demand, the contact angle ϕ is determined; otherwise, it needs to reset the values of ϕ_f and ϕ_r, and recalculate $w(\phi)$ and $q_w(\phi)$. It will not stop until the error meets the demand that the contact angle is determined.

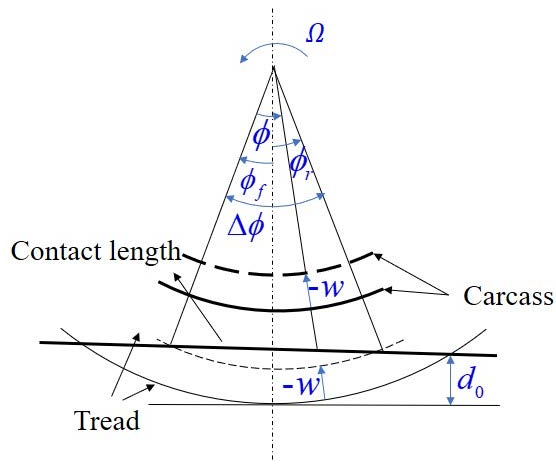

Fig. 8. *Deformations of tread and carcass*

2 RESULTS AND DISCUSSION

2.1 Tire Model Analysis

Through analysis of Eq. (4), the radial deformation of the neutral surface was discovered to be separable into the deformation caused by the tangential force and that caused by the radial force. When the tangential force

is 0, the radial deformation of the tire is approximately symmetrical; otherwise, the radial deformation of the tire is asymmetric.

Table 1. *Flexible ring model parameters*

Parameter	Value	Unit	Parameter	Value	Unit
ρ	1.8×10^3	kg/m³	y	0.0077	m
b	0.185	m	h	0.00405	m
R	0.306	m	EI	1.13	Nm²
k_{Gt}	5.4×10^6	N/m²	k_v	3.47×10^5	N/m²
k_w	9.57×10^5	N/m²	$c_w = c_v$	0	Ns/m²

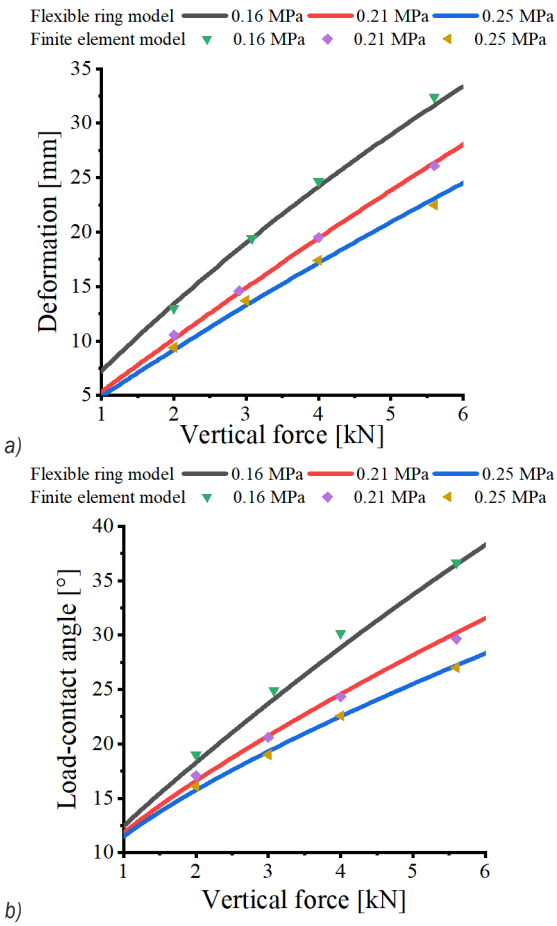

Fig. 9. *Comparison of the results obtained using the finite-element method and flexible ring model; a) load-deformation; and b) load-contact angle*

The detailed identification method for the flexible ring model is illustrated in [24]. Specifically, the geometric parameters of the flexible ring are obtained according to the cross-section of the pneumatic tire; the stiffness parameters are identified using modal test and load-sinkage test; the damping parameters are identified by varying the initial damping parameters and minimizing the error of contact angle between the simulated strains and the numerical ones using tire finite element analysis. The identified flexible ring model parameters are listed in Table 1. A comparison of the analytical results with the simulation results is shown in Fig. 9, which indicates the feasibility of the flexible ring model.

The model parameters presented in Table 1 indicate that the ring model can predict tire longitudinal forces when the vertical load is 4000 N, the friction coefficient is 0.7, the rolling velocity is 70 km/h, and the slip ratio is from -20 % to 20 %. Fig. 10 displays the longitudinal tire force calculated using Eq. (13) and the radial deformations of the neutral surface calculated using Eq. (15). It can be seen that when the longitudinal force is 0, the deformations in the front and rear contact areas are approximately equal, and the radial deformation exhibits a symmetrical distribution. According to Fig. 3, when the longitudinal force is positive, the radial deformation of the front contact area is smaller than that of the rear contact area. When the longitudinal force is negative, the deformation of the front contact area is larger than that of the rear contact area. Moreover, the larger the longitudinal force, the greater the asymmetry. It is noted that the longitudinal force has little effect on the radial deformation of the centre of the tire contact patch.

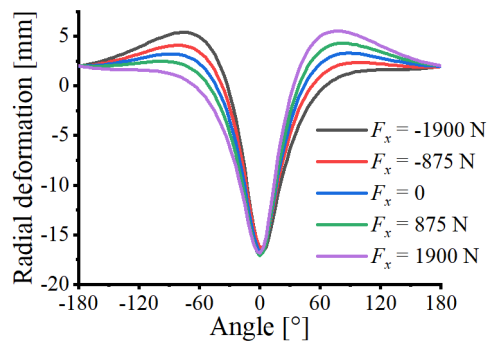

Fig. 10. *Simulated deformation under different longitudinal forces with the vertical load 4000 N*

Xiong and Tuononen [17] utilized a laser-based tire sensor system for measuring tire deformation and compared the measured radial deformations under different longitudinal forces; the test results are shown in Fig. 11. As seen in Fig. 11, increasing tire longitudinal force will lead to decrease in the radial deformation of the front contact area and increase in the radial deformation of the rear contact area. Under the conditions that the longitudinal force 0 N, 875 N and 1900 N, and comprehensive change trend analysis

of the comparison between the simulation result in Fig. 10 and the measured result in Fig. 11, although vertical tire force is different, the radial deformation trends of simulation results were the same as the measured results, it can be seen that the flexible ring model established in the study is accurate and credible.

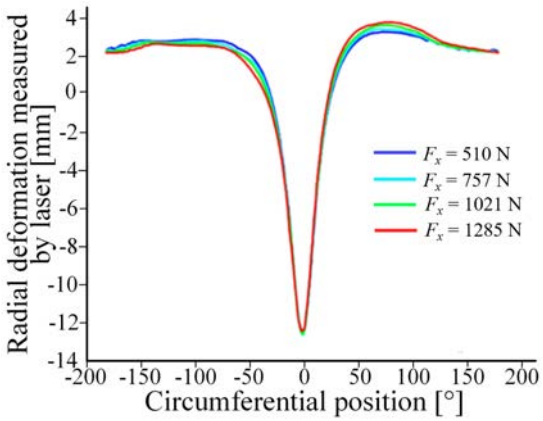

Fig. 11. *Measured radial deformations under different longitudinal forces with the vertical load 3000 N* [17]

The circumferential strain of the neutral surface, which is calculated using Eq. (16), is illustrated in Fig. 12. When the longitudinal force is 0, the strain in the front and rear contact areas is approximately equal, and the strain curve displays symmetric distribution. When the longitudinal force is positive, the circumferential strain of the front contact area is less than that of the rear contact area. When the longitudinal force is negative, the circumferential strain of the front contact area is larger than that of the rear contact area. Thus, the longitudinal force causes asymmetric strain distribution in the front and rear areas of the tire. As the longitudinal force increases, the asymmetry of the strain curve also increases. However, the longitudinal force has almost no effect on the maximum tensile strain.

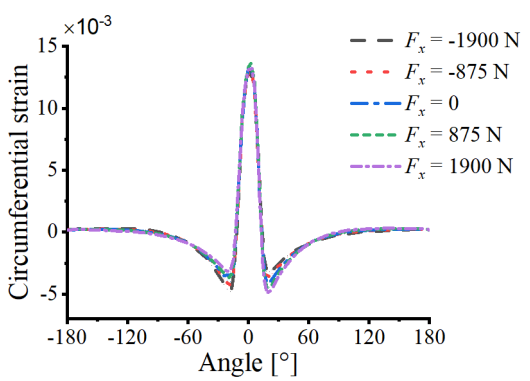

Fig. 12. *Circumferential strain under different longitudinal forces*

The variation in the circumferential strain distribution with the longitudinal force can be used to identify the driving conditions of the tire. The front and rear contacts of the tire are displayed in Fig. 13, in which the tire's rolling direction is considered the positive direction. The peak circumferential strain at the front contact is denoted by CP_f, and the peak circumferential strain at the rear contact is denoted by CP_r. The tire conditions can be defined using the different relationships between CP_f and CP_r, as shown in the following travel state. Comprehensive analysis of the coordinate directions in Fig. 2 and the longitudinal forces in Fig. 12 indicates that the tire is in the driving condition when the longitudinal forces are negative and that the tire is in the braking condition when the longitudinal forces are positive.

$$\begin{cases} CP_f \approx CP_r & \text{Free rolling} \\ CP_f < CP_r & \text{Braking} \\ CP_f > CP_r & \text{Driving} \end{cases}.$$

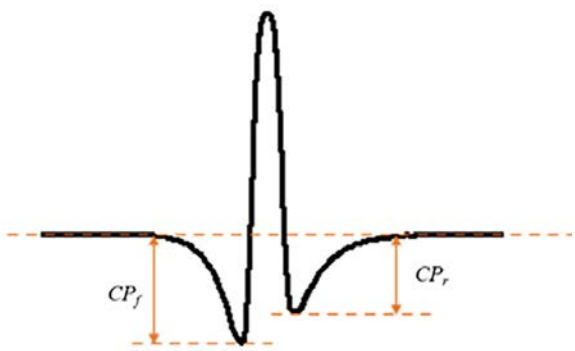

Fig. 13. *Circumferential strain distribution of the neutral surface*

2.2 Characteristic Analysis of Radial Deformation

To analyse the asymmetry in the neutral surface's radial deformation caused by the longitudinal force, the radial deformation is defined as follows. The 0° coordinate position of the contact patch centre is taken as the midpoint along the rolling direction; thus, the front region comprises negative angles, and the rear region comprises positive angles (Fig. 14). The angle range in the front area is denoted $N_{\phi f}$, whereas that in the rear area is denoted $N_{\phi r}$. An angle ϕ_j, (j=1, ..., $N_{\phi f}$) in the front area corresponds to an angle $-\phi_j$, (j=1, ..., $N_{\phi r}$) in the rear area. The radial deformation of the angle ϕ_j in the front area is denoted $w(\phi_j)$, and the radial deformation of the angle $-\phi_j$ in the rear area is denoted $w(-\phi_j)$. According to the radial deformation characteristics displayed in Fig. 4, if the longitudinal

force is equal to 0, $w(\phi_j)=w(-\phi_j)$. If the longitudinal force is not equal to 0, $w(\phi_j)\neq w(-\phi_j)$. Therefore, the difference between $w(\phi_j)$ and $w(-\phi_j)$ (denoted as Δw) is used to characterize the degree of asymmetry of the radial deformation. According to the tire rolling direction, Δw can be expressed as follows:

$$\begin{cases} \Delta w(\phi_j) = w\left(\phi_j\right) - w\left(-\phi_j\right) & -\pi \le \phi_j \le 0 \\ \Delta w(-\phi_j) = w\left(-\phi_j\right) - w\left(\phi_j\right) & 0 \le -\phi_j \le \pi \end{cases}. \quad (19)$$

Eq. (19) indicates that the deformation differences in the front and rear areas have the same magnitude but in the opposite direction.

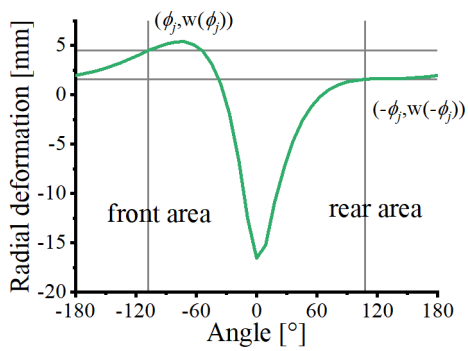

Fig. 14. *Radial deformation of the ring neutral surface*

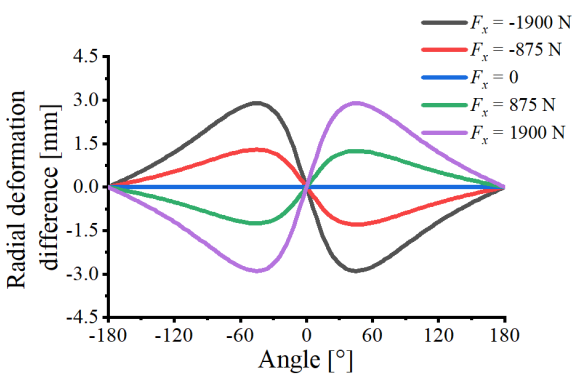

Fig. 15. Curves of $\Delta\omega$ under different longitudinal forces

To analyse the effect of the longitudinal force on the radial deformation difference $\Delta\omega$, the longitudinal dynamic model of the thin ring is analysed under a vertical load of 4000 N, a friction coefficient of 0.7, roll velocity of 70 km/h, and slip rate range of –20 % to 20 %. The analytical results are displayed in Fig. 15. When the longitudinal force is equal to 0, the $\Delta\omega$ is also equal to 0. When the longitudinal force is positive, the radial deformation difference in the front area is negative, and that in the rear area is positive. When the longitudinal force is negative, the radial deformation difference in the front area is positive, and that in the rear area is negative. As the longitudinal force increases, the change in the radial deformation difference curve increases.

2.3 Analysis of the Circumferential Strain Characteristics

To analyse the effect of the vertical force on the radial deformation difference under the same longitudinal force, the following boundary conditions were adopted: vertical load range of 2900 N to 5600 N, friction coefficient range of 0 to 0.7, and slip rate of 20 %. Because of the high slip rate, the tread brushes are in the slipping zone. The friction coefficient can be changed under different vertical forces to obtain the longitudinal force (2000 N). The effect of the vertical force on the radial deformation difference between the front and rear areas is displayed in Fig. 16. The results indicate that the vertical force has almost no influence on the radial deformation difference. Thus, the radial deformation difference between the front and rear areas is mainly affected by the longitudinal force.

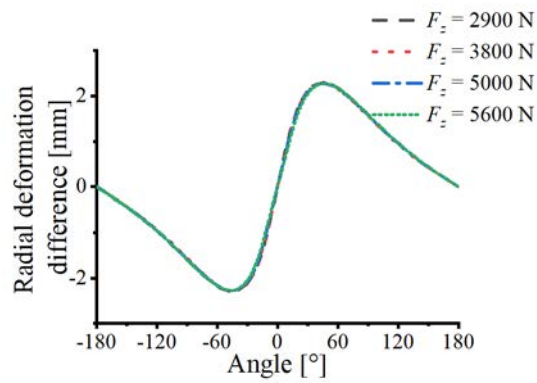

Fig. 16. *Curves of $\Delta\omega$ under different vertical forces*

The circumferential strain difference $\Delta\varepsilon_\theta$ between the front and rear regions can be defined by using the method for determining the radial deformation difference between these regions. The curves of circumferential strain difference under the same conditions as those used for analysing the radial deformation difference are displayed in Fig. 17. When the longitudinal force is equal to 0, the difference in the circumferential strain of the front and rear areas is also 0. When the longitudinal force is positive, the maximum value of the circumferential strain difference curve is in the front area and its minimum value is in the rear area. The variation of the circumferential strain difference increases with an increase in the longitudinal force.

The curves of circumferential strain difference for different vertical forces under the same longitudinal

force are displayed in Fig. 18. The variation in the circumferential strain difference does not change significantly with an upsurge in the vertical force. Thus, the circumferential strain difference between the front and rear areas is mainly affected by the longitudinal force.

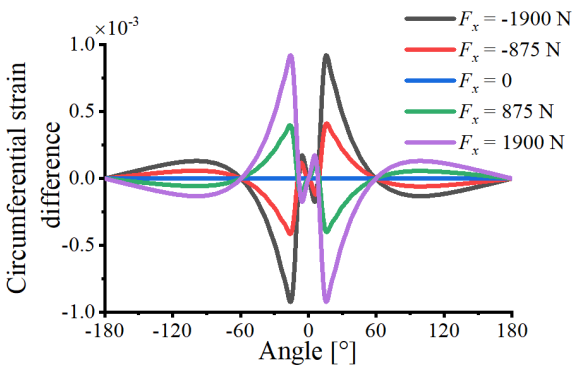

Fig. 17. *Curves of $\Delta\varepsilon_\theta$ under different longitudinal forces*

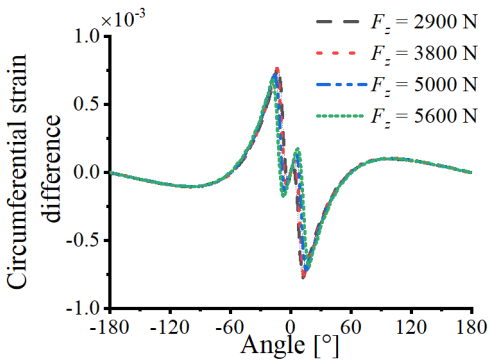

Fig. 18. *Curves of $\Delta\varepsilon_\theta$ under different vertical forces*

2.4 Characteristic Curve Index

The difference in the radial deformation and circumferential strain between the front and rear regions reflects the degree of asymmetry of the deformation and strain, respectively. To quantitatively analyse the relationship between the radial deformation difference or circumferential strain difference and the longitudinal force, this study employed the difference curve area, which was defined as the area under the curve obtained by setting the radial deformation difference or circumferential strain difference as the vertical coordinate and the tire angle as the horizontal coordinate. A tire is assumed to pass through point P at equal intervals over one revolution; thus, the difference area of the tire revolution can be expressed as follows:

$$A_\omega = \sum_{i=1}^{P} \Delta\omega(\phi_i)\Delta\phi, \quad A_\varepsilon = \sum_{i=1}^{P} \Delta\varepsilon_\theta(\phi_i)\Delta\phi, \quad (20)$$

where $\Delta\phi$ is the interval angle between two discrete points, A_ω is the area of the difference curve of the radial deformation, and A_ε is the area of the difference curve of the circumferential strain.

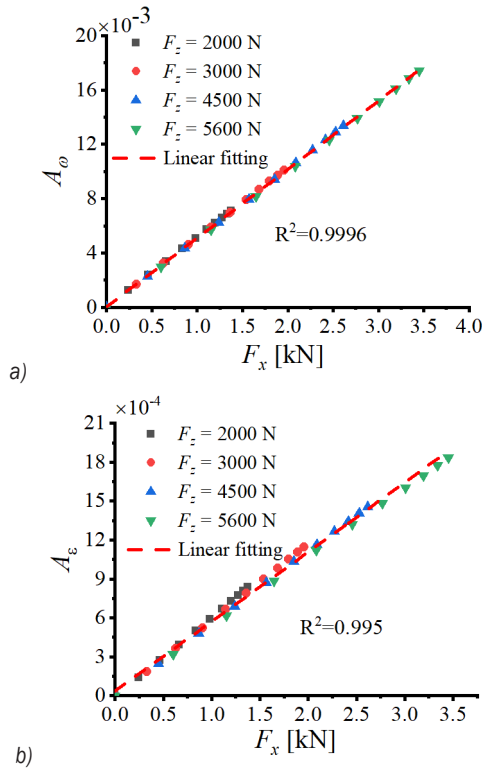

Fig. 19. *Relationship between the difference curve area and longitudinal tire force; a) relationship between A_ω and F_x; and b) relationship between A_ε and F_x*

To quantitatively analyse the effect of the longitudinal force on the difference curve area, the difference curve area of the radial deformation difference and circumferential strain difference curves were calculated using Eq. (20) under the following conditions: friction coefficient of 0 to 0.7, roll velocity of 70 km/h, vertical load range of 2000 N to 5600 N, and slip rate range of 0 % to 20 %. Fig. 19a indicates that A_ω has a linear relationship with the longitudinal force, and the correlation coefficient for this relationship is 0.9996. Fig. 19b indicates that A_ε has a linear relationship with the longitudinal force, and the correlation coefficient for this relationship is 0.995. It can be inferred from Fig. 19 that the vertical force has little influence on A_ω and A_ε. Theoretically, the A_ω and A_ε can be used as a tire signal to estimate tire longitudinal force. Nevertheless, previous research related to the intelligent tires indicates that the strain sensors meet the requirements to achieve and advance intelligent tire system by means of strain

measurement, and the strain sensors are gaining attention due to their low cost, robustness and high reliability in their measurements and applications [25]. Therefore, it is feasible to use the A_ε calculated by the strain signal as an index to estimate tire longitudinal force.

3 ESTIMATION ALGORITHM OF A LONGITUDINAL FORCE

3.1 Finite-Element Tire Model

Because the finite-element tire model established in this study was used only to identify the model parameters and verify the tire estimation algorithm, the model was constructed only considering the longitudinal pattern of the tire. The details of the tire model method were detailed previously in [26] and [27]. To improve the calculation accuracy of the contact area, the grid of the contact area was refined. When performing rotation to generate a three-dimensional grid, the rotation angle of the grid near the lower half of the tire's contact area was 1° with 60 pitches, and the rotation angle over the remaining angle was 5° with 60 pitches. The tire model is illustrated in Fig. 20; the total number of elements was 211,585, and the total number of nodes was 227,546. The rim and road surface were defined as rigid analytical bodies, and the tire model was loaded and free-rolled. The tire loading process was implemented by applying road surface displacement.

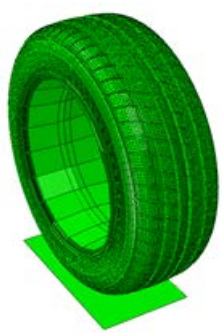

Fig. 20. *Tire Finite element model*

3.2 Longitudinal Force Estimation Algorithm

The overall framework of the intelligent tire longitudinal force estimation algorithm is displayed in Fig. 21. The input of the algorithm is the circumferential strain of the longitudinal centerline of the inner liner. In the signal processing part of the algorithm, A_ε is calculated using the circumferential strain. In the output part of the algorithm, the linear regression model is used to output the longitudinal tire force.

The linear regression model uses a unary linear function, and the longitudinal force of the tire is considered to be a linear function of A_ε. The regression model is expressed as follows:

$$F_x = a \cdot A_\varepsilon + b, \tag{21}$$

where a and b are the fitting parameters to be identified.

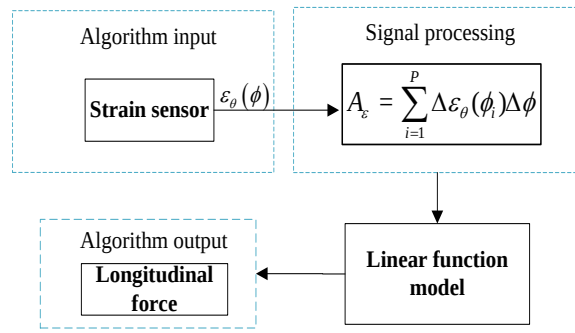

Fig. 21. *Flowchart for longitudinal force estimation method*

To conduct parameter identification for the linear function and verify the longitudinal force estimation algorithm, the longitudinal forces were simulated using a finite element model under different schemes, as shown in Table 2.

Table 2. *Finite element simulation schemes*

Schemes	Vertical force [N]	Slip ratio [%]
1	2000	3, 6, 9, 12, 20
2	2900	3, 6, 9, 12, 20
3	4000	3, 6, 9, 12, 20
4	5600	3, 6, 9, 12, 20

The finite-element simulation results provided the longitudinal forces corresponding to different slip rates. Schemes 1 and 3 were used to identify the fitting parameters of the linear function. The difference curve area A_ε was calculated using the circumferential strain obtained through finite-element simulation. The following fitting parameters were obtained by linearly fitting the longitudinal force obtained from the finite-element simulation: $a = 1.96 \times 10^6$, $b = -28.35$. The longitudinal force values obtained using schemes 2 and 4 were used to verify the predicted results. Fig. 22 displays a comparison of the estimated and simulated longitudinal force. The results indicate that when the longitudinal force was less than 400 N, the estimated error was 20 % because the asymmetry of the strain was not considered when the longitudinal force was

small. However, when the longitudinal force was greater than 400 N, the estimated error decreased and is lower than 10 %. The main source of this error was the error in the strain simulation result caused by the finite-element mesh density. Because the nodal strain of Abaqus software was obtained from a geometric equation, the integral point strain was obtained from the extrapolation of the integral point stress. Moreover, different results are usually obtained when extrapolating the tensor of the integral point from multiple elements to the shared node. Therefore, the accuracy of the finite-element strain analysis results was relatively low, and the estimated longitudinal force exhibited a large error.

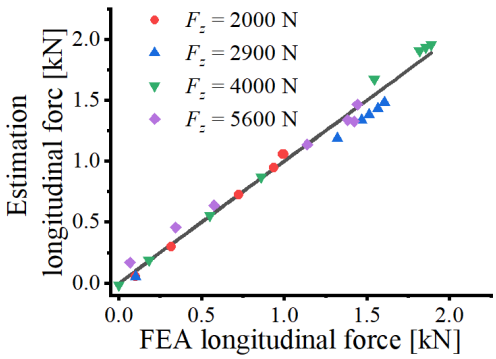

Fig. 22. *Comparison of the longitudinal force estimated and simulated under different vertical force*

4 CONCLUSION

This study established an algorithm for estimating the longitudinal tire force using the physics-based model. The following conclusions were drawn from this study:

1. A longitudinal dynamic tire model based on the flexible ring model and brush model was established, and the deformation and strain of the ring were obtained under different vertical and longitudinal forces. Due to the inextensibility of the high strength tire carcass, the radial deformations of tire carcass will not only result into tangential deformations but also results into circumferential stress and strain. The longitudinal force is the primary reason for the asymmetric distribution of the radial deformation and circumferential strain of the tire. Moreover, the greater the longitudinal force, the larger the asymmetry of the radial deformation and circumferential strain. The radial deformation difference $\Delta\omega$ and the circumferential strain difference $\Delta\varepsilon_\theta$ between the front and rear regions are proposed to describe the asymmetry quantitatively.
2. The difference curve area of radial deformation A_ω and the difference curve area of circumferential strain A_ε are proposed to study the effects of the longitudinal force on the tire deformation and strain, and the results show that the A_ω and A_ε have a strong linear relationship with the longitudinal tire forces under the different vertical loads and slip ratios. With these results, theA_ω and A_ε can be used to estimate the longitudinal force acting on the tire.
3. Considering the low cost, robustness, and high reliability of the strain gauges in their measurements, tire circumferential strain information in this study is more suitable for estimating the longitudinal tire force. To establish the relationship between the circumferential strain and longitudinal force, a tire longitudinal force estimation algorithm was proposed, and the model parameters were also identified. From the simulation results under different vertical forces and slip ratios, the reliability of the proposed algorithm was validated. However, it is necessary to develop a practical intelligent tire based on strain. Experiments to reveal the relationship between tire strain and longitudinal force, and the determination of the strain sensor location, are objectives that remain for future study.

5 ACKNOWLEDGEMENTS

The author(s) disclosed receipt of the following financial support for the research, authorship, and/or publication of this article: this work was jointly supported by the National Natural Science Foundation of China (Grant No. 52072156 and No. 51675240), Jiangsu provincial Six Talent Peaks (Grant No. JXQC-011), and Postdoctoral Foundation of China(2020M682269).

6 NOMENCLATURES

R	mean radius of ring, [m]
$\overline{R}$	free radius of ring, [m]
Ω	angular speed, [rad/s]
h	the thickness of the ring, [m]
K_ω	radial stiffness of sidewall, [N/m²]
K_v	tangential stiffness of sidewall
K_{Et}	radial stiffness of tread
K_{Gt}	tangential stiffness of tread, [N/m²]
w	radial displacement of the neutral axis, [m]
v	tangential displacement of the neutral axis, [m]

c_w radial damping of sidewall, [Ns/m^2]
c_v tangential damping of sidewall, [Ns/m^2]
EI stiffness of the ring, [Nm^2]
ρ equivalent density of the ring [kg/m^3]
b the width of the ring, [m]
τ depth of tire, [m]
q_w radial external force on ring, [N]
q_v tangential external force on ring, [N]
u_r displacement in radial direction, [m]
u_r displacement in circumferential direction, [m]
y distance from the neutral ring, [m]

7 REFERENCES

[1] Coppo, F., Pepe, G., Roveri, N., Carcaterra, A. (2017). A multisensing setup for the intelligent tire monitoring. *Sensors*, vol. 17, no. 3, art. ID 576, **DOI:10.3390/s17030576**.

[2] Du, X.B., Zhao, Y.Q., Wang, Q., Fu, H.X., Lin, F. (2019). Grounding characteristics of a non-pneumatic mechanical elastic tire in a rolling state with a camber angle. *Strojniški vestnik - Journal of Mechanical Engineering*, vol. 65, no. 5, p. 287-296, **DOI:10.5545/sv-jme.2018.5845**.

[3] Khaleghian, S., Emami, A., Taheri, S. (2017). A technical survey on tire–road friction estimation. *Friction*, vol. 5, no. 2, p. 123-146, **DOI:10.1007/s40544-017-0151-0**.

[4] Lee, H., Taheri, S. (2017). Intelligent Tires? A review of tire characterization literature. *IEEE Intelligent Transportation System Magazine*, vol. 9, no. 2, p. 114-135, **DOI:10.1109/MITS.2017.2666584**.

[5] Xiong, Y., Yang, X.G. (2018). A review on in-tire sensor systems for tire–road interaction studies. *Sensors Review*, vol. 38, no. 2, p. 231-238, **DOI:10.1108/SR-07-2017-0132**.

[6] Mendoza-Petit, M.F., García-Pozuelo, D., Díaz, V., Olatunbosun, O. (2020). A strain-based intelligent tire to detect contact patch features for complex maneuvers. *Sensors*, vol. 20, no. 6, art. ID 1750, **DOI:10.3390/s20061750**.

[7] Ley-Rosas, J.J., Gonzalez-Jimenez, L.E., Loukianov, A.G., Ruiz-Duarte, J.E. (2019). Observer based sliding mode controller for vehicles with roll dynamics. *Journal of the Franklin Institute*, vol. 356, no. 5, p. 2559-2581, **DOI:10.1016/j.jfranklin.2018.11.031**.

[8] Kunjunni, B., bin Zakaria, M.A., Majeed, A.P.P., Nasir, A.F.A., Hamid, U.Z.A. (2020). Effect of load distribution on longitudinal and lateral forces acting on each wheel of a compact electric vehicle. *SN Applied Ences*, vol. 2, art ID 244, **DOI:10.1007/s42452-020-1996-9**.

[9] Yang, X., Olatunbosun, O., Ramos, D.G.P., Bolarinwa, E. (2013). Experimental investigation of tire dynamic strain characteristics for developing strain-based intelligent tire system. *SAE International Journal of Passenger Cars-Mechanical Systems*, vol. 6, no. 1, p. 97-108, **DOI:10.4271/2013-01-0633**.

[10] Matsuzaki, R., Todoroki, A. (2009). Intelligent tires for improved tire safety based on strain measurements, health monitoring of structural and biological systems 2009. *Proceedings SPIE*, vol. 7295, **DOI:10.1117/12.815403**.

[11] Zhao, J., Lu, Y.H, Zhu, B., Liu, S. (2018). Estimation algorithm for longitudinal and vertical forces of smart tire with accelerometer embedded. *Automotive Engineering*, vol. 40, no. 2, p. 137-142, **DOI:10.19562/j.chinasae.qcgc.2018.02.003**. (in Chinese)

[12] Zhu, X.L., Lu, D. (2017). A 'smart tire' for estimating the tire force and the extents of the influences of specific factors. *Proceedings of the Institution of Mechanical Engineers, Part D: Journal of Automobile Engineering*, vol. 231, no. 13, p. 1848-1857, **DOI:10.1177/0954407016685633**.

[13] Zhang, Y., Yi, J. (2014). Static tire/road stick–slip interactions: Analysis and experiments. *IEEE/ASME Transactions on Mechatronics*, vol. 19, no. 6, p. 1940-1950, **DOI:10.1109/TMECH.2013.2292872**.

[14] Zhang, Y., Yi, J., Liu, T. (2013). Embedded flexible force sensor for in-situ tire–road interaction measurements. *IEEE Sensors Journal*, vol. 13, no. 5, p. 1756-1765, **DOI:10.1109/JSEN.2013.2241051**.

[15] Yi, J., (2008). A piezo-sensor-based "smart tire" system for mobile robots and vehicles. *IEEE/ASME Transactions on Mechatronics*, vol. 13, no. 1, p. 95-103, **DOI:10.1109/TMECH.2007.915064**.

[16] Garcia-Pozuelo, D., Yunta, J., Olatunbosun, O., Yang, X., Diaz, V. (2017). A strain-based method to estimate slip angle and tire working conditions for intelligent tires using fuzzy logic. *Sensors*, vol. 17, no. 4, p. 874-891, **DOI:10.3390/s17040874**.

[17] Xiong, Y., Tuononen, A. (2015). The in-plane deformation of a tire carcass: Analysis and measurement. *Case Studies in Mechanical Systems and Signal Processing*, vol. 2, p. 12-18, **DOI:10.1016/j.csmssp.2015.09.001**.

[18] Garcia-Pozuelo, D., Olatunbosun, O., Strano, S., Terzo, M. (2019). Areal-time physical model for strain-based intelligent tires. *Sensors and Actuators, A: Physical*, vol. 288, p. 1-9, **DOI:10.1016/j.sna.2018.12.010**.

[19] Wei, Y.T., Nasdala, L., Rothert, H. (2009). Analysis of forced transient response for rotating tires using ref models. *Journal of Sound and Vibration*, vol. 320, no. 1-2, p. 145-162, **DOI:10.1016/j.jsv.2008.07.007**.

[20] Kim, S.J., Savkoor, A.R. (1996). The contact problem of in-plane rolling of tires on a flat road. Vehicle System Dynamics, vol. 27, p. 189-206, **DOI:10.1080/00423119608969654**.

[21] Liu, Z., Zhou, F.Q., Oertel, C., Wei, Y.T. (2017). Three-dimensional vibration of a ring with a noncircular cross-section on an elastic foundation. *Proceedings of the Institution of Mechanical Engineers, Part C: Journal of Mechanical Engineering Science*, vol. 232, no. 13, p. 2381-2393, **DOI:10.1177/0954406217720823**.

[22] Guo, K.H. (2016). Untire:Untire tire model. *Journal of Mechanical Engineering*, vol. 52, no. 12, p. 90-99, **DOI:10.3901/JME.2016.12.090**. (In Chinese)

[23] Nishihara, O., Masahiko, K. (2011). Estimation of road friction coefficient based on the brush model. *Journal of Dynamic Systems, Measurement, and Control*, vol. 133, no. 4, **DOI:10.1115/1.4003266**.

[24] Han, T. (2020). *Study on tire force estimation method of intelligent tires by using flexible ring model*. MSc Thesis, Jiangsu University. (in Chinese).

[25] Garcia-Pozuelo, D., Olatunbosun, O., Yunta, J., Yang, X., Diaz, V. (2017). A novel strain-based method to estimate tire conditions using fuzzy logic for intelligent tires. *Sensors*, vol.17, no. 2, p. 350-366, **DOI:10.3390/s17020350**.

[26] Zhou, H.-C., Wang, G.-L., Yang, J., Xue, K.-X. (2015). Numerical simulation of the effect of bionic v-riblet non-smooth surface on tire anti-hydroplaning. *Journal of Central South University*, vol. 22, p. 3900-3908, **DOI:10.1007/s11771-015-2934-7**.

[27] Yang, J., Wang, G.L., Wan, Z.J., Liang, C., Zhou, H.C. (2016). Non-natural equilibrium contour design for radial tire and its influence on tire performance. *International Journal of Automotive Technology*, vol. 17, no. 4, p. 639-649, **DOI:10.1007/s12239-016-0063-4**.

Strojniški vestnik - Journal of Mechanical Engineering 67(2021)4, 167-179

DOI:10.5545/sv-jme.2021.7106 Original Scientific Paper
Received for review: 2021-01-23
Received revised form: 2021-02-21
Accepted for publication: 2021-03-22

Optimization of the Internal Roller Burnishing Process for Energy Reduction and Surface Properties

Trung-Thanh Nguyen[1] – Minh-Thai Le[2,*]

[1] Le Quy Don Technical University, Faculty of Mechanical Engineering, Vietnam
[2] Le Quy Don Technical University, Faculty of Special Equipments, Vietnam

Improving the surface quality after burnishing operation has been the subject of various published investigations. Unfortunately, the trade-off analysis between the energy consumption and surface characteristics of the internal burnishing has been not addressed due to the expensive cost and huge efforts required. The objective of the present work is to optimize burnishing factors, including the spindle speed, burnishing feed, depth of penetration, and the number of rollers for minimizing the energy consumed in the burnishing time, as well as surface roughness and maximizing Rockwell hardness. An adaptive neuro-based-fuzzy inference system (ANFIS) was used to develop burnishing objectives in terms of machining parameters. The optimization outcomes were selected using an evolution algorithm, specifically the non-dominated sorting particle swarm optimization (NSPSO). The results of the proposed ANFIS models are significant and can be employed to predict response values in industrial applications. The optimization technique comprising the ANFIS and NOPSO is a powerful approach to model burnishing performances and select optimal parameters as compared to the trial and error method as well as operator experience. Finally, the optimal solution can help to achieve the improvements in the energy consumed by 16.3 %, surface roughness by 24.3 %, and Rockwell hardness by 4.0 %, as compared to the common values .

Keywords: roller burnishing; energy reduction; roughness; Rockwell hardness; optimization

Highlights

- *Optimizing machining parameters for the internal roller burnishing process of the hardened steel 40X.*
- *Considering the spindle speed, burnishing feed, burnishing depth, and number of the rollers.*
- *Evaluating energy consumption, surface roughness, and Rockwell hardness.*
- *Development of the correlations using ANFIS models.*
- *Determination of optimal parameters using NSPSO.*

0 INTRODUCTION

The burnishing operation is an effective solution to boost the surface properties of the machined parts. The outstanding characteristics of the burnished surface, such as reduced roughness, increased hardness, and enhanced compressive stress, can be obtained with the aid of the burnishing process. The optimal factors of different burnishing operations have been selected for improving machining responses. El-Taweel and El-Axir **[1]** revealed that the burnishing performances, such as the surface roughness and micro-hardness, were primarily affected by the force, feed, speed, and the number of passes, respectively. A roughness of 0.055 μm and hardness of 46.69 HRC for the burnished T215Cr12 material were obtained with the aid of the response surface method **[2]**. Babu et al. **[3]** stated that the burnishing depth significantly increased the micro-hardness, while the average roughness was primarily influenced by the burnishing force for the burnishing processes of the EN steels, aluminium alloy, and alpha-beta brass. Tadic et al. **[4]** emphasized that a small burnishing force significantly contributed to a lower roughness. Cobanoglu and Ozturk **[5]** indicated that the average roughness and micro-hardness were enhanced by 100.0 % and 55.50 %, as compared to the initial values for the burnished AISI 1040 steel. John and Vinayagam **[6]** revealed that the optimum values of the roughness and hardness of the burnished Al 63400 were 0.032 μm and 91.63 HV, respectively.

Revankar et al. **[7]** presented that the improvements in the surface roughness and micro-hardness were 77.0 % and 17.0 %, as compared to pre-machined properties for the burnished titanium alloy. Amdouni et al. **[8]** indicated that the burnishing crossed path could be effectively used to decrease the roughness, while the successive one was an alternative solution to increase the hardness for the burnished aluminium alloy. John et al. **[9]** emphasized that the average roughness could be decreased by 94.5 %, and the micro-hardness could be increased by around 41.7 % for the burnishing process of EN-9 alloy. Similarly, the impacts of the processing conditions on the average roughness bore size, and the ovality of the internal roller burnishing were presented by John et al. **[10]**. The findings revealed that a burnished hole with an acceptable accuracy was produced. Świrad et al. **[11]** stated that the raster strategy was an effective solution for machining curved paths, while

*Corr. Author's Address: Le Quy Don Technical University, 236 Hoang Quoc Viet, Ha Noi, Vietnam, thaileminh@lqdtu.edu.vn

the burnishing pressure had a positive impact on the improvement of the burnished surface.

Huuki and Laakso [12] indicated that the compressive stress and average roughness could be improved by 90 % and 400 %, while the roundness was enhanced by 38 % for the ultrasonic burnishing of 34CrNiMo6-M steel. The regression models of the surface roughness and micro-hardness for the ultrasonic-assisted burnishing process of the aluminium alloy were developed by Teimouri et al. [13]. The authors concluded that the proposed approach could bring a higher value of the affected depth. Yang et al. [14] indicated that the cryogenic condition significantly contributed to a decreasing burnishing force and roller wear, enhancing microstructure and hardness, as compared to the dry one for the burnishing of the Co–Cr–Mo biomaterial. Tang [15] agreed that the surface roughness, microstructure, and corrosion resistance of the burnished titanium alloy were improved with cryogenic cooling. Sachin et al. [16] stated that cryogenic burnishing effectively improved surface properties. A new burnishing process was developed to produce the drill shank for minimizing machining costs, resources, and energy [17]. The author stated that the proposed process can replace conventional operations, including heat treatment and grinding. Maximov et al. [18] emphasized that diamond burnishing is an effective approach to enhance the fatigue limits and decrease the surface roughness.

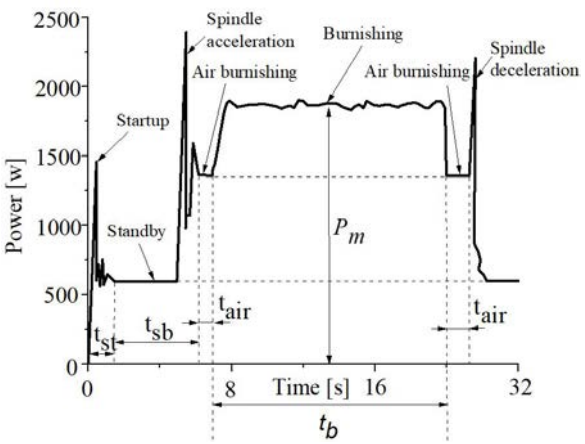

Fig. 1. *The power used for the burnishing process*

Unfortunately, the influences of machining parameters on the energy consumed for the internal burnishing operation have not been analysed. Furthermore, the relation between the energy reduction and surface properties for the burnishing process has not considered.

1 METHODS

1.1 Optimizing Objectives

Fig. 1 presents the graph of the power used for the burnishing process. The energy components include the start-up energy (E_s), standby energy (E_b), transition energy (E_t), air-burnishing energy (E_a), and the burnishing energy (E_{be}).

The start-up state refers to the shortest period for turning on the machine tool. The standby state presents the stable period, which starts from turning on the machine tool and stops by the spindle rotation. During this time, the lowest amount of energy is consumed. The spindle acceleration/deceleration state refers to the short period for increasing and decreasing the spindle speed. The air-burnishing energy state presents the steady period with spindle rotation but no material burnishing. The burnishing state refers to the steady period for material burnishing.

Practically, the start-up energy, standby energy, transition energy, and air-burnishing energy are less dependent on the variety of machining parameters; hence, the energy consumed in the burnishing state is considered to be an optimization objective. The energy consumed in the burnishing time is calculated as:

$$E_{be} = P_m \times t_b, \tag{1}$$

where P_m is the power consumed in the burnishing time; and t_b is the burnishing time.

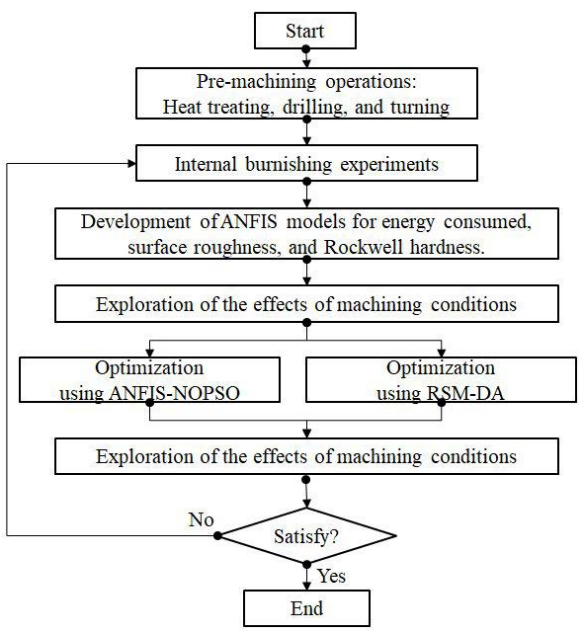

Fig. 2. *Optimization approach*

A decreased surface roughness has a significant contribution to the functional performance of mechanical parts and production costs. In the roughness criteria, average roughness (R_a) is considered to be a serious index of the product quality, which indicates the average of the absolute value along the sampling length. Maximum profile peak height (R_p) and Maximum profile valley depth (R_v) are the highest and lowest points along the sampling length, respectively. Practically, a decreased R_a leads to a reduction in the R_p and R_v.

The surface roughness (R_a) is calculated as:

$$R_a = \frac{\sum_{i=1}^{5} R_{ai}}{5}, \tag{2}$$

where R_{ai} presents the average roughness at the burnished surface.

The Rockwell hardness (*RH*) is calculated as:

$$RH = \frac{\sum_{i=1}^{5} RH_{ai}}{5}, \tag{3}$$

where RH_{ai} is the Rockwell hardness after the burnishing operation at the measured position.

Burnishing factors are presented in Table 1. These ranges are determined based on the characteristics of the burnishing tool, workpiece, and machine tool. These values are verified with the handbooks and aforementioned works.

Table 1. *Burnishing parameters*

Symbol	Parameters	1	2	3
S	Spindle speed [rpm]	1000	1500	2000
f	Feed rate [mm/min]	200	400	600
D	Burnishing depth [mm]	0.04	0.08	0.12
N	Number of rollers	2	3	4

1.2 Optimization Procedure

Fig. 2 presents the optimization approach, which is expressed as follows:

Step 1: The internal burnishing experiments using the Box-Behnken method (BBM) [19]. The BMM is an alternative design of the experimental method, in which a two-level factorial design is combined. Three required levels of each factor are "–1", "0", and "1", which presents the low, middle, and high ranges. The design points are placed on the middle points of the edge and the centre of the block. The BBD does not contain parametric combinations at their highest or lowest levels (at the vertices of the cube). This prevents the experiments from being performed under extreme conditions, which may cause unsatisfactory results. In other words, the extreme situations of the responses are avoided. In the BBM, the number of experiments is significantly decreased, which reduces experimental costs.

The number of experiments (*NE*) in the Box-Behnken method is calculated as:

$$NE = 2k(k-1) + C_p, \tag{4}$$

where k and C_p present the number of factors and the number of centre points, respectively.

Step 2: The ANFIS approach describes the impacts of input process parameters on the total energy consumed, surface roughness, and Rockwell hardness. The designed ANFIS model using five-layer feed-forward neural networks for the burnishing responses is expressed as follows (Fig. 3) [20] and [21]:

Layer 1: In this layer, the membership functions are assigned to the inputs. The outcome of this layer is expressed as:

$$LA_1^i = M_1^i = \mu_{Ai(x)}. \tag{5}$$

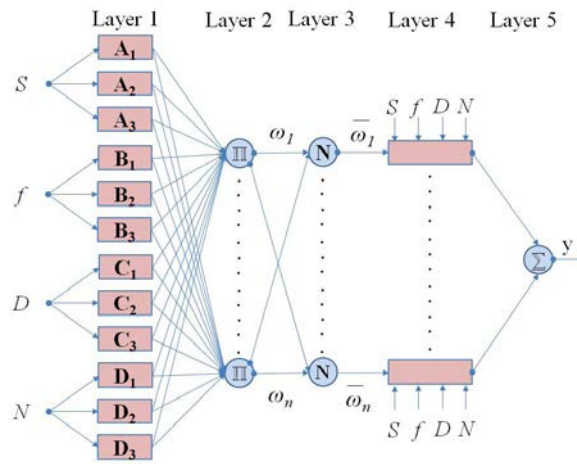

Fig. 3. *The typical structure of the ANFIS model*

Layer 2: This layer is applied to collect the inputs from the respective fuzzification nodes and determine the firing strength of the rule. The output is expressed as:

$$LA_2^i = \omega_i = \mu_{Ai}(x) \times \mu_{Bi}(y). \tag{6}$$

Layer 3: This layer is used to determine the ratio of the firing strength of a given rule to the total of firing strengths of all rules. The output is expressed as:

$$LA_3^i = \bar{\omega}_i = \frac{\omega_i}{\sum_{i=1}^{n} \omega_i}. \quad (7)$$

Layer 4: This layer is employed to defuzzify the received inputs and assign the consequent parameters of the rules. The output is expressed as:

$$LA_4^i = \bar{\omega}_i y_i = \bar{\omega}_i (a_i x + b_i x + c_i). \quad (8)$$

Layer 5: This layer is used to determine the overall output of all incoming signals. The output is expressed as:

$$LA_5^i = \sum_i \bar{\omega}_i f_i = \frac{\sum_i \omega_i f_i}{\omega_i}. \quad (9)$$

Step 3: The NOPSO is applied to select optimal factors.

NSPSO is an effective optimization algorithm to improve working efficiency and select non-dominated solutions [22]. Furthermore, NOPSO propels the population towards the Pareto-optimal front. Three niching approaches, including the crowding distance, niche count, and max-min operations, are applied to enhance the diversity of the Pareto front. The principal working of the NOPSO is shown in Fig. 4.

Step 4: The DA is applied to identify optimal values of process parameters and responses, in which each burnishing response is transformed into the function of the desirability (di) [23]. The desirability values are computed for three cases, including the maximum, minimum, and constrained objectives.

Step 5: The comparison of optimal results generated by two optimization approaches is evaluated.

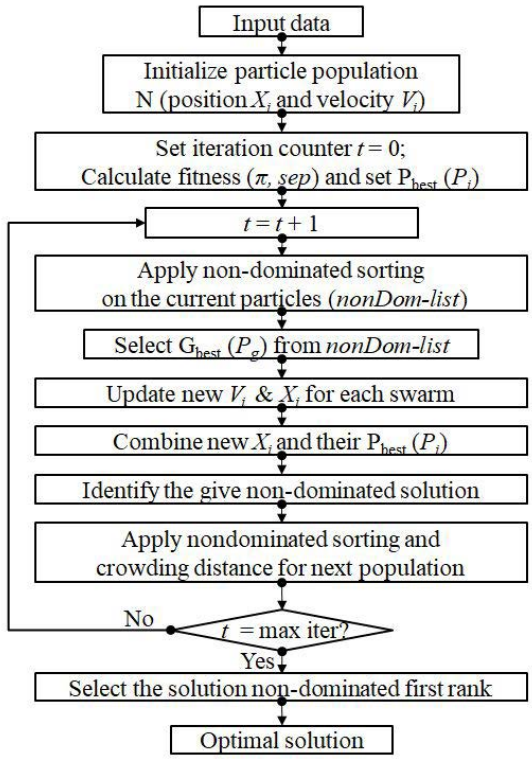

Fig. 4. *The principal working of the NOPSO*

2 EXPERIMENTAL

The round bar of a material labelled 40X steel is employed to produce machining specimens. The length of 50 mm, the internal diameter of 15 mm, and the diameter of 50 mm are used for all specimens. The average values of the surface roughness and Rockwell hardness of the pre-machined surface are 2.06 μm and 23.2 HRC, respectively.

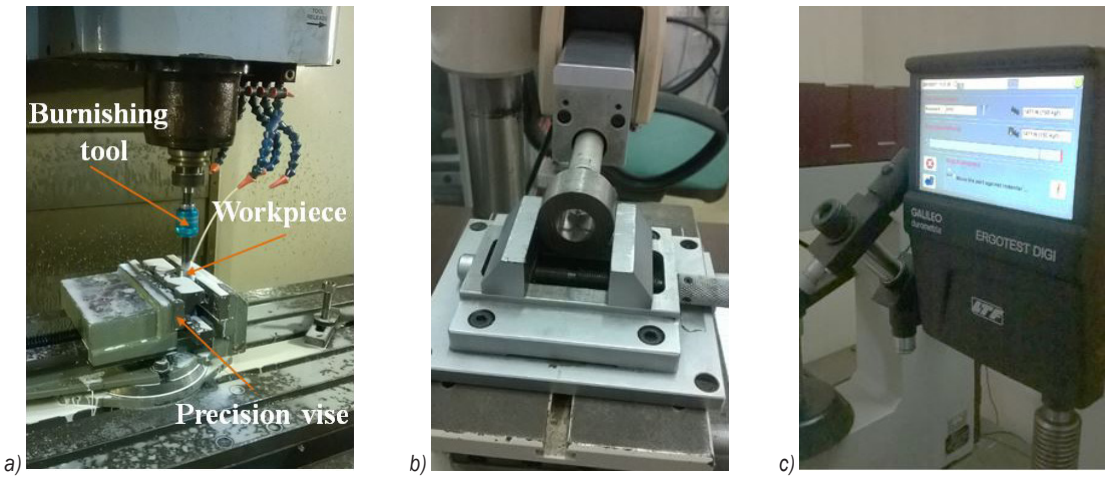

a) b) c)

Fig. 5. *a) Setting the origin of the workpiece; b) measuring roughness; and c) measuring hardness*

The burnishing trails are done with the support of a CNC milling machine. The burnishing tool is clamped on the machine spindle using the straight shank (Fig. 5a). The linear movement of the burnishing tool is performed with the aid of the Z-axis.

A KEW 6305 power meter is employed to measure power consumption. A reading error of ±0.3 % and full scale error of ±0.2 % are used to enhance the measure accuracy. Moreover, the display update period of 1 second is applied to visualize the capture data. A Mitutoyo SJ-301 tester is used to measure the surface roughness. The length of 4 mm is measured for each segment (Fig. 5b). The resolution of 0.1 μm is employed to improve the accuracy of the measuring data.

A ERGOTEST DIGI-25R tester is used to measure the Rockwell hardness. The pressed load of 150 kf and dwell time of 5 seconds are used for all hardness tests (Fig. 5c). The resolution of 0.1 Rockwell is applied to capture the experimental data.

Table 2. *Experimental data for the internal burnishing process*

	No.	S [rpm]	F [mm/min]	D [mm]	N	E_{be} [kJ]	R_a [μm]	RH [HRC]
Experimental data for developing ANFIS model	1	1000	400	0.08	4.00	16.97	0.37	38.2
	2	2000	400	0.08	2.00	18.59	0.63	37.8
	3	1000	400	0.08	2.00	16.08	0.39	33.5
	4	1500	400	0.04	4.00	17.16	0.37	39.1
	5	1500	400	0.08	3.00	17.47	0.37	42.7
	6	1000	600	0.08	3.00	11.73	0.58	37.1
	7	2000	600	0.08	3.00	13.09	0.68	42.7
	8	1500	200	0.08	2.00	32.59	0.31	34.3
	9	1500	400	0.08	3.00	17.49	0.36	42.4
	10	2000	400	0.08	4.00	18.69	0.43	43.5
	11	2000	200	0.08	3.00	35.24	0.46	37.3
	12	1500	600	0.12	3.00	13.01	0.52	41.0
	13	2000	400	0.12	3.00	19.79	0.53	41.1
	14	1500	200	0.12	3.00	34.86	0.34	36.4
	15	1500	400	0.04	2.00	15.91	0.47	34.7
	16	2000	400	0.04	3.00	17.33	0.58	36.8
	17	1000	200	0.08	3.00	31.33	0.33	32.6
	18	1500	200	0.08	4.00	33.56	0.21	38.7
	19	1500	600	0.08	4.00	12.65	0.46	43.6
	20	1500	400	0.12	2.00	18.46	0.42	39.3
	21	1500	400	0.12	4.00	18.53	0.32	44.1
	22	1000	400	0.04	3.00	15.81	0.51	31.8
	23	1500	200	0.04	3.00	30.91	0.39	33.2
	24	1000	400	0.12	3.00	16.99	0.46	36.2
	25	1500	600	0.04	3.00	11.74	0.57	36.6
	26	1500	600	0.08	2.00	12.09	0.56	39.2
Experimental data for testing accuracy of the ANFIS model	27	1200	200	0.06	2	30.58	0.34	30.4
	28	1400	300	0.06	2	22.47	0.37	35.2
	29	1600	400	0.08	3	17.72	0.38	42.9
	30	1800	500	0.08	3	14.15	0.49	43.5
	31	1800	500	0.10	4	14.64	0.37	45.6
	32	2000	600	0.10	4	13.22	0.52	44.2
	33	2000	600	0.12	4	13.39	0.46	43.9
	34	1300	450	0.07	3	14.64	0.41	40.7
	35	1700	550	0.09	4	13.25	0.39	45.4
	36	1900	550	0.11	3	13.84	0.52	42.9
	37	1100	350	0.05	3	18.64	0.42	34.6
	38	1700	450	0.09	4	16.07	0.33	45.5
	39	1900	550	0.05	4	12.95	0.53	41.2

3 RESULTS AND DISCUSSIONS

3.1 ANFIS Models for Burnishing Responses

The experimental data of the internal roller burnishing operation are presented in Table 2. The experimental outcome from 1 to 26 are employed to develop ANFIS models, while the data from 27 to 39 are applied in order to evaluate the precision of the ANFIS correlations.

The 2-2-2-2 structure of the ANFIS model is applied to present the relationship between burnishing parameters and the energy consumed. The 3-3-3-3 structures of the ANFIS model are used to render the relationships between burnishing parameters and the surface roughness and Rockwell hardness. The membership function labelled *gaussmf* can bring minimal errors.

The comparisons between the predicted and experimental values of the E_{be}, R_a, and *RH* models are presented in Table 3. The small errors revealed that the ANFIS models can produce acceptable accuracy.

3.2 ANOVA Results for the Burnishing Responses

The ANOVA results for the E_{be}, R_a, and *RH* are shown in Tables 4, 5, and 6, respectively. The R^2 values of the E_{be}, R_a, and *RH* are 0.9883, 0.9874, and 0.9885, indicating the adequacy of the proposed models.

For the E_{be} model, the meaningful terms are the single factors (*S*, *f*, *D*, and *N*), interactive factors (*Sf*, *SD*, *fD*, and *DN*), and the quadratic factor (f^2). The contributions of the *S*, *f*, *D*, and *N* are 5.61 %, 50.44 %, 5.20 %, and 1.56 %. The contribution of the f^2 is 25.49 %. The contributions of the *Sf*, *SD*, *fD*, and *DN* are 3.11 %, 1.57 %, 3.26 %, and 1.43 %, respectively.

For the R_a model, the meaningful terms are the single factors (*S*, *f*, *D*, and *N*), interactive factors (*SN*), and quadratic factors (S^2, f^2, and N^2). The contributions of the *S*, *f*, *D*, and *N* are 10.88 %, 21.59 %, 14.61 %, and 10.07 %. The contributions of the S^2, f^2, and N^2 are 21.59 %, 8.60 %, and 3.65 %, respectively. The contribution of the *SN* is 8.77 %.

For the *RH* model, the meaningful terms are the single factors (*S*, *f*, *D*, and *N*) and quadratic factors (S^2, f^2, D^2, and N^2). The contributions of the *S*, *f*, *D*, and *N* are 19.98 %, 18.78 %, 16.49 %, and 14.70 %. The contributions of the S^2, f^2, D^2, and N^2 are 11.77 %, 7.31 %, 9.20 %, and 1.09 %, respectively.

3.3 Parametric Influences

Fig. 6a presents the impacts of the spindle speed and feed rate on the energy consumed. An increment in the feed rate has a significant contribution to a decrement in the burnishing time. The higher the feed rate is, the faster the burnishing will be. Therefore, a higher feed rate causes a reduction in energy consumption. At a higher spindle speed, the momentum of the spindle system increases to satisfy a targeted setting, which causes increased energy consumption. Moreover, an increased spindle speed causes a higher power used of the spindle system, which increases the total power used in the machine tool. The similar influences of the feed rate and spindle speed on the energy consumption for the flat burnishing process were presented in the works of [24] and [25].

Fig. 6b presents the influences of the burnishing depth and number of rollers on the energy consumed.

Table 3. *Comparative errors for the burnishing responses*

No.	E_{be} [kJ]			R_a [μm]			*RH* [HRC]		
27	Exp.	ANFIS	Err. [%]	Exp.	ANFIS	Err. [%]	Exp.	ANFIS	Err. [%]
28	30.58	30.14	1.44	0.34	0.33	2.94	30.4	30.8	1.30
29	22.47	22.78	1.38	0.37	0.38	2.63	35.2	34.7	1.42
30	17.72	17.56	0.90	0.38	0.36	5.26	42.9	42.1	1.86
31	14.15	14.47	2.26	0.49	0.48	2.04	43.5	42.9	1.38
32	14.64	14.42	1.50	0.37	0.36	2.70	45.6	45.2	0.88
33	13.22	13.44	1.64	0.52	0.53	1.89	44.2	42.8	3.17
34	13.39	13.63	1.79	0.46	0.45	2.17	43.9	44.5	1.35
35	14.64	14.49	1.02	0.41	0.43	4.65	40.7	41.5	1.93
36	13.25	13.48	1.74	0.39	0.38	2.56	45.4	45.9	1.10
37	13.84	13.62	1.59	0.52	0.51	1.92	42.9	42.4	1.17
38	18.64	18.35	1.56	0.42	0.41	2.38	34.6	34.1	1.45
39	16.07	16.33	1.62	0.33	0.32	3.03	45.5	44.9	1.32

Exp.: Experimental value; Err.: Error

Table 4. *ANOVA results for the E_{be} model*

So.	*SS*	*MS*	*F* Value	*P* value
Mod.	1479.343	105.667	66.370	< 0.0001
S	80.751	80.751	50.720	< 0.0001
f	726.022	726.022	456.015	< 0.0001
D	74.796	74.796	46.979	< 0.0001
N	22.490	22.490	14.126	0.0013
Sf	44.765	44.765	28.117	0.0004
SD	22.654	22.654	14.229	0.0276
fD	46.924	46.924	29.473	0.0002
DN	20.583	20.583	12.928	0.0392
f^2	366.955	366.955	230.485	< 0.0001
Res.	17.513	1.592	904.040	
Cor.	1496.857			
Mod.: Model; So.: Source; Res.: Residual; Cor.: Core total				

Table 5. *ANOVA results for the R_a model*

So.	*SS*	*MS*	*F* Value	*P* value
Mod.	0.305	0.022	61.332	< 0.0001
S	0.032	0.032	90.771	< 0.0001
f	0.064	0.064	180.181	< 0.0001
D	0.043	0.043	121.923	0.0001
N	0.030	0.030	84.036	< 0.0001
SN	0.026	0.026	73.187	0.0225
S^2	0.064	0.064	180.181	< 0.0001
f^2	0.025	0.025	71.769	0.0010
N^2	0.011	0.011	30.460	0.0385
Res.	0.004	0.000	834.512	
Cor.	0.309			

Table 6. *ANOVA results for the RH model*

So.	SS	MS	F Value	P value
Mod.	318.318	22.737	67.460	< 0.0001
S	72.521	72.521	215.166	< 0.0001
f	68.163	68.163	202.238	< 0.0001
D	59.853	59.853	177.582	< 0.0001
N	53.341	53.341	158.260	< 0.0001
S^2	42.727	42.727	126.770	< 0.0001
f^2	26.550	26.550	78.774	< 0.0001
D^2	33.401	33.401	99.100	< 0.0001
N^2	3.973	3.973	11.787	0.0056
Res.	3.708	0.337	1076.947	
Cor.	322.025			

An increased burnishing depth leads to a higher machining pressure, which causes a greater resistance on the machined surface; hence, higher energy consumed is required to overcome resistance. Similarly, a higher number of rollers causes an increased burnishing pressure. Therefore, more energy is required to burnish the material. The impacts of the burnishing depth and number of rollers on the energy used for the flat burnishing process were similarly described in the works of **[24]** and **[25]**.

Fig. 7a presents the influences of the spindle speed and feed rate on the surface roughness. A higher temperature in the machining area is obtained with an increased spindle speed, which causes a reduction in the workpiece hardness. Therefore, the material is easily burnished, and the roughness is reduced. Unfortunately, when the speed increases from 1500 rpm to 2000 rpm, the work-hardening behaviour is appeared, which causes a higher roughness. A higher feed rate causes a higher distance between two consecutive paths; hence, higher roughness is produced. The similar impacts of the feed rate and spindle speed on the surface roughness can be found for the external burnishings **[1]**, **[5]**, **[6]**, and **[9]**, flat burnishings **[2]**, **[24]**, and **[25]**, and the internal burnishings **[10]**, and **[17]**.

Fig. 7b presents the influences of the burnishing depth and number of rollers on the surface roughness. Higher burnishing depth causes a larger degree of plastic deformation; hence, low roughness is obtained. A reduction in the roughness with an increased burnishing depth was also found in the published investigations **[5]**, **[6]**, **[10]**, **[17]**, **[24]**, and **[25]**. A higher number of rollers leads to an increased frequency of engagement; hence, a higher degree of plastic deformation is obtained. More material is burnished, which causes a reduction in the roughness. A similar influence of the number of rollers on the surface roughness was presented in the works of **[6]**, **[10]**, and **[25]**.

Fig. 8a presents the impacts of the spindle speed and feed rate on the Rockwell hardness. A higher feed rate causes an increased burnishing pressure on the machined surface, which increases the degree of the plastic deformation; hence, the Rockwell hardness is improved. A higher spindle speed results in an increased temperature in the burnishing region, which causes an improvement in the larger plastic deformation. More material is then compressed and burnished; hence, the Rockwell hardness is enhanced. A further feed rate and/or speed may cause excessive burnishing temperature, and the residual stress can be relieved; hence, the Rockwell hardness value is decreased. Similar impacts of the spindle speed and feed rate on the machined hardness were presented in the works of **[17]**, **[18]**, **[24]**, **[25]**, and **[26]**.

Fig. 8b presents the impacts of the burnishing depth and number of rollers on the Rockwell hardness. An increased burnishing depth results in higher machining pressure, which causes a higher degree

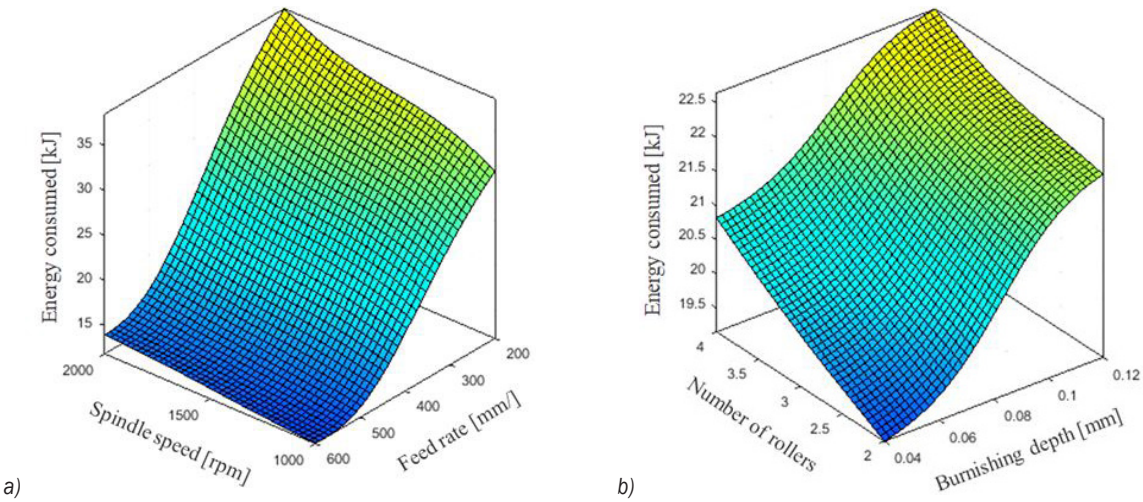

Fig. 6. *The influences of the burnishing parameters on the E_b: a) E_b versus S and f; b) E_b versus D and N*

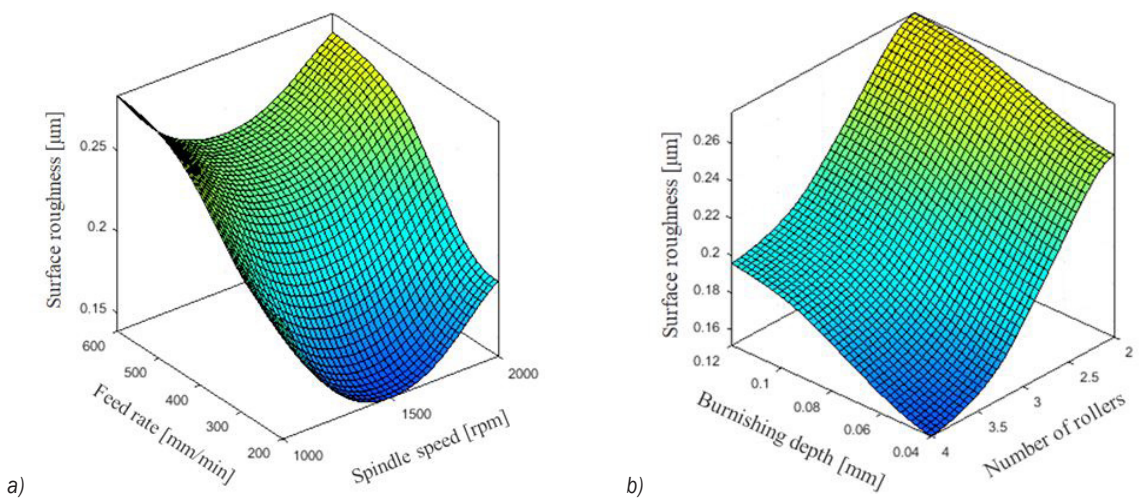

Fig. 7. *The influences of the burnishing parameters on the R_a: a) R_a versus S and f; b) R_a versus D and N*

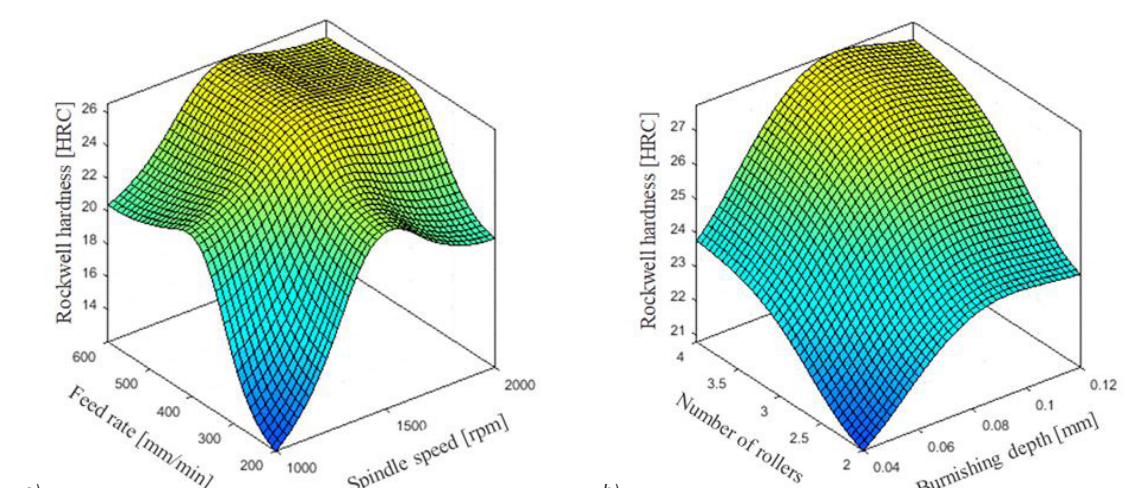

Fig. 8. *The influences of the burnishing parameters on the RH: a) RH versus S and f; b) RH versus D and N*

of work-hardening; hence, the Rockwell hardness is enhanced. However, a further burnishing depth leads to higher burnishing temperature and the residual stress can be relieved; hence, the Rockwell hardness is decreased. As the number of rollers increases, more material is compressed and burnished. A higher degree of plastic deformation is generated; hence, higher Rockwell hardness is obtained. An increased hardness with higher burnishing depth and the number of rollers can be found in the works of [17], [18], [24], [25], and [26].

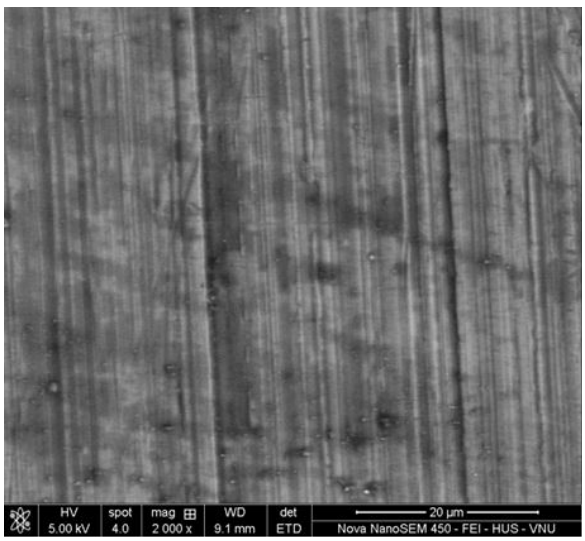

Fig. 9. *Surface morphology after burnishing process*

The surface morphology after the burnishing operation is presented in Fig. 9 with the aid of a Nano Nova 450″scanning electron microscope. It can be stated that a smooth surface can be achieved using the burnishing process. The pre-machined defects, such as grooves, cracks, and waviness, were filled.

3.4 Optimization Outcomes Generated by NOPSO

The single optimization is executed to find the best outcome for each response, as shown in Table 7.

The Pareto graphs produced by NSPSO are shown in Fig. 10. The global relation between the energy consumption and average roughness is depicted in Fig. 10a, while the trade-off analysis between the energy consumption and Rockwell hardness is presented in Fig. 10b.

It can be stated that machining performances have contradictory trends. The minimization of the average roughness may lead to increased energy consumed and decreased Rockwell hardness. Three typical solutions, including points 1, 2, and 3, are chosen to evaluate the burnishing performances (Table 8).

For the first point, the average roughness increases, while the energy consumed and Rockwell hardness decreases; hence, this solution does not satisfy the optimization requirement. For the second point, the energy consumed increases, while the average roughness and Rockwell hardness decrease; hence, this point cannot consider as a proper solution. For the third solution, the energy consumed and average roughness simultaneously are decreased, while the Rockwell hardness increases, as compared to the initial values. Consequently, the third point can be selected as an appropriate solution to enhance burnishing performances.

Based on the optimization requirement, the third point is selected as the optimal point. As a result, the optimum values of the spindle speed, feed rate, burnishing depth, and the number of rollers are 1513 rpm, 490 mm/min, 0.11 mm, and 4, respectively. The reductions in E_{be} and R_a are 16.3 % and 24.3 %,

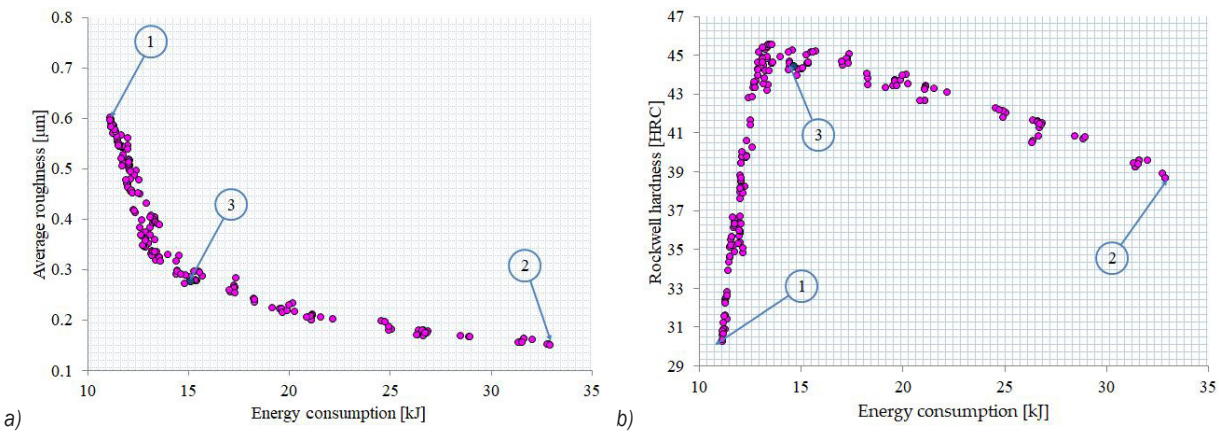

a) b)

Fig. 10. *Pareto graphs: a) E_b versus R_a; b) E_b versus RH*

Table 7. *Optimization results for each response*

Scenarios	Optimization parameters				Responses		
	S [rpm]	f [mm/min]	D [mm]	N	E_{be} [kJ]	R_a [μm]	RH [HRC]
For minimizing Eb	1000	600	0.04	2	11.09		
For minimizing Ra	1484	200	0.12	4		0.16	
For maximizing RH	1545	480	0.10	4			45.6

Table 8. *Optimization results for the burnishing responses using ANFIS-NOPSO*

Method	Optimization parameters				Responses		
	S [rpm]	f [mm/min]	D [mm]	N	E_{be} [kJ]	R_a [μm]	RH [HRC]
Initial values	1500	400	0.08	3	17.47	0.37	42.7
Point 1	1024	573	0.04	2	11.16	0.60	29.5
Point 2	1470	224	0.12	4	32.23	0.17	39.1
Point 3	1513	490	0.11	4	14.63	0.28	44.4
Improvement [%]					-16.3	-24.3	4.0

respectively, while the *RH* is enhanced by 4.0 %, as compared to the initial values.

3.5 Optimization Outcomes Generated by DA

The mathematical models of the E_{be}, R_a, and *RH* are expressed using Eqs. (10) to (12), respectively.

$$E_{be} = 44.70623 + 0.00374S - 0.13858f + 63.7D + 1.47729N - 0.000006Sf + 0.01614SD - 0.08356fD - 7.35DN + 0.00013f^2, \quad (10)$$

$$R_a = 0.78458 - 0.00088S - 0.00013f - 1.75D + 0.19583N - 0.00009SN + 0.0000004S^2 + 0.000001f^2 - 0.01875N^2, \quad (11)$$

$$RH = -33.99167 + 0.04038S + 0.05858f + 316.39167D + 6.68633N - 0.000012S^2 - 0.000065f^2 - 1773.41146D^2 - 0.88208N^2 \quad (12)$$

Optimization outcomes are shown in Fig. 11. The optimum values of the spindle speed, feed rate, burnishing depth, and the number of rollers are 1427 rpm, 468 mm/min, 0.09 mm, and 4, respectively. The reductions in the E_{be} and R_a are 14.4 % and 2.7 %, respectively, while the *RH* is enhanced by 2.8 %, as compared to the initial values.

3.6 Evaluation of Optimization Outcomes

As given in Table 8, the ANFIS-NOPSO provides the improvements in the E_{be}, R_a, and *RH* are 16.3 %, 24.3 %, and 4.0 %, respectively. As shown in Table 9, the reductions in the E_{be} and R_a are 14.4 % and 2.7 %, respectively, while the *RH* is enhanced by 2.8 % at the optimal solution produced by the RSM-DA. It can be stated that the ANFIS-NOPSO is more efficient than the RSM-DA regarding the optimization issues for the burnishing operation.

3.7 Scientific and Industrial Contributions

The optimal values of process parameters and burnishing responses are only determined using the optimization technique. The ANFIS-NOPSO is more efficient than the RSM-DA in resolving the complex optimizing issue.

The proposed optimization approach using ANFIS and NOPSO can be applied to solve optimization problems for different burnishing operations with different materials.

The scientific findings can be effectively applied in future works for optimization of the burnishing operation or development of the expert system in terms of the burnishing process.

The ANFIS models of the energy consumed, surface roughness, and Rockwell hardness have been developed in terms of machining factors. These models have an industrial interest, which can be applied to forecast the burnishing performances for hardened 40X steel.

The optimal outcomes generated by the ANFIS-NOPSO can be employed to improve the technical parameters for the internal burnishing operation of hardened 40X steel.

Table 9. *Optimization results for the burnishing responses using RSM-DA*

Method	Optimization parameters				Responses		
	S [rpm]	f [mm/min]	D [mm]	N	E_{be} [kJ]	R_a [μm]	RH [HRC]
Initial values	1500	400	0.08	3	17.47	0.37	42.7
Optimal values	1427	468	0.09	4	14.96	0.36	43.9
Improvement [%]					-14.4	-2.7	2.8

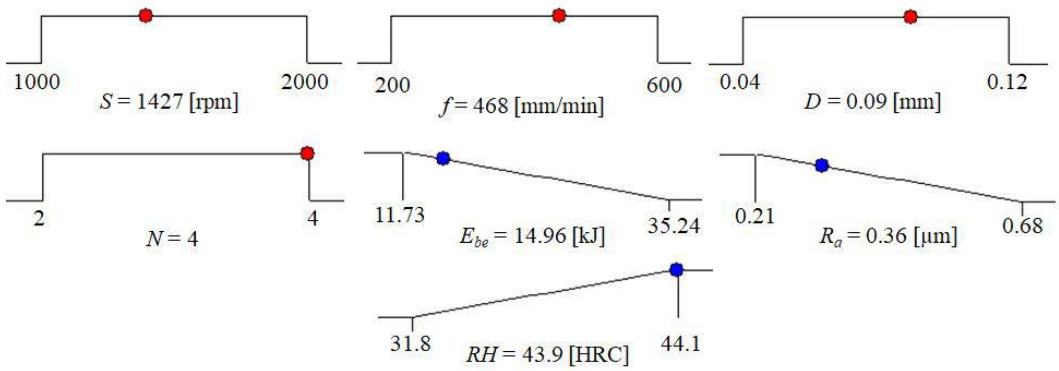

Fig. 11. *The optimal values generated by the DA*

Moreover, the parametric influences can help machine operators deeply understand the impacts of burnishing factors on the process responses.

4 CONCLUSIONS

In this investigation, an attempt has been made to optimize the machining conditions of the roller burnishing operation for reducing the energy consumed in the burnishing state, surface roughness, and Rockwell hardness. The inputs considered are the spindle speed, burnishing feed, burnishing depth, and the number of rollers. The ANFIS method was employed to propose the predictive models of technical outcomes. The NSPSO was utilized to find optimal outcomes. The conclusion can be presented as bellows:

1. The minimum values of the spindle speed, burnishing depth, and the number of rollers can be applied to save the energy consumed, while the highest feed rate is recommended to apply. Higher values of the burnishing depth and number of rollers can be employed to decrease the roughness, while a minimum feed rate leads to a reduction in the roughness. The middle level of the spindle speed is used to obtain a smooth surface. Higher levels of process parameters are recommended to enhance the Rockwell hardness.
2. The ANFIS models of the energy consumption in the burnishing time, surface roughness, and Rockwell hardness can be applied to predict the response values with high accuracy. These developed models are effectively employed to save experimental costs and human efforts.
3. The Pareto fronts can significantly help machine operators to determine proper parameters for decreasing energy consumed as well as average roughness and enhancing Rockwell hardness. The appropriate selection of process parameters can decrease machining costs, time, operator skills, and efforts.
4. As shown in the optimal setting generated by NSPSO, the optimal parameters of the S, f, D, and N are 1513 rpm, 490 mm/min, 0.11 mm, and 4, respectively. The E_{be}, and R_a are decreased by 16.3 % and 24.3 %, while the RH is enhanced by 4.0 %, respectively in comparison with the initial values.
5. In the current investigation, the machining factors are optimized to decrease the energy consumption as well as average roughness and to improve the Rockwell hardness. Practically, the impacts of burnishing parameters on the residual stress, the depth of the affected layer, and machining costs have been not presented. Therefore, a holistic optimization considering

more burnishing performances will be addressed in future investigation.

5 ACKNOWLEDGEMENTS

This research is funded by Vietnam National Foundation for Science and Technology Development (NAFOSTED) under grant number 107.04-2020.02.

6 NOMENCLATURE

D Burnishing depth, [mm]
E_{be} Energy consumption in the burnishing time, [kJ]
f Feed rate, [mm/min]
MS Mean square
N Number of rollers
RH Rockwell hardness, [HRC]
S Spindle speed, [rpm]
SS Sum of squares
R_a Surface roughness, [μm]

7 REFERENCES

[1] El-Taweel, T.A., El-Axir, M.H. (2009). Analysis and optimization of the ball burnishing process through the Taguchi technique. *The International Journal of Advanced Manufacturing Technology*, vol. 41, p. 301-310, **DOI:10.1007/s00170-008-1485-6**.

[2] Stalin John, M.R., Vinayagam, B.K. (2011). Optimization of ball burnishing process on tool steel (T215Cr12) in CNC machining centre using response surface methodology. *Arabian Journal for Science and Engineering*, vol. 36, p. 1407-1422, **DOI:10.1007/s13369-011-0126-9**.

[3] Babu, P.R., Ankamma, K., Prasad, T.S., Raju, A.V.S., Eswara Prasad, N. (2012). Optimization of burnishing parameters and determination of select surface characteristics in engineering materials. *Sadhana*, vol. 37, p. 503-520, **DOI:10.1007/s12046-012-0092-2**.

[4] Tadic, B., Todorovic, P.M., Luzanin, O., Miljanic, D., Jeremic, B.M., Bogdanovic, B., Vukelic, D., (2013). Using specially designed high-stiffness burnishing tool to achieve high-quality surface finish. *International Journal of Advanced Manufacturing Technology*, vol. 67, p. 601-611, **DOI:10.1007/s00170-012-4508-2**.

[5] Cobanoglu, T., Ozturk, S. (2014). Effect of burnishing parameters on the surface quality and hardness. *Proceedings of the Institution of Mechanical Engineers, Part B: Journal of Engineering Manufacture*, vol. 229, no. 2, p. 286-294, **DOI:10.1177/0954405414527962**.

[6] Stalin John, M.R., Vinayagam, B.K. (2014). Optimization of nonlinear characteristics of ball burnishing process using Sugeno fuzzy neural system. *Journal of the Brazilian Society of Mechanical Sciences and Engineering*, vol. 36, p. 101-109, **DOI:10.1007/s40430-013-0060-8**.

[7] Revankar, G.D., Shetty, R., Rao, S.S., Gaitonde, V.N. (2014). Analysis of surface roughness and hardness in ball burnishing of titanium alloy. *Measurement*, vol. 58, p. 256-268, **DOI:10.1016/j.measurement.2014.08.043**.

[8] Amdouni, H., Bouzaiene, H., Montagne, A., Van Gorp, A., Coorevits, T., Nasri, M., Iost, A. (2017). Experimental study of a six new ball-burnishing strategies effects on the Al-alloy flat surfaces integrity enhancement. *International Journal of Advanced Manufacturing Technology*, vol. 90, p. 2271-2282, **DOI:10.1007/s00170-016-9529-9**.

[9] Stalin John, M.R., Banerjee, N., Shrivastava, K., Vinayagam, B.K., (2017). Optimization of roller burnishing process on EN-9 grade alloy steel using response surface methodology. *Journal of the Brazilian Society of Mechanical Sciences and Engineering*, vol. 39, p. 3089-3101, **DOI:10.1007/s40430-016-0674-8**.

[10] Stalin John, M.R., Balaji, B., Vinayagam, B.K., (2017). Optimisation of internal roller burnishing process in CNC machining center using response surface methodology. *Journal of the Brazilian Society of Mechanical Sciences and Engineering*, vol. 39, p. 4045-4057, **DOI:10.1007/s40430-017-0871-0**.

[11] Świrad, S., Wydrzynski, D., Nieslony, P., Krolczyk, G.M. (2019). Influence of hydrostatic burnishing strategy on the surface topography of martensitic steel. *Measurement*, vol. 138, p. 590-601, **DOI:10.1016/j.measurement.2019.02.081**.

[12] Huuki, J., Laakso, S.V.A. (2012). Integrity of surfaces finished with ultrasonic burnishing. *Proceedings of the Institution of Mechanical Engineers, Part B: Journal of Engineering Manufacture*, vol. 227, no. 1, p. 45-53, **DOI:10.1177/0954405412462805**.

[13] Teimouri, R., Amini, S., Bami, A.B. (2018). Evaluation of optimized surface properties and residual stress in ultrasonic assisted ball burnishing of AA6061-T6. *Measurement*, vol. 116, p. 129-139, **DOI:10.1016/j.measurement.2017.11.001**.

[14] Yang, S., Umbrello, D., Dillon, O.D.Jr., Puleo, D.A., Jawahir, I.S. (2015). Cryogenic cooling effect on surface and subsurface microstructural modifications in burnishing of Co–Cr–Mo biomaterial. *Journal of Materials Processing Technology*, vol. 217, p. 211-221, **DOI:10.1016/j.jmatprotec.2014.11.004**.

[15] Tang, J., Luo, H.Y., Zhang, Y.B. (2017). Enhancing the surface integrity and corrosion resistance of Ti-6Al-4V titanium alloy through cryogenic burnishing. *International Journal of Advanced Manufacturing Technology*, vol, 88, p. 2785-2793, **DOI:10.1007/s00170-016-9000-y**.

[16] Sachin, B., Narendranath, S., Chakradhar, D. (2019). Enhancement of surface integrity by cryogenic diamond burnishing toward the improved functional performance of the components. *Journal of the Brazilian Society of Mechanical Sciences and Engineering*, vol. 41, art. ID 396, **DOI:10.1007/s40430-019-1918-1**.

[17] Tajane, R.S., Pawar, P.J. (2020) Investigation into burnishing to minimize heat treatment in drill manufacturing. *Materials and Manufacturing Processes*, vol. 35, no. 7, p, 817-825, **DOI:10.1080/10426914.2020.1743848**.

[18] Maximov, J.T, Duncheva, G.V., Anchev, A.P., Dunchev, V.P. (2020). Smoothing, deep, or mixed diamond burnishing of low-alloy steel components – optimization procedures. *International Journal of Advanced Manufacturing Technology*, vol. 106,p. 1917-1929, **DOI:10.1007/s00170-019-04747-2**.

[19] Nguyen, T.-T., Mia, M., Dang, X.-P., Le, C.-H., Packianather, M.S. (2020). Green machining for the dry milling process of stainless steel 304. *Proceedings of the Institution of Mechanical Engineers, Part B: Journal of Engineering Manufacture*, vol. 234, no. 5, p. 881-899, **DOI:10.1177/0954405419888126**.

[20] Hegedüs, F., Bécsi, T., Aradi, S., Gáspár, P. (2019). Motion planning for highly automated road vehicles with a hybrid approach using nonlinear optimization and artificial neural networks. *Strojniški vestnik - Journal of Mechanical Engineering*, vol. 65, no. 3, p. 148-160, **DOI:10.5545/sv-jme.2018.5802**.

[21] Ghritlahre, H.K., Prasad, R.K. (2018). Exergetic performance prediction of a roughened solar air heater using artificial neural network. *Strojniški vestnik - Journal of Mechanical Engineering*, vol. 64, no.3, p. 194-206, **DOI:10.5545/sv-jme.2017.4575**.

[22] Wang, Y., Liu, Z., Cai, L., Cheng, Q., Dong, X. (2018). Optimization of oil pads on a hydrostatic turntable for supporting energy conservation based on particle swarm optimization. *Strojniški vestnik - Journal of Mechanical Engineering*, vol. 64, no. 2, p. 95-104, **DOI:10.5545/sv-jme.2017.4742**.

[23] Nguyen, T.-T., Vu, T.-C., Duong, Q.-D. (2020) Multi-responses optimization of finishing honing process for surface quality and production rate. *Journal of the Brazilian Society of Mechanical Sciences and Engineering*, vol. 42, art. ID 604, **DOI:10.1007/s40430-020-02690-y**.

[24] Nguyen, T.-T., Cao, L. H., Dang, X. P., Nguyen, T.-A., Trinh, Q. H. (2019). Multi-objective optimization of the flat burnishing process for energy efficiency and surface characteristics. Materials and Manufacturing Processes, vol. 34, 1888-1901, **DOI:10.1080/10426914.2019.1689266**.

[25] Nguyen, T.-T., Cao, L.-H., Nguyen, T.-A., Dang, X.-P. (2019). Multi-response optimization of the roller burnishing process in terms of energy consumption and product quality. *Journal of Cleaner Production*, vol. 245, **DOI:10.1016/j.jclepro.2019.119328**.

[26] Nguyen, T.T., Mia, M. (2020). Modeling and evaluation of energy efficiency of new hybrid turning-burnishing process in terms of surface properties. *Energies*, vol. 13, no. 18, art. ID 4929, **DOI:10.3390/en13184929**.

Strojniški vestnik - Journal of Mechanical Engineering 67(2021)4, 180-190
DOI:10.5545/sv-jme.2021.7124
Original Scientific Paper
Received for review: 2021-01-21
Received revised form: 2021-02-25
Accepted for publication: 2021-03-29

Design of a Throat-extended FDM Extruder for Multi-axis 3D Printing

Hao Liu[1*] – Zhoupeng Liu[1,*] – Siting Hao[2]

[1] Nanjing University of Aeronautics and Astronautics, College of Mechanical and Electrical Engineering, China
[2] Tianjin University, College of Mechanical Engineering, China

Multi-axis fused deposition modelling (FDM) 3D printing technology has been paid attention to by more and more people. However, existing FDM extruders are usually short and fat, which significantly restricts the popularization of multi-axis FDM 3D printing technology because one significant trend of additive manufacturing is the use of long and thin extruders to avoid collisions between extruders and workpieces in the printing process. This paper presents the design of a throat-extended FDM extruder to print complex-shaped workpieces with details. The main contributions in this paper include: (i) presenting a novel extruder structure including an extended-throat, a smaller heater block, and a cooling mini-fan; (ii) designing an optimized heater block using the shapes of its components and the milling tool as constraints to make its volume as little small as possible; (iii) Construct experimental and simulation methods to examine the temperature distribution of the throat to optimize the shapes of the heat dams of nozzle throats and the wind speed of the heat-dissipation fan. Based on the throat-extended FDM extruder, a five-axis FDM 3D printer has been developed, and various complex-shaped workpieces have been printed without any support.
Keywords: 3D printing, FDM, extruder, design, multi-axis, throat

Highlights

- *Construct a novel FDM direct extruder structure, including a smaller heater block, the extended throat, and a mini cooling fan.*
- *Present experimental and simulation methods to measure the temperature distribution along the throat lengthwise direction referring to the heat-insulating tape and cooling-wind.*
- *Design an optimized heater block using shapes of its components and the milling tool as constraints to make its volume as small as possible.*
- *Optimize the heat dam number for the extended-throat shape using the orthogonal experiment method to prevent the heat conduction along the throat upward from the hot end as much as possible.*
- *Present an optimal wind speed for the mini cooling fan to make the thermal equilibrium state appear to maintain the working temperature of the heater block.*

0 INTRODUCTION

Along with increasing applications of 3D printing, researchers are increasingly dissatisfied with the 2.5-axis 3D printing because these supports waste significant amounts of printing time and materials **[1]**. Consequently, support-free multi-axis 3D printing has been popular in recent years **[2]** to **[4]**. Furthermore, in the field of surface-cladding, the multi-axis 3D printer has been regarded as the most appropriate type of equipment **[5]** and **[6]**. Among all 3D printing methods, fused deposition modelling (FDM) has been the most well-known method because of its simplicity and cheapness **[7]** and **[8]**. Therefore, this paper focuses on the FDM 3D printing that can be more easily extended to a multi-axis process from the 2.5-axis process by adapting the kinematics, extruders, and path planning **[1]** to **[3]**.

Among these adaptations, the improvement of extruders is very important because the conventional printing head is short and fat due to the hot end with a radiator and heater block, as shown in Fig. 1a. For many workpieces with complex structures **[9]** and **[10]**, when these details are going to be printed one by one so that printing paths are optimized, and the printing quality is improved, a conventional printing head is not suitable because the short-fat print head always collides printed workpiece details (see Fig. 1a). To avoid such collisions, an intuitive design concept is to extend the nozzle throat and to use a smaller hot end, as shown in Fig. 1b. Furthermore, the external radiator is eliminated.

There are two types of extruders: pellet extruders **[11]** to **[14]** and filament extruders **[15]** to **[18]**. For the first one, Pollák et al. **[11]** presented a pellet extruder that can use recycled materials as the printing material, except for plastic and composites. Whyman et al. **[12]** aimed at the special need that the bio-polymer filament could not satisfy for some research fields and designed a pellet-based extrusion system for the 3D printing of bio-polymers. Goyanes et al. **[13]** developed a single-step process pellet extruder that directly extrudes powder materials for the fabrication of drug products. Netto et al. **[14]** researched a twin-screw extruder to allow in-process multi-material mixing and direct deposition of the product to construct

*Corr. Author's Address: Nanjing University of Aeronautics and Astronautics, 054 Department, No.29 Yudao Street, Nanjing, China, liuhao-01@nuaa.edu.cn, liuzhoupenga@nuaa.edu.cn

three-dimensional parts. Regarding the background, a throat-extended pellet extruder may be appropriate. However, compared with filament extruders, pellet extruders are usually more expensive and complex. They are frequently used in special fields, such as biopolymers [12], drugs [13], composite materials [11] and [14], and where additive manufacturing can create furniture, vehicle bodies, or building materials [19] and [20]. Consequently, filament extruders are more suitable for most users of conceptual designs.

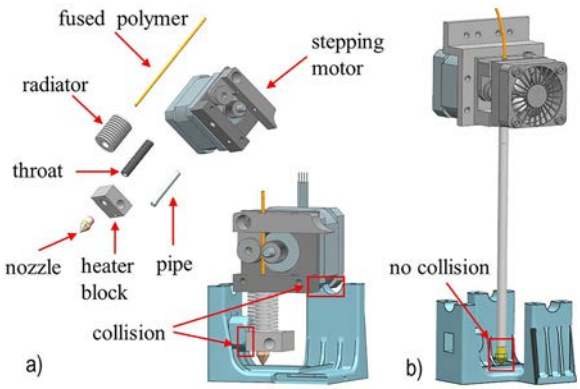

Fig. 1. *Comparison between the conventional printing head and the long-throat printing head; a) conventional printing head, and b) concept design of a multi-axis printing head*

The filament extruder includes a cool end and a hot end. The nozzle throat connects the two ends. The filament passes through the throat pipe. The cool end drives the filament into the hot end. It is usually composed of a numerical control motor, a toothed gear, and a bearing. The filament is placed between the toothed gear and the bearing. When the motor is activated, the gear rotates, and the filament is driven towards the hot end [15] and [16]. There are two types of filament extruders: direct extruders and Bowden extruders. The only difference between the two is that the throat of the direct extruder is a short and fat metal tube with a radiator while the throat of the Bowden extruder is a long flexible plastic tube [16] and [17]. Generally, there are two large disadvantages for the Bowden extruder [17]: (i) slower response time because of more friction in the Bowden tube to avoid stringing [21] to [23], fast retractions are required; (ii) a smaller range of materials, which means that some flexible filaments probably bind in Bowden tubes.

Consequently, researchers usually improve the direct extruder according to their needs. For example, Abilgaziyev et al. [16] presented a print head with several nozzles so that different materials can be printed in different regions of parts. Han et al. [18] developed a printing head with a nozzle and two throats so that two materials with different colours can be mixed. Go and Hart [24] found that the volumetric build rate of fused filament fabrication (FFF) could be limited by some conventional designs. They presented a Fast FFF system to overcome these conventional limits by extending the heater block towards the cool end and adding a laser auxiliary heater for the filament before coming into the heater block. Löffler and Koch [25] described a concept of a rotatable print head with a slot-shaped nozzle opening. Their design allowed the free adjustment of the path-line width and the layer heights. Though there are many works on innovative designs of direct extruders, there isn't an improved direct extruder to avoid collisions in multi-axis the 3D printing process even if Dai et al. [4] and Huang et al. [26] developed robot arms with direct extruders. To design a throat-extended slim direct extruder, there are three challenges: (i) shape optimization of a smaller heater block; (ii) shape optimization of nozzle throat without a radiator; (iii) appropriate temperature maintaining of the heater.

The heater is a key part of the extruder [15] and [27]. There are three problems to be improved: the resistor power, its appropriate temperature, and its geometrical shape. To select the power of the resistor, there are two estimation models of the heat flux: constant heat flux and constant wall temperature [27] to [29]. There are also some pieces of literature [30] to [32] to discuss appropriate temperatures to obtain the optimal printing quality. Because the appropriate temperature for a filament is constant and because aluminium (the heater block material) is a typical heat conductor, these conclusions in existing literature can be used in this paper. Jerez-Mesa's finite element analysis [33] also proved that the heater block has a constant temperature. However, distinct from existing designs, in our design, the heat-insulating tape method is used for our heater block because the ratio between the superficial area and the volume of the heater block is larger than the conventional heater block. The shape of the heater block in this paper is also optimized to reduce its *XY*-projection-area and quality.

Geometric accuracy is also an important topic about the FDM extruder. For example, Budzik et al. [37] verified the geometrical accuracy of 3D printing models of the lateral-mandibular condyle using several different printing methods, such as FDM, PolyJet, and selective laser sintering. The selective laser sintering had a standard deviation of 0.06 mm while FDM and PolyJet had a similar standard deviation of 0.07 mm. El-Katatny et al. [38] gave the standard deviation 0.24 % and 0.22 %, respectively, for FDM skull models and mandible models. Polak et al. [39] presented

FDM processing settings to the highest geometric accuracy. Boschetto and Bottini [40] developed an empirical formula to predict the geometric errors for FDM parts. In this paper, geometric accuracy comparisons between our extruder and the usual FDM extruder on the market are implemented to verify the *usability* of our extruder.

Aiming at the filament FDM extruder without collisions between the extruder and the workpiece in the printing process, the contributions of this paper include:

(1) Present a filament FDM extruder for the 3D printing of complex-structure workpieces. The extruder is composed of a heater block, an extended nozzle throat, and wind-speed-adjustable cooling equipment;
(2) Optimizing the shape of the heater block using other components and the milling tool as constraints to make its *XY*-projection-area as small as possible so that there are as few collisions as possible between the extruder and the workpiece in the printing process;
(3) Constructing FEA and experimental methods for the temperature distribution analysis of the throat to optimize the shapes of heat dams of nozzle throats and the wind speed of the heat-dissipation fan to prevent the heat conduction along the throat upward from the hot end.

In the rest of this paper, Section 1 provides the theoretical and experimental methods used to design the extruder. Section 2 presents details of the experimental set-up and the methods used to obtain the data. Section 3 shows the experimental data using figures and tables. Section 4 concludes our researches in this paper.

1 DESIGN AND METHODS

This section firstly gives a general design concept of the extruder. Then, a heater block shape optimization approach is presented based on the shapes and sizes of other components. The third subsection constructs a temperature field analysis FEA model for the heater block and the throat when the insulating tape and the cooling-fan are used. The fourth subsection discusses optimization methods for the heater block, the throat, and the cooling-wind speed.

1.1 General Design Concept

In this paper, the throat-extended extruder is installed in a five-axis (X, Y, Z, A, and C) printer. The printing head has three degree of freedom (DOF) including X, Y, and Z. The workpiece is placed on the AC rotary table, as shown in Fig. 2.

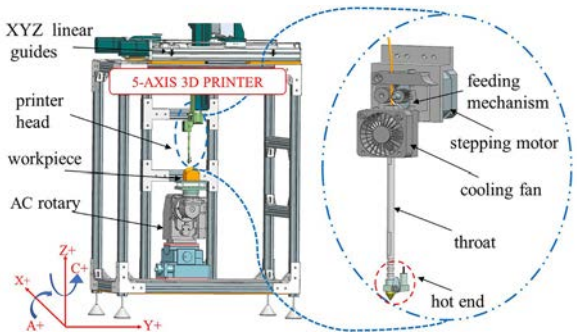

Fig. 2. *Concept design of our 5-axis FDM 3D printer with the throat-extended extruder*

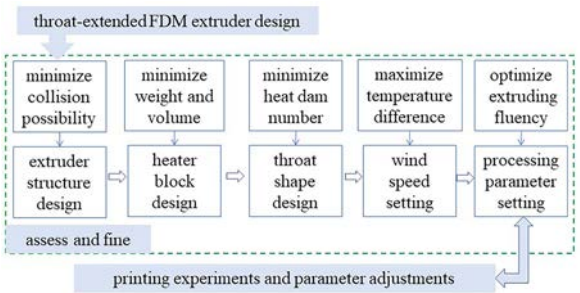

Fig. 3. *Design process proposed for the throat-extended FDM extruder*

To fabricate workpieces with fine details, the radiator has to be discarded, and the size of the heater block has to be reduced. Consequently, the design should include: (i) heater block shape optimization based on built-up members (nozzle, resistor, throat, thermistor), processing ability of machine tools; (ii) size and number optimization of dams of the nozzle throat based on the temperature field of the nozzle throat to the heat conduction along the throat upward from the hot end; (iii) wind speed adjustment to maintain the constant working temperature for the throat. Fig. 3 shows a flow diagram to design the FDM extruder.

1.2 Throat Design

A long and thin throat probably makes the filament form jam (see Fig. 4b) because of the extrusion force and the high throat temperature. The traditional extruder is equipped with radiators on the throat to radiate the throat heat, but they make the throat to thick. Consequently, throat heat dams and a cooling fan are used in the throat-extended extruder (see Fig. 4a).

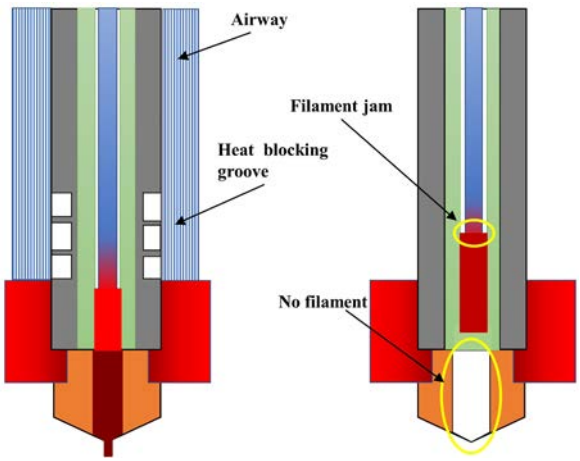

Fig. 4. *Schematic diagram of extruder jam; a) regularly work, b) jammed*

In our design, the throat is made of stainless steel. The wall thickness is 2 mm. There are several heat dams at the low region of the throat, shown in Fig. 4a. Widths for dams and grooves are 3 mm to 5 mm. The groove depth is 0.5 mm to 1.5 mm. The nozzle is made of copper. According to Fig. 2, the cooling wind blows from top to bottom. The velocity is 1 m/s to 5 m/s.

1.3 Heater Block Shape Design

As shown in Fig. 5a, the parts of a heater block include a nozzle, a resistor, a throat, and a thermistor. For the conventional heater block (see Fig. 5a), the main part is a quadrilateral aluminium block in which there are two large bolt holes for the nozzle and the throat, and a hole for the resistor that is inserted into the heater block. Because of the inserted resistor, the heater block is usually large. Existing aluminium blocks usually have the size 20 mm × 20 mm × 10 mm. Note that the resistor is horizontally inserted, which makes its electric wire occupy spaces in the length direction. The heater block occupies space up to 30 mm × 30 mm × 10 mm or more. Consequently, it is necessary to optimize the heater block shape. According to the 3D printing process, the design of the heater block of the throat-extended extrusion should satisfy the following principles:

(i) Aluminium block sizes in *x*-direction and *y*-direction should be as little as possible so that more workpieces details can be printed;

(ii) Temperature of the throat should be as low as possible so that the heat of heater block cannot be conducted to the cold end;

(iii) The quality of the heater block should be as little as possible because the large quality means that the large inertia force that makes the connection between the throat and the cold end loose.

Firstly, refer to the principle (iii). The quality of the heater block in the schematic in Fig. 5c, must be larger than the quality of the heater block in the scheme of Fig. 5b, which means that the schematic in Fig. 6c is against the criterion (iii). Consequently, we use the schematic in Fig. 5b instead of the one in Fig. 5c. Now we have to acquire some parameter values for the design in Fig. 5b to make the quality of the heater block as little as possible. These parameters are illuminated in Fig. 6. According to the ISO standard [34], because the depth of the screw thread groove of the throat is 0.541 mm, the wall thickness *w* (in Fig. 6) is usually larger than 1 mm. Because the diameter of the locking mini bolt is 3 mm, the thickness *h* (in Fig. 6) is usually larger than 3.6 mm [35].

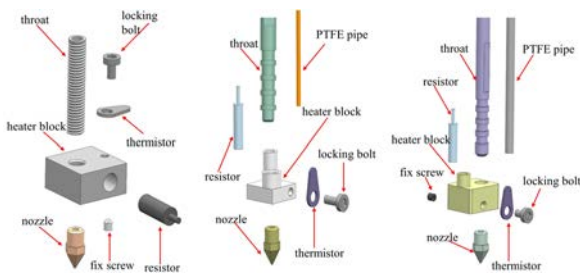

Fig. 5. *Comparison of a conventional heater block and our innovative heater block; a) conventional heater block, b) optimal heater block, c) inserted bolt hole*

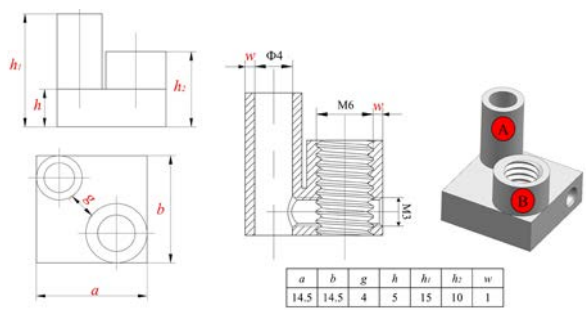

a	b	g	h	h_1	h_2	w
14.5	14.5	4	5	15	10	1

Fig. 6. *Size specification for the heater block [unit: mm]*

Criterion (ii) means that cylinder A and cylinder B (see Fig. 6) must be separated. By criterion (i), the less the gap size *g* is, the better the block is. However, the gap size *g* is determined by the diameter of the milling tool. Referring to existing milling tools, the minimum diameter of the milling tool is 3 mm. Consequently, we set the gap "*g*" as 4 mm so that the two cylinders can be milled and pasted with heat-insulating tape.

1.4 Principles and Methods of FEA

Since the cooling-wind is necessary to maintain a wanted thermal equilibrium state, the thermal numerical analysis problem is a heat transfer fluid-solid coupling problem that combines the computational fluid dynamics (CFD) computation of the environment flowing air and the temperature field FEA of the heater block. Principles of the fluid-solid coupling computation are shown in Fig. 7. The numerical analysis is implemented by Abaqus 6.14.

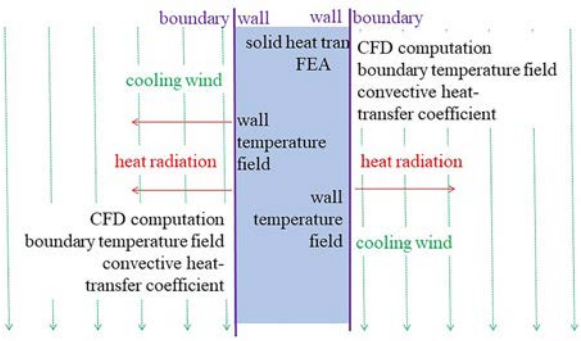

Fig. 7. *Illumination of the Fluid-Solid Interaction*

1.5 Orthogonal Experiment Statistical Methods

The orthogonal experiment is used to optimize the heat-dam shape and the cooling-wind speed. To analyse the orthogonal experiment data, two statistical methods (signal-to-noise ratio analysis (S/N) and analysis of variance (ANOVA)) are used. S/N is used to sort shape parameters of heat dams according to their importance. The statistical formula is used in Eq. (1), where η is S/N, p is the number of trials, and w is experimental data.

$$\eta = -10\log[\frac{1}{p}\sum_{i=1}^{p}(\frac{1}{w_i^2})]. \quad (1)$$

ANOVA is used to distinguish whether the difference in the experimental results is caused by the change of factor levels or by the experimental error, in which five statistical approaches are usually used: sum of squares (SS), mean square error (MS), degree of freedom (DOF), F-test statistics, and p-values. For the last one, the lower p-value (less than 0.05) means the significant influence of the parameter for the experimental result.

1.6 Temperature Field Analysis Model

As shown in Fig. 8, we select four temperature-monitoring points on the body composed of the throat and the heater block because we hope that the heater block has a constant temperature of 200 °C while the temperature declines as fast as possible along the throat. At the point near the cool end, the throat temperature should be close to the indoor temperature (20 °C).

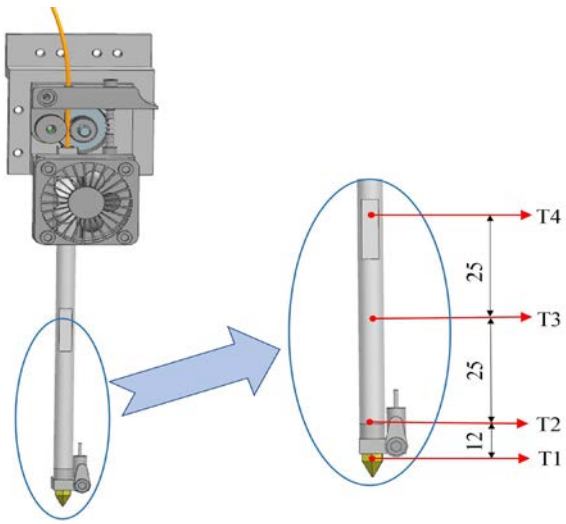

Fig. 8. *Thermal analysis model for the heater block and the throat; T1: heater block region, T2: throat region close to the hot end, T3: throat middle region, and T4: throat region close to the cool end*

2 EXPERIMENTAL DESCRIPTION

This section includes four subsections: extruder working environment and devices, thermal numerical analysis, discussions of experimental factors, and verification of FEA.

2.1 Working Environment and Devices

These experiments are performed at a room temperature of 20 °C. As shown in Fig. 9, the extruder is installed in the printer. We let the thermal resistor inserted in the heater block (see Fig. 5b) work while the extruder does not move but does extrude silks. There is a thermistor connected to a temperature controller. When the thermal equilibrium state appears, temperatures of these monitoring points are measured.

A temperature measurement system is shown in Fig. 10. The measurement range of the thermometer (Fig. 10, marked ①) is –200 °C to 1372 °C, and the accuracy is ±0.1 %. The speed range of the anemometer (see Fig. 10, marked ④) is 0 m/s to 30 m/s, with a basic error of ±1 %. The thermocouple

detector and the wire are fixed to install detectors at monitoring points.

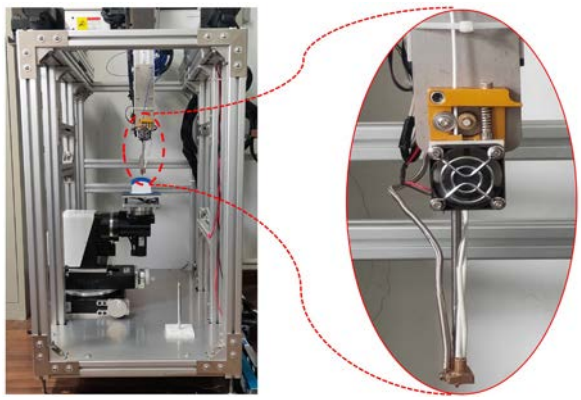

a) b)

Fig. 9. *Pictures of the 5-axis printer installed the novel extruder; a) overall appearance, and b) extruder*

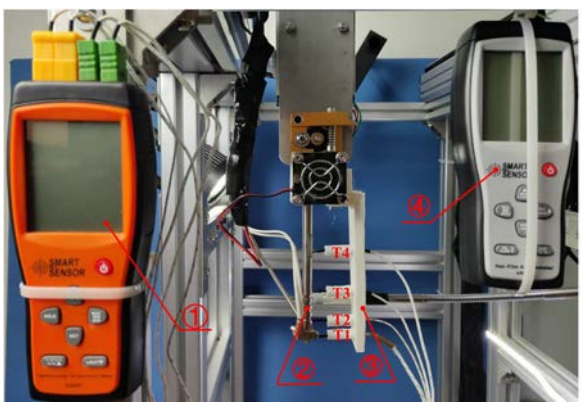

Fig. 10. *The experimental temperature measurement system; ① thermal conductor, ② extruder, ③ fixed support, and ④ mini-anemograph*

2.2 Thermal Numerical Analysis

The heater block is set as the heat source, and the boundary temperature is 200 °C, since only the thermal equilibrium is under consideration. The connection way between the components is "binding". The heat dissipation conditions are defined as the convective heat transfer between the surface of the throat and the outside air. Wind velocity conditions are assigned to the lower tuyere of the air guide hood. Since the wind velocity is not large, laminar flow is formed near the hot end. The convective heat transfer is obtained from the empirical formula in [36].

2.3 Experimental Factors and Levels

According to the analysis in subsection 2.1, a stainless-steel pipe is selected with a length of 140 mm, an outer diameter of 6 mm, an inner diameter of 4 mm as the throat pipe. The inside-liner is a Teflon tube with an outer diameter of 4 mm and an inner diameter of 1.9 mm. The filament is fed into the Teflon tube through the cold end and then arrives at the hot end. In the experiment, we select five factors that affect the temperature field distribution: wind velocity, the number of grooves, groove width, groove depth, and the dam width. Table 1 shows each level value of the factors, which is obtained based on experiences and preliminary experiments. We will select an optimal combination for these level values using an orthogonal experiment.

Table 1. *Factors and levels*

Levels	A Wind velocity [m/s]	B Groove number	C Dam width [mm]	D Groove width [mm]	E Dam depth [mm]
1	1	1	3	3	0.5
2	1.5	2	3.5	3.5	0.75
3	2	3	4	4	1.0
4	2.5	4	4.5	4.5	1.25
5	3	5	5	5	1.5

2.4 Verification of FEA

Because many samples are required for the optimizations of shapes and the parameters of the extruder, and real experiments always need more time and expense, we use simulation experiments instead of real experiments. To verify simulation results, this subsection measures the temperature of T_1 to T_4 in Fig. 8 under different heat dissipation conditions; the verification results are shown in Fig. 11. These results show that errors between FEA and real experiments are less than 2 %. Consequently, the FEA can replace the real experiment in this paper.

3 RESULT AND DISCUSSION

This section sorts factors in Table 1 according to their importance for the temperature field using the orthogonal experiment data analysed leveraging S/N and ANOVA methods.

3.1 Orthogonal Numerical Experimental Scheme

According to Table 1, we choose the orthogonal table of L_{25} (5^6) (see Table 2), which is composed of 25

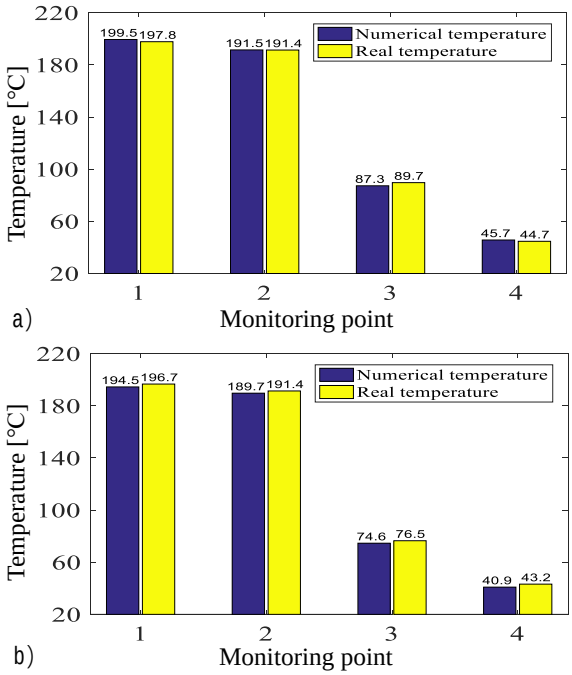

Fig. 11. *Comparison of simulation results and real results; a) wind speed is 3 m/s, and b) wind speed is 2 m/s*

Table 2. *Results and S/N of the orthogonal experiment*

No.	A	B	C	D	E	Result	S/N
1	1	1	1	1	1	133.61	42.517
2	1	2	3	4	5	149.26	43.479
3	1	3	5	2	4	149.76	43.508
4	1	4	2	5	3	144.07	43.171
5	1	5	4	3	2	142.52	43.078
6	2	1	5	4	3	144.50	43.197
7	2	2	2	2	2	142.72	43.090
8	2	3	4	5	1	140.97	42.983
9	2	4	1	3	5	148.27	43.421
10	2	5	3	1	4	156.39	43.884
11	3	1	4	2	5	152.52	43.667
12	3	2	1	5	4	150.66	43.560
13	3	3	3	3	3	150.14	43.530
14	3	4	5	1	2	149.43	43.489
15	3	5	2	4	1	146.38	43.310
16	4	1	3	5	2	146.73	43.330
17	4	2	5	3	1	149.68	43.503
18	4	3	2	1	5	159.68	44.065
19	4	4	4	4	4	158.48	43.999
20	4	5	1	2	3	153.71	43.734
21	5	1	2	3	4	152.07	43.641
22	5	2	4	1	3	153.42	43.718
23	5	3	1	4	2	152.5	43.665
24	5	4	3	2	1	150.51	43.551
25	5	5	5	5	5	162.98	44.243

(Note: The room temperature is 20 °C, and the thermal equilibrium temperature is 200 °C.)

experiments. The evaluation index is the temperature difference between T_2 and T_4 in Fig. 8, and the average value of each factor is calculated to obtain the range value.

3.2 Numerical Experimental Data Analysis

According to the range analysis in Table 3, the importance order of these factors can be concluded: A > E > B > C > D. Consequently, we can preliminarily infer that influences of wind velocity and dam depth are the largest.

Table 3. *Range analysis of the orthogonal experiment*

No.	A	B	C	D	E	blank
k1	143.84	145.89	147.75	150.51	144.23	149.59
k2	146.57	149.15	48.98	149.84	146.78	149.09
k3	149.83	150.61	150.61	148.54	149.17	148.91
k4	153.66	150.15	149.58	150.22	153.47	151.03
k5	154.30	152.40	151.27	149.08	154.54	149.57
R	10.45	6.51	3.52	1.97	10.31	---

To further highlight the influences of these factors, S/N analysis data are illuminated in Fig. 12, in which the level of these factors is taken as the abscissa. The strain S/N ratio is taken as a trend graph for every factor.

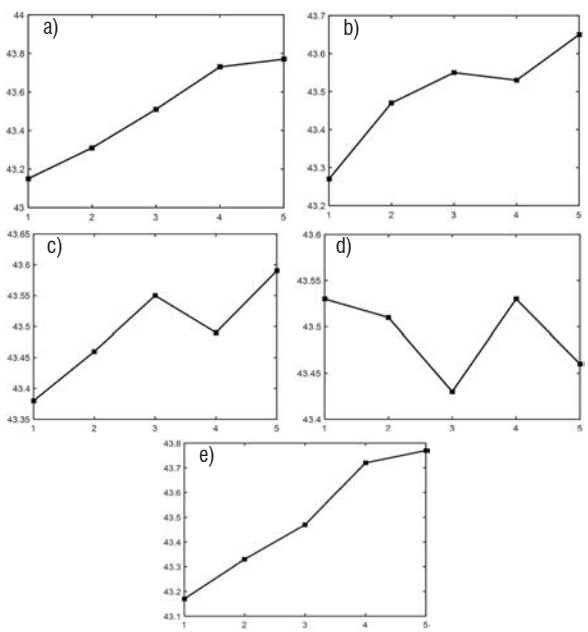

Fig. 12. *Main effect plot for S/N ratio; a) factor A, b) factor B, c) factor C, d) factor D, and e) factor E*

According to the S/N analysis diagram, we further analyse the influence of the level of each

factor. According to data in Table 3, we select the factor A, B, and E to conduct a second orthogonal test (see Table 4) because they have greater impact level values.

Table 4. *Preferred levels of designed parameters*

Factors	A	B	C	D	E
1	5(1)	5(1)	3	4.5	1.5(1)
2	5(1)	3(2)	3	4.5	1.25(2)
3	4(2)	5(1)	3	4.5	1.25(2)
4	4(2)	3(2)	3	4.5	1.5(1)

Analysis results of ANOVA are shown in Table 5, which shows the importance order is A > E > B > C > D. The experiment shows that wind velocity is the most important factor. Under the optimal wind velocity, shape parameters of heat dams are optimized to maximize the temperature difference. The result conforms to the main effect diagram.

Table 5. Analysis of variance (ANOVA)

Source	SS^2	*DOF*	*MS*	*F*	*p*
A	404.3	4	10.06	18.872	0.003
B	115.67	4	5.38	5.397	0.032
C	37.98	4	3.08	1.772	0.177
D	13.31	4	1.85	0.662	0.516
E	381.92	4	9.77	17.828	0.004
Error	13.9	4	1.86	---	---
Total	967.08	24	---	---	---

3.3 Orthogonal Real Experiments

According to the above analysis, we selected several parameters as the factors of a second orthogonal experiment (see Table 4): the wind velocity (A), the groove number (B), and the dam depth (E). Each of these factors takes two-level values. The level values of the factors C and D are fixed, and the L_4 (2^2) orthogonal test is designed. The experimental results consist of T_1, T_3, T_4, and *t*. The position of T is shown in Fig. 8, and *t* is the thermal equilibrium time.

Table 6. *The result of the real experiment*

No.	A	B	E	T_1	T_3	T_4	*t* [s]
1	1	1	1	189.2	90.2	36.1	148
2	1	2	2	188.5	86.9	33.3	151
3	2	1	2	180.4	72.7	35.1	121
4	2	2	1	178.9	71.3	37.1	118

As shown in Table 6, it is found that the temperature of the nozzle at 4 m/s is higher than that at 5 m/s, and the balance time is also lower than the latter, so the optimal wind velocity is 4 m/s. To make the temperature distribution more uniform, the optimal number of grooves is 5, the groove depth is 1.25 mm, and the optimal design parameter level is shown in Table 6.

3.4 Discussion on Experimental Results

According to the experimental data analysis, the following conclusions can be drawn:

(1) The temperature difference of the throat increases obviously along with the increase of wind speed. Therefore, this factor has the greatest influence on the temperature field. However, an excessive wind speed will increase the thermal equilibrium time and reduce the equilibrium temperature of the heater. The most suitable wind speed is 4 m/s.

(2) The groove plays an important role to prevent heat-conducting along the throat. It replaces the radiator and then reduces the volume of the hot end. The groove number is proportional to the temperature difference. The optimal groove number is 5.

(3) The groove depth is the third important factor. When there are 5 grooves, 1.25 mm to 1.5 mm groove depth is suitable. In consideration of the strength of the throat, 1.25 mm is optimal.

(4) The groove width and dam width are not significant. Therefore, 3 mm and 5 mm are selected, respectively, following the principle of maximum strength.

Table 7 lists optimal design parameters for the throat-extended extruder.

Table 7. *The optimum level of design parameters*

Factor	Wind velocity	Groove number	Dam width	Groove depth	Dam depth
Optimal level	4 m/s	5	3 mm	5 mm	1.25 mm

3.5 Manufacturing Accuracy Analysis

Six blocks with designed size 20 mm × 20 mm × 40 mm are printed by the extruder and a usual extruder using polylactic acid (PLA), acrylonitrile butadiene styrene (ABS), and polycarbonate (PC) materials, as shown in Fig. 13. The shape size, surface roughness and proper alignment are measured by the rough-meter, the micrometre calliper, and the dial indicator, respectively. These measured data are listed in Table 8, from which it can be found: (i) PLA has the highest geometrical accuracy, which is the reason that we use

PLA to test our 5-axis printer; (ii) blocks printed by our extruder and blocks printed by usual extruders have a similar geometrical accuracy, which shows that our extruder is valid.

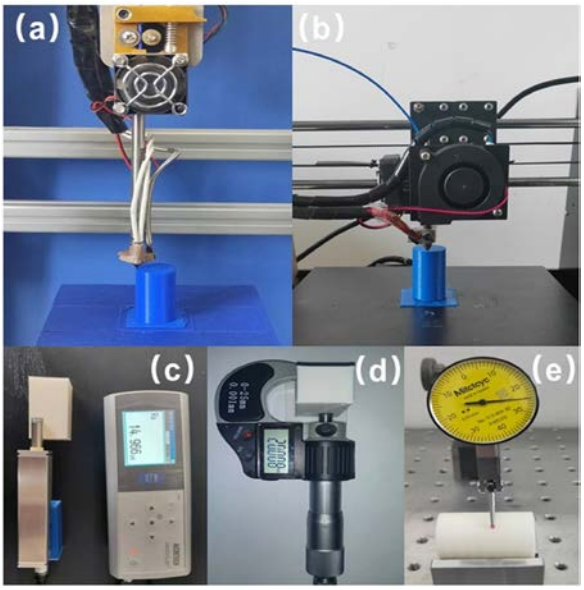

Fig. 13. *The printing process and measurement of the testing specimen; a) 5-axis printing, b) 3-axis printing, c) surface roughness measuring. d) dimension error measuring, e) proper alignment measuring*

Table 8. *Manufacturing accuracy of the testing specimen with different materials*

Properties	Type	PLA	ABS	PC
Surface roughness	3-axis	15.37	16.33	15.97
Ra [μm]	5-axis	13.54	15.89	15.67
Dimension error	3-axis	0.39	0.27	0.48
Δl [mm]	5-axis	0.15	0.33	0.25
Proper alignment	3-axis	Φ0.09	Φ0.15	Φ0.17
Δd [mm]	5-axis	Φ0.06	Φ0.12	Φ0.11

3.6 3D Printing Tests

To verify the effectiveness of the extruder, several workpieces are printed using the extruder. The experimental 5-axis printer and the extruder are shown in Fig. 10. The most suitable filament is PLA according to Table 8. Nozzles respectively with 0.4 mm, 0.6 mm, and 1.0 mm diameter are used in the extruder so that the printer can print several types of workpieces including 2.5-axis 3D printing with AC-axis periodical movement, five-axis linkage FDM cladding, and five-axis linkage 3D printing. The relationship among some 3D processing parameters and the fused filament volume $V_{printed}$ are:

$$V_{printed} = A \cdot s = [(w - h_f) \cdot h_f + \pi(\frac{h_f}{2})^2] \cdot s, \quad (2)$$

$$V_{printed} = S_f \cdot L. \quad (3)$$

In Eqs. (2) and (3), w is the fused material placement width, h_f is the layer height, s is the printing speed. The maximum of $V_{printed}$ in a unit time is closely related to the heater. It can be verified by experiments. The method to evaluate $V_{printed}$ is to extrude silk using the 1.0 mm nozzle while the speed s gradually increases until the nozzle is jammed. The maximum speed is 910 mm/min. Using the value, the maximum speed s for every nozzle can be calculated. S_f is the cross-section area of the filament. L is the extruded filament length. When $V_{printed}$, w, h_f, and S_f are given, s and L can be calculated. In this paper, we use the single factor experiment method to determine these optimal processing parameters. The optimal ones for different nozzles are listed in Table 9.

Table 9. *Process parameter values*

Diameter [mm]	h_f [mm]	w [mm]	s [mm/min]	L [mm]
0.4	0.2	0.2	2000	33.26
0.6	0.3	0.3	1500	56.13
1.0	0.5	0.5	700	72.56

(Note: h: layer height; w: silk placement width; s: print speed; L: extruded filament length)

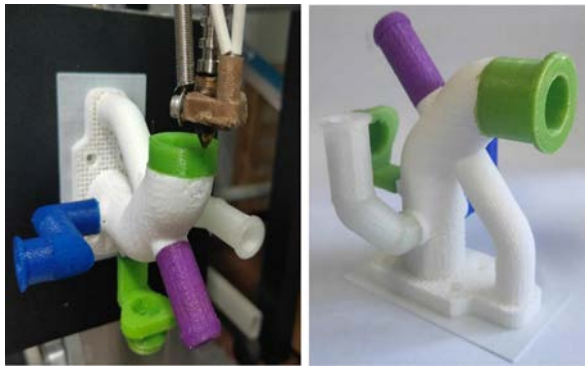

Fig. 14. *Multi-branch models printed by AC-axis periodical movement (nozzle diameter: 0.4 mm)*

Under the optimal level combination, nozzles with 0.4 mm, 0.6 mm, and 1.0 mm diameters are used in the extruder, and several workpieces are printed. From Fig. 14, we can find that distances between branch parts are restricted by sizes of the heater block in the x-direction and the y-direction because these parts cannot be printed at the same time. For Fig. 15a,

when a concave spherical surface is cladded, there is a similar colliding possibility for a conventional extruder. In Fig. 15b, several blades are printed.

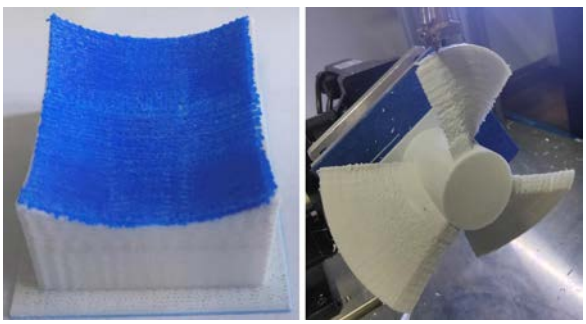

a) b)

Fig. 15. *Concave surface cladded and turbine printed by 5-axis linkage movement; a) 0.6 mm, and b) 1.0 mm*

4 CONCLUSIONS

This paper presents a throat-extended extruder so that a 5-axis FDM printer can print more details and clad more complex surfaces. Compared with a conventional filament FDM extruder, the throat-extended extruder is composed of a smaller heater block, an extended nozzle throat with heat dams, and wind-speed-adjustable cooling equipment. This paper optimizes those shapes and parameters by using several types of constraints: milling tools, heat-insulating tape, smaller *XY*-projection area of the heater block, a smaller quality of the heater block, the larger temperature difference between the hot end and cold end. The extruder is equipped with a 5-axis FDM printer. Several workpieces with complex shapes have been printed by the extruder using different types of nozzles. These experiments show the throat-extended extruder can steadily work in a 5-axis FDM printer with different nozzles. It can print various workpieces that cannot be printed with conventional FDM extruders.

5 ACKNOWLEDGEMENTS

This project is supported by the National Natural Science Foundation of China (Grant No. 51975281 and 51705183).

6 REFERENCES

[1] Wulle, F., Coupek, D., Schäffner, F., Verl, A., Oberhofer, F., Maier, T. (2017). Workpiece and machine design in additive manufacturing for multi-axis fused deposition modeling. Procedia CIRP, vol. 60, p. 229-234, **DOI:10.1016/j.procir.2017.01.046**.

[2] Liu, H., Liu, L., Li, D., Huang, R., Dai, N. (2020). An approach to partition workpiece cad model towards 5-axis support-free 3d printing. *The International Journal of Advanced Manufacturing Technology*, vol. 106, p. 683-699, **DOI:10.1007/s00170-019-04495-3**.

[3] Wei, X., Qiu, S., Zhu, L., Feng, R., Tian, Y., Xi, J., Zheng, Y. (2018). Toward Support-Free 3D Printing: A Skeletal Approach for Partitioning Models. *IEEE Transactions on Visualization and Computer Graphics*, vol. 24, no. 10, p. 2799-2812, **DOI:10.1109/TVCG.2017.2767047**.

[4] Dai, C., Wang, C.C. L., Wu, C., Lefebvre, S., Fang, G., Liu, Y.-J. (2018). Support-free volume printing by multi-axis motion. *ACM Transactions on Graphics*, vol. 37, no. 4, p. 1-14, **DOI:10.1145/3197517.3201342**.

[5] Calleja, A., Tabernero, I., Fernández, A., Celaya, A., Lamikiz, A., López de Lacalle, L.N. (2014). Improvement of strategies and parameters for multi-axis laser cladding operations. *Optics and Lasers in Engineering*, vol. 56, p. 113-120, **DOI:10.1016/j.optlaseng.2013.12.017**.

[6] Kapil, S., Negi, S., Joshi, P., Sonwane, J., Sharma, A., Karunakaran, K.P. (2017). 5-axis slicing methods for additive manufacturing process. *Proceedings of the 28th Annual International Solid Freeform Fabrication Symposium*, p. 1886-1896.

[7] Saeed Daneshmand, S., Aghanajafi, C. (2012). Description and modeling of the additive manufacturing technology for aerodynamic coefficients measurement. *Strojniški vestnik-Journal of Mechanical Engineering*, vol. 58, no. 2, p. 125-133, **DOI: 10.5545/sv-jme.2010.238**.

[8] Budzik, G., Burek, J., Bazan, A., Turek, P. (2016). Analysis of the accuracy of reconstructed two teeth models manufactured using the 3DP and FDM technologies. *Strojniški vestnik - Journal of Mechanical Engineering*, vol. 62, no. 1, p. 11-20, **DOI:10.5545/sv-jme.2015.2699**.

[9] Valentan, B., Brajlih, T., Drstvenšek, I., Balič, J. (2011). Development of a part-complexity evaluation model for application in additive fabrication technologies. *Strojniški vestnik - Journal of Mechanical Engineering*, vol. 57, no. 10, p. 709-718, **DOI:10.5545/sv-jme.2010.057**.

[10] Homar, D., Pušavec, F. (2017). The development of a recognition geometry algorithm for hybrid – subtractive and additive manufacturing. *Strojniški vestnik - Journal of Mechanical Engineering*, vol. 63, no. 3, p. 151-160, **DOI:10.5545/sv-jme.2016.3924**.

[11] Pollák, M., Kaščak, J., and Tkáč, J. (2019). Design of the 3D printhead with extruder for the implementation of 3D printing from plastic and recycling by industrial robot. *TEM Journal*, vol. 8, no. 3, p. 709-713, **DOI:10.18421/TEM83-02**.

[12] Whyman, S., Arif, K.M., Potgieter, J. (2018). Design and development of an extrusion system for 3D printing biopolymer pellets. *The International Journal of Advanced Manufacturing Technology*, vol. 96, p. 3417-3428, **DOI:10.1007/s00170-018-1843-y**.

[13] Goyanes, A., Allahham, N., Trenfield, S.J., Stoyanov, E., Gaisford, S., Basit, A.W. (2019). Direct powder extrusion 3D printing: Fabrication of drug products using a novel single-step

process. *International Journal of Pharmaceutics*, vol. 567, **DOI:10.1016/j.ijpharm.2019.118471**.

[14] Justino Netto, J.M., Silveira, Z.D.C. (2018). Design of an innovative three-dimensional print head based on twin-screw extrusion. *ASME Journal of Mechanical Design*, vol. 140, no. 12, art. ID 125002, **DOI:10.1115/1.4041175**.

[15] Gibson, I., Rosen, D., Stucker, B. (2015). *Additive Manufacturing Technologies,* Springer, New York.

[16] Abilgaziyev, A., Kulzhan, T., Raissov, N., Ali, M.H., Match, W.L.KO., Mir-Nasiri, N. (2015). Design and development of multi-nozzle extrusion system for 3D printer. *International Conference on Informatics, Electronics & Vision*, **DOI:10.1109/ICIEV.2015.7333982**.

[17] Obias Hullette, All3DP, Direct vs Bowden Extruder: Does It Make a Difference? from *https://all3dp.com/2/direct-vs-bowden-extruder-technology-shootout/*, accessed on 2020-10-01.

[18] Han, S., Xiao, Y., Qi, T., Li, Z., Zeng, Q. (2017). Design and analysis of fused deposition modeling 3D printer nozzle for color mixing. *Advances in Materials Science and Engineering*, art. ID 2095137, **DOI:10.1155/2017/2095137**.

[19] Fok, K.-Y., Cheng, C.-T., Ganganath, N., Iu, H.H.-C., Tse, C.K. (2019). An ACO-based tool-path optimizer for 3-D printing applications. *IEEE Transactions on Industrial Informatics*, vol. 15, no. 4, p. 2277–2287, **DOI:10.1109/TII.2018.2889740**.

[20] Abdulhameed, O., Al-Ahmari, A., Ameen, W., Mian, S.H. (2019). Additive manufacturing: challenges, trends, and applications. *Advances in Mechanical Engineering*, vol. 11, no. 2, **DOI:10.1177/1687814018822880**.

[21] Jin, Y., He, Y., Fu, J., Gan, W., Lin, Z. (2014). Optimization of tool-path generation for material extrusion-based additive manufacturing technology. *Additive Manufacturing*, vol. 1-4, p. 32-47, **DOI:10.1016/j.addma.2014.08.004**.

[22] Duty, C.E., Love, L.J. (2015). Big Area Additive Manufacturing (BAAM), Cincinnati Incorporated, from *https://www.e-ci.com/baam/*, accessed on 2021-04-10, **DOI:10.2172/1210140**.

[23] Molitch-Hou, M. (2018). Overview of Additive Manufacturing Process. Zhang, J., Jung, Y-G. (eds.) *Additive Manufacturing*, Elsevier, p. 1-38, **DOI:10.1016/B978-0-12-812155-9.00001-3**.

[24] Go, J., Hart, A.J. (2017). Fast desktop-scale extrusion additive manufacturing. *Additive Manufacturing*, vol. 18, p. 276-284, **DOI:10.1016/j.addma.2017.10.016**.

[25] Löffler, R., Koch, M. (2019). Innovative extruder concept for fast and efficient additive manufacturing. *IFAC-PapersOnLine*, vol. 52, no. 10, p. 242-247, **DOI:10.1016/j.ifacol.2019.10.071**.

[26] Huang, B., Singamneni, S.B. (2015). Curved layer adaptive slicing (CLAS) for fused deposition modelling. *Rapid Prototyping Journal*, vol. 21, no. 4, p. 354-367, **DOI:10.1108/RPJ-06-2013-0059**.

[27] Turner, B.N., Strong, R., nd A. Gold, S.A. (2014). A review of melt extrusion additive manufacturing processes: I. Process Design and Modeling. *Rapid Prototyping Journal*, vol. 20, no. 3, p. 192-204, **DOI:10.1108/RPJ-01-2013-0012**.

[28] Bellini, A., Güçeri, S., Bertoldi, M. (2004). Liquefier dynamics in fused deposition. *Journal of Manufacturing Science and Engineering*, vol. 126, no. 2, p. 237-246, **DOI:10.1115/1.1688377**.

[29] Ramanath, H.S., Chua, C.K., Leong, K.F., Shah, K.D. (2008). Melt flow behavior of poly-ε-caprolactone in fused deposition modelling. *Journal of Materials Science: Materials in Medicine*, vol. 19, no. 7, p. 2541-2550, **DOI:10.1007/s10856-007-3203-6**.

[30] Manikandan, N., Vignesh, T., Prasath, C., Ismail, M. (2020). Thermo-mechanical analysis of fused filament fabrication process. *IOP Conference Series: Materials Science and Engineering*, vol. 764, p. 012008, **DOI:10.1088/1757-899X/764/1/012008**.

[31] Lužanin, O., Movrin, D., Plančak, M. (2013). Experimental investigation of extrusion speed and temperature effects on arithmetic mean surface roughness in FDM built specimens. *Journal for Technology of Plasticity*, vol. 38, no. 2, p. 179-189, **DOI:10.1007/s00170-019-03859**.

[32] Kozior, T., Mamun, A., Trabelsi, M. (2020). Quality of the surface texture and mechanical properties of FDM printed samples after thermal and chemical treatment. *Strojniški vestnik - Journal of Mechanical Engineering*, vol. 66, no. 2, p. 105-113, **DOI:10.5545/sv-jme.2019.6322**.

[33] Jerez-Mesa, R., Travieso R. (2015). Design of open source 3D printer extruder and modelling of thermal performance with FEA. *19th International Research/Expert Conference: Trends in the Development of Machinery and Associated Technology*.

[34] ISO 724:1993(E). *ISO General-Purpose Metric Screw Threads - Basic Dimensions*. International Organization for Standardization, Geneve.

[35] ANSI H35.2(M) (2017). *American National Standard Dimensional Tolerances for Aluminum Mill Products*. American National Standards Institute. America.

[36] Mert P., Hakan D. (2020). An experimental study for determination of convective heat transfer coefficients on cooling monofilament. *International Journal of Heat and Mass Transfer*, vol. 149, no. 3, p. 11925-11936, **DOI:10.1016/j.ijheatmasstransfer.2019.119255**.

[37] Budzik, G., Turek, P., Dziubek, T., Gdula, M. (2020). Elaboration of the measuring procedure facilitating precision assessment of the geometry of mandible anatomical model manufactured using additive methods. *Measurement and Control*, vol. 53, no. 1-2, p. 181-191, **DOI:10.1177/0020294019881708**.

[38] El-Katatny I., Masood, S.H., Morsi, Y.S. (2010). Error analysis of FDM fabricated medical replicas. *Rapid Prototyping Journal*, vol. 16, no. 1, p. 36-43, **DOI:10.1108/13552541011011695**.

[39] Polak, R., Sedlacek, F., Raz, K. (2017). Determination of FDM printer settings with regard to geometrical accuracy. *Proceedings of the 28th DAAAM International Symposium*, p. 0561-0566, **DOI:10.2507/28th.daaam.proceedings.079**.

[40] Boschetto, A., Bottini, L. (2014). Accuracy prediction in fused deposition modeling. *The International Journal of Advanced Manufacturing Technology*, vol. 73, p. 913-928, **DOI:10.1007/s00170-014-5886-4**.

Strojniški vestnik - Journal of Mechanical Engineering 67(2021)4, 191-199
DOI:10.5545/sv-jme.2021.7101
Original Scientific Paper
Received for review: 2021-01-21
Received revised form: 2021-02-25
Accepted for publication: 2021-03-29

Residual, Corrosion & Tribological Behavior of HVOF Sprayed Sustainable Temperature-Dependent Carbon-Based Hybrid Composite Coating

Ankit Tyagi[1,2,*] – Qasim Murtaza[1] – Ravinderjit Singh Walia[3]
[1] Delhi Technological University, Department of Mechanical Engineering, India
[2] SGT University, Department of Mechanical Engineering, India
[3] Punjab Engineering College, Department of Production & Industrial engineering, India

At present, cost-effective coatings that cause less pollution are in great demand; to decrease frictional losses, carbon-based hybrid composite coatings have been developed using a high-velocity oxy-fuel (HVOF) spray process. The microstructural, tribological, corrosion, and mechanical properties of these coatings have been evaluated using high-resolution X-ray diffraction (HRXRD), field emission scanning electron microscopy-Energy dispersive X-ray Spectroscopy (FESEM-EDS), Raman spectrum, Vickers micro-hardness tester, μ-360 cos(α) residual stress analyser, corrosion tester, and high temperature tribometer. The residual stress, corrosion and tribological behaviour at high temperatures were investigated using a pin-on-disc high-temperature tribometer. The tribological performance was evaluated using a high-temperature tribometer, and the experimental result shows that a coefficient of friction (COF) varies from 0.12 to 0.52, while wear results were in the range of 45 μm to 120 μm, as the test condition of temperature ranging from 50 °C to 350 °C, load from 60 N to 90 N and sliding velocity from 0.1 m/s to 0.4 m/s respectively. The experimental results of corrosion testing show that the mass loss decreases from 0.10 g to 0.04 g, when samples were dipped for 1 h; when the samples were dipped for 8 h, the mass loss of hybrid composite coating varied from 0.12 g to 0.045 g. The tribological test showed a 78.9 % increase in micro-hardness, a 78 % decrease in residual stress, and 60 % and 62.5 % decreases in mass loss due to corrosion at 1 h and 8 h, respectively, a 76.9 % decrease in COF and 62.5 % reduction in the wear at test condition of 350 ºC temperature, a sliding velocity of 0.4 m/s and 90 N load.
Keywords: HVOF carbon coating, FESEM, HRXRD, Raman spectra test, corrosion, wear test

Highlights
- *The experimental results showed micro-hardness in the range of 380 HV to 680 HV and residual stress from –11 MPa to –50 MPa.*
- *The corrosion test shows that the mass loss of hybrid composite coating varies from 0.12 g to 0.045 g for 8 h.*
- *The COF were found in the range of 0.12 to 0.52, while wear was in the range of 45 μm to 120 μm.*
- *The tribological test showed a 78.9 % increase in micro-hardness, a 78 % decrease in residual stress, a 62.5 % decrease in mass loss due to corrosion at 8 h, a 76.9 % decrease in COF, and a 62.5 % reduction in the wear.*

0 INTRODUCTION

The past century observed a wide range of development in the automotive, marine and aerospace industries. Among assorted challenges in the automotive and marine environment, cavitation and erosion are prominent causes in the failure of engineering components, such as pumps, engines, blades, and ship propellers [1] and [2]. The general phenomenon in hydraulic systems involves a bombardment of gas bubbles on the component surface that leads to erosion, and fatigue failure, which finally deteriorate the performance of valuable and crucial equipment [3] and [4]. Surface modification offers an economical and effective methodology to tackle cavitation and erosion problem on the component surface. Thermal spray is a surface modification method that can fabricate coatings with broad feedstock materials and high deposition rate and effective for cavitation and erosion protection [5] and [6]. The experimental investigation of Qiao et al. [7] observed that high-velocity oxy-fuel (HVOF) sprayed Fe amorphous coating exhibits high cavitation erosion resistance. Among coating materials, tungsten carbide (WC)-based composite coatings or hard metals are significant sort of materials with a diverse range of governable properties, such as surface energy, wear, hardness, corrosion resistance and toughness, due to their unique virtues of the binder phase and hard phase [8] to [12]. Recently, a comparative study was carried out by Zhang et al. [13], which determined that among several thermal spray coating, WC based composite coating have excellent cavitation erosion resistance. Detonation spraying, HVOF spraying, plasma

*Corr. Author's Address: SGT University, Gurgram, Haryana, India, tyagiankit10506@yahoo.com

spraying and cold spraying are the most commonly used techniques for WC-based coating deposition [14] to [16]. Cheng et al. [17] studied the wear resistance behaviour, hardness and elastic behaviour of arc-sprayed coating and concluded that all the properties are enhanced with high H/E, H^3/E^2, and η value. The experimental study further concluded that high H/E, H^3/E^2, and η value enhances product and service life and other properties. Another study, by Hong et al. [18] on the Cr3C2-NiCr (CN) and WC-Cr3C2-Ni (WCN) HVOF sprayed coating for corrosion and wear resistance concluded that CN coating retains lower E and H values with high porosity, while WCN coating has higher H^3/E^2 and H/E values and lower porosity. The HVOF method is the best apposite process for ceramic coating materials due to the low flame temperature and high velocity of melted particles. According to [19], HVOF-based WC-10Co-4Cr coating exhibits excellent slurry erosion resistance on comparing with uncoated steel plate. One fascinating outcome for WC-based coating were improvements in toughness and hardness, using nano-sized WC particles [20] and [21] and, due to decarburization [22], occasionally negative results were reported. To overcome decarburization, multimodal feedstock powder was used but employment of HVOF techniques proves effective in enhancement of particle velocity and in lowering of flame temperature [23] and [24].

Corrosion and erosion are critical and an inevitable issue for the constituent's surface exposed to the engine and marine environment that typically complicate the problem. Wentzel and Allen [25] investigated pure Ni binder and observed poor wear and corrosion wear performance despite good static corrosion results. The combined mechanisms are crucial for the coating fabrication and selection of material for coating, which has not been implicit in previous studies.

The present work aims to explicate the influence of HVOF sprayed sustainable temperature-dependent carbon-based hybrid composite coating on wear, coefficient of friction (COF), corrosion, residual stress, and hardness. The analysis of COF, wear, and corrosion behavior was well supported by field emission scanning electron microscopy (FESEM), Raman spectrum and high-resolution X-ray diffraction (HRXRD) observation. This work focused to evaluates the microstructure, surface morphology, tribological and mechanical properties of hybrid composite coating, using a high-temperature pin-on-disk tribometer, at test condition of temperature ranging from 50 °C to 350 °C, load from 60 N to 90 N and sliding velocity from 0.1m/s to 0.4 m/s, respectively

1 EXPERIMENTAL

1.1 Coating Preparation

Carbon-based hybrid composite powders were used for the fabrication of high quality coating for wear resistance applications. The fabrication process initially involved mixing of micron size $C+Mo+WC+TiO_2+Al_2O_3$ powders of the same proportion using a ball mill process followed by thermal spraying and sintering. The ball-milling operation was performed for homogeneous and uniform distribution of carbon powder throughout the composite powder. A MEC - HIPOJET® 2700 HVOF spraying system was used to deposit a carbon-based hybrid composite coating on 100 mm × 100 mm × 50 mm steel substrate. Prior to spraying, the substrates were properly cleaned with emery paper and were grit-blasted with 60 mesh SiC, using the pressurized air jet of sandblaster with a blasting pressure of 70 psi from 50 mm distance, followed by surface cleaning with acetone. The optimized spraying parameters for HVOF coating were 45 m^3/h oxygen flux, 15 l/h LPG flux, 100 mm spraying distance, 60 g/min powder feed rate.

1.2 Characterization & Wear Test

The surface morphology and structural composition of fabricated coating were characterized using JOEL FESEM-EDS. PANalytical HRXRD systems were used to identify and confirm the phase and crystal structure using the Cu anode material in Bragg mode. A Renishaw micro-Raman spectrometer was deployed to identify elemental peaks of fabricated coating with spectral range (3500 cm^{-1}) and resolution about 1 cm^{-1}.

The micro-hardness of the developed carbon coating was evaluated using an Hm2000S Make Vickers hardness tester (Fischer scope). The micro-hardness tester with a diamond stylus was used to perform tests with indentation time of 20 s, dwell time of 5 s and a maximum applied load of 1000 mN on the stylus. The residual stress analyser (μ-X360, XRD) was used to evaluate the internal stresses developed on the carbon coatings.

The pin-on-disk tribometer was used to examine the tribological behavior (COF & wear) of carbon-based hybrid composite coatings. The DHM850 high-temperature tribometer, with a temperature

range of ambient –800 °C, load 20 N to 200 N and sliding velocity of 0.1 m/s to –10 m/s was used for the experimental investigation of wear and COF. The test conditions of wear and COF were given in Table 1, where C is the carbon-based hybrid coating, and suffixes 01, 02, 03 and 04 were used to differentiate the test conditions of the composite coating. The experimental tests for COF and wear were conducted with ASTM G99 standards without lubrication, G99 grade pin with a diameter of 8mm and a surface roughness of 10 nm; the temperature varies from 50 °C to 350 °C, the load from 60 N to 90 N, and the sliding velocity from 0.1 m/s to 0.4 m/s.

The corrosion test was conducted with ASTM G111 standards in an electrolyte solution. The electrolyte solution was formed by mixing 3.5 wt% of NaCl powder in 1000 ml distilled water. The samples of the high-temperature wear test were dipped in the electrolyte solution for 1 and 8 h, for mass loss analysis.

Table 1. *Details of experiment for wear test*

No.	Parameter	C01	C02	C03	C04
1	Temperature [°C]	50	150	250	350
2.	Load [N]	60	70	80	90
3.	Sliding velocity [m/s]	0.1	0.2	0.3	0.4

2 RESULTS & DISCUSSIONS

2.1 Coating Characterization

Fig. 1a to c illustrates the FESEM image of the surface and cross-sectional morphology along with bonding conformity of carbon-based hybrid composite coatings. It is quite clear from FESEM image at ×1000 and ×500 that flake-like structures are seen along with presence of semi-molten, molten, and un-melted grains of composite particles along with formation of lamellae. Fig. 1c shows carbon coating was deposited uniformly and homogeneously, ranging from 400 µm to 450 µm. Fig. 1d to f shows the EDS mapping results of composite coating and confirms the deposition of wt% in the developed coating as 28 % carbon, 8 % oxygen. Fig. 1f shows the HRXRD spectra on the carbon-based hybrid composite coating. In the present case, peaks at 2Θ = 9° to 9.5°, 2Θ = 18.5° to 19°, 2Θ = 26° to 27°, 2Θ = 35° to 36°, 2Θ = 48° to 48.5° and at 2Θ = 54° to 55°, 2Θ = 65°, and 73° to 78° and many other small peaks respectively were observed on the fabricated coating. The prominent peaks on the coating were at 2Θ = 26° to 27°, 2Θ = 35° to 36°, and 2Θ = 48° to 48.5°. The HRXRD results confirm the formations of carbides, oxides and sulphides phases within the coating [26]. Fig. 1g shows the captured Raman spectra peak on the developed coating with the presence of hybridized carbon peak. To examine the structural properties of coating materials, Raman spectroscopy has been used by the researchers. In the present research, prominent peaks were observed at 1120 cm^{-1} to1140 cm^{-1}, 1340 cm^{-1} to 1360 cm^{-1} and 1550 cm^{-1} to 1590 cm^{-1} on the carbon-based hybrid composite coating. It is noted that peaks around 1340 cm^{-1} to 1350 cm^{-1} and at 1120 cm^{-1} to 1140 cm^{-1} show sp^1 or sp^2 hybridized carbon deposition on the developed coating, while peaks around 1550 cm^{-1} to 1590 cm^{-1} shows presence of sp^3 hybridization with presence of diamond-like carbon (DLC) coating as testified in formerly research [26] to [28].

2.2 Micro-Hardness

The micro-hardness of carbon-based hybrid composite coatings deposited using the HVOF process is shown in Fig. 2a. The experimental results of hardness for fabricated coating shows that as the test condition of temperature ranging from 50 °C to 350 °C, load from 60 N to 90 N and sliding velocity from 0.1 m/s to 0.4 m/s, respectively, rapidly increase hardness from 380 HV to 680 HV. The hardness was found to increase of 79 % at the test condition of 90 N load, 0.4 m/s sliding velocity, and 350 °C temperature. The increase in hardness is due to the hard-ceramic particles, formation of oxides, carbides and sulphides layers, the agglomerate size of powders and the strong adhesive force between coating particles [29]. The experimental result shows as the temperature, load, and velocity increase, the micro-hardness of the carbon-based hybrid composite coating increases significantly, as studied by Tyagi et al. [30], and similar trends were also attained in the present hardness test. Matikainen et al. [31] investigated HVOF-developed coating, and experimental result shows that higher velocity particles enhance the hardness of the coating [32].

2.3 Residual Stress

The residual stress of carbon-based hybrid composite coatings fabricated using HVOF process is shown in Fig. 2b. Mathematically, the residual stress was determined by accurately measuring the position of the Debye rings using the Eqs. (1) and (2) and as shown in Fig. 3. Residual stresses on the coated samples are because biaxial applied load and thermal stresses developed on the body. The experimental results of residual stress for composite coating shows that as the

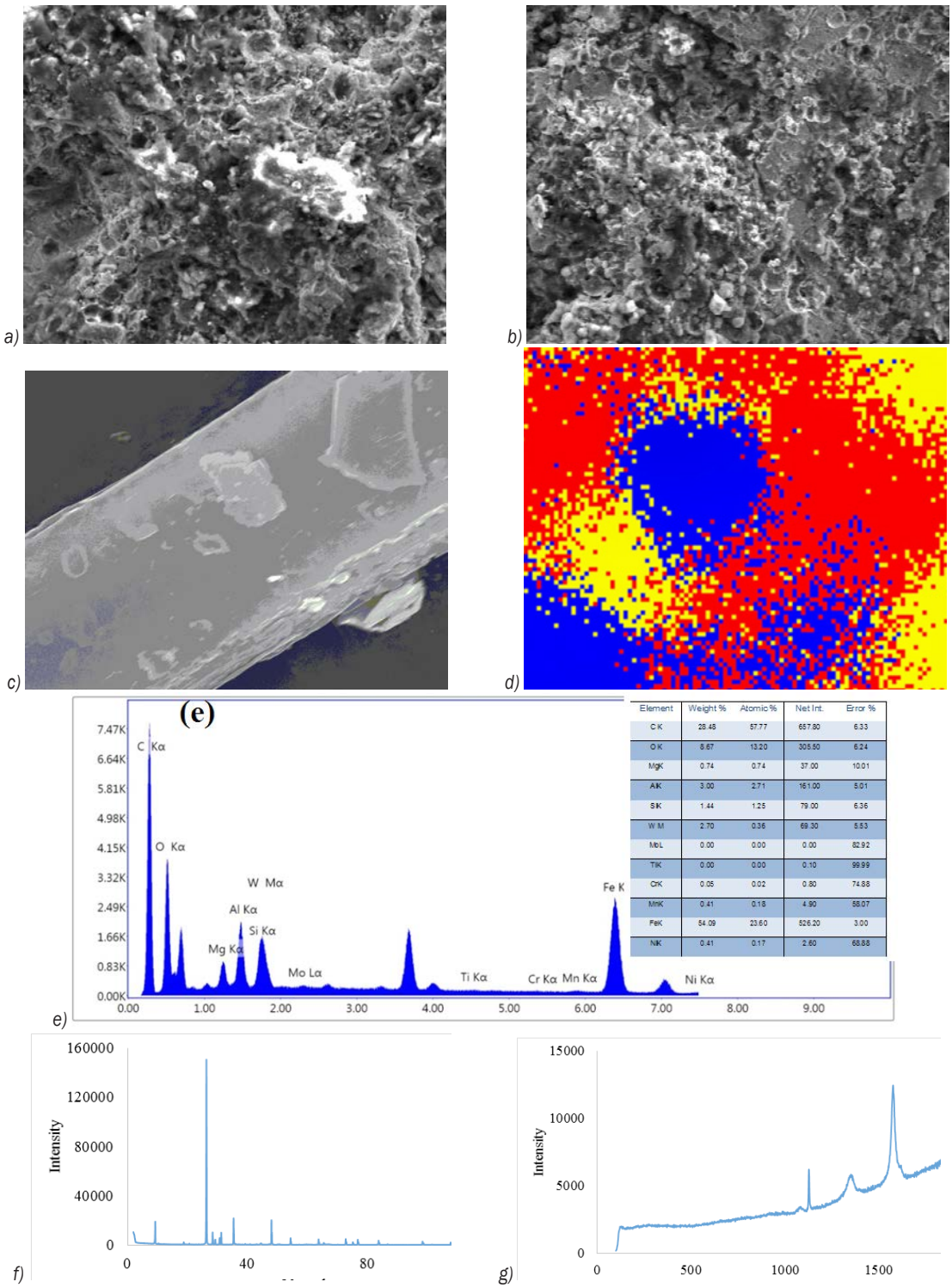

Fig. 1. *Coating characterization; a) to c) SEM; d) to e) EDS mapping result; f) HRXRD; g) Raman spectra image of coating*

test condition of temperature ranging from 50 °C to 350 °C, load from 60 N to 90 N and sliding velocity from 0.1 m/s to 0.4m/s respectively increases residual stress rapidly decreases from –50 HV to –11 HV. The residual stress was found to decrease to 78 % at test condition of 90 N load, 0.4 m/s sliding velocity and 350 °C temperature. Compressive residual stresses are established due to the bombardment of high-

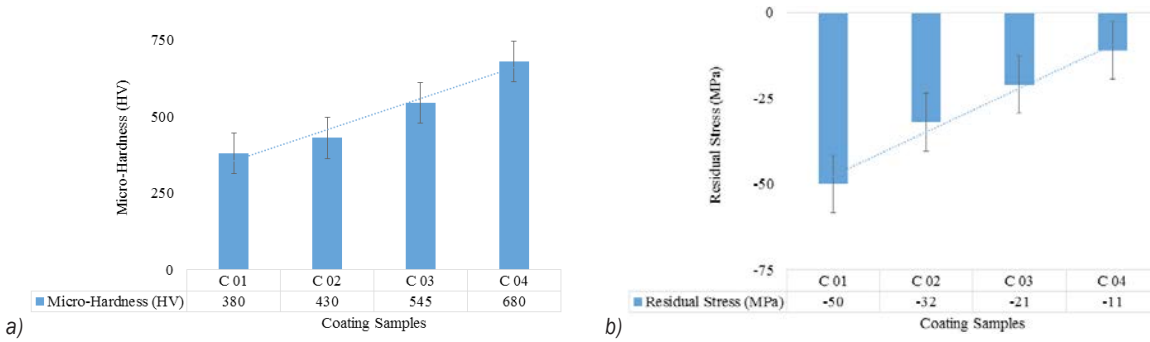

Fig. 2. *a) Micro-hardness vs. coating graph; and b) residual stress of coating vs. coating graph*

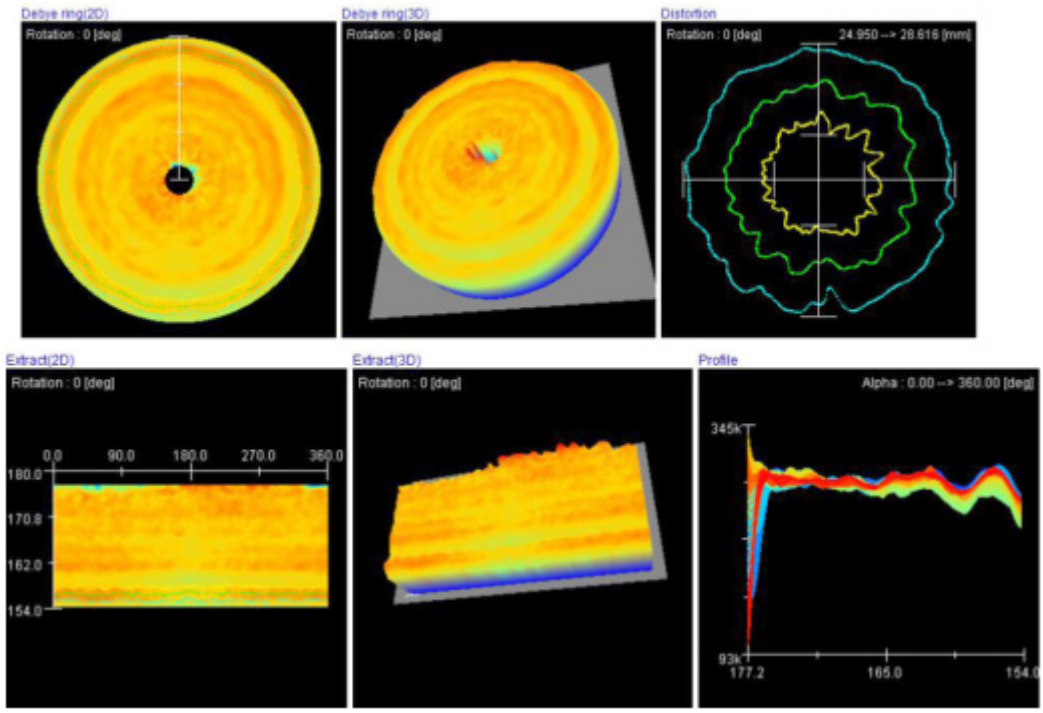

Fig. 3. *Residual stress of coating; a) Debye ring (2D), b) Debye ring (3D), c) distortion, d) extract (2D), e) extract (3D), and f) profile*

velocity particles on the substrate material. Further increases in temperature, load and sliding velocity during the tribological test, and tensile stresses as internal stresses are developed, which balances the compressive stresses developed due to bombardment of hard ceramics particles [29] and [33]. Skordaris et al. [34] reported that as the temperature increases, thermal stresses on the coating also increases, but the structural stress developed on the samples remains stable up to 400 °C.

$$\sigma_x = \frac{E}{1+\nu} \cdot \frac{1}{\sin 2\eta} \cdot \frac{1}{\sin 2\Psi_0} \cdot \frac{\partial \varepsilon \alpha_1}{\partial \cos \alpha}, \quad (1)$$

$$\sigma_y = \frac{E}{2(1+\nu)} \cdot \frac{1}{\sin 2\eta} \cdot \frac{1}{\sin 2\Psi_0} \cdot \frac{\partial \varepsilon \alpha_2}{\partial \cos \alpha}, \quad (2)$$

where σ_x and σ_y is residual stress developed on the surface at the *x*- and *y*-axis, respectively, ν is Poisson ratio, η is diffraction lattice angle, ψ_0 is X-rays incident angle and α is the azimuth angle of Debye ring, E is Young's modulus.

2.4 Corrosion test

Fig. 4 shows the experimental test results of mass loss during corrosion test. The experimental results of corrosion test for the hybrid composite coating shows that as the test condition increases mass loss due to corrosion rapidly decreases from 0.10 g to 0.04 g, when samples were dipped for 1 h. When samples were dipped for 8 h, the mass loss of hybrid composite

coating varies from 0.12 g to 0.045 g. The mass loss was found to decrease by 60 % at 1 h and 62.5 % at 8 h. During the corrosion test, the samples after high temperature wear test were dipped in the electrolytic solution for 1 h and 8 h. The trend of mass loss shows linear relation with time due to corrosion with no acceleration, incubation or steady stage. The presence of carbon and hydrogen leads to a graphitization effect and the formation of sulphide forms a thin solid lubricated layer [30] and [33].

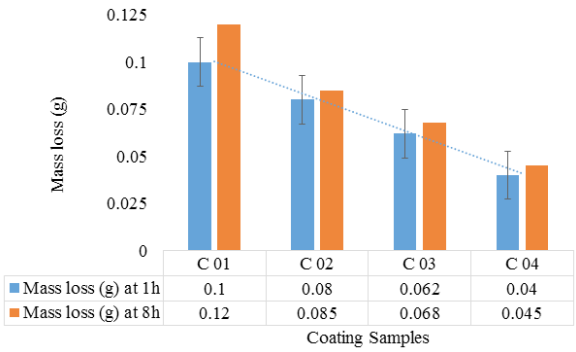

Fig. 4. *Corrosion test of coating*

2.5 Tribological Test

The tribological performance was evaluated using pin-on-disk tribometer, which showed COF in the range of 0.12 to 0.52, as shown in Fig. 5a, while Fig. 5b shows that wear was in the range of 45 µm to 120 µm, at test condition of temperature ranging from 50 °C to 350 °C, load from 60 N to 90 N and sliding velocity from 0.1 m/s to 0.4 m/s, respectively. The tribological analysis of carbon-based hybrid composite coating was done to evaluate the wear behaviour for wear resistance applications. The tribological test showed a 76.9 % decrease in COF and a 62.5 % reduction in the wear at test condition of 0.4 m/s sliding velocity, 350 °C temperature, and 90 N load. During wear testing COF, the wear values first increase and, after that, become stable during the running-in process between the composite coating and its counterpart, due to good interfacial strength and excellent adhesive strength. The presence of carbon and hydrogen leads to a graphitization effect, and the formation of sulphide forms a thin solid lubricated layer [30] and [33]. Tyagi et al. [30] and Matikainen et al. [31] investigated an HVOF-developed coating, and the experimental result shows that higher velocity particles enhance the wear resistance properties of the developed coating; similar trends were also attained in the present tribological study. The experimental results that as the load, velocity, and temperature increases, COF & wear behaviour of carbon coating decreases significantly according to the Stribeck theory [35], and similar trends were also found in the present tribological study. The deviation of friction and wear by sliding distance shows approximately 500 m run-in-stage, followed by a stable stage [36].

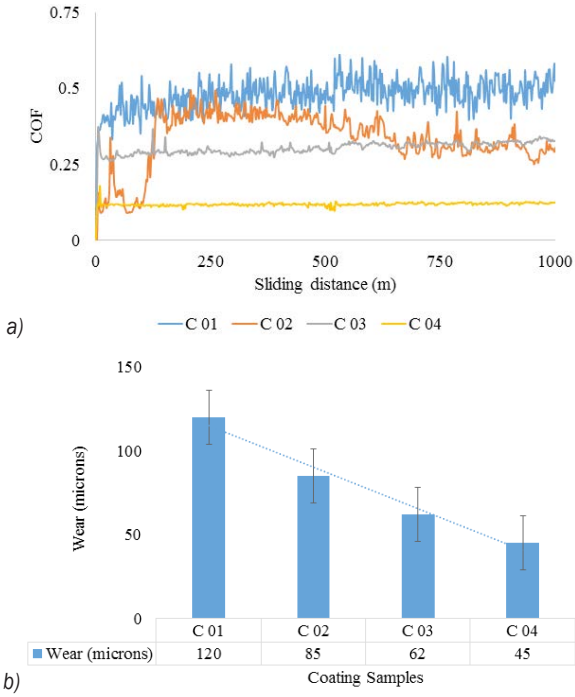

Fig. 5. *a) COF; and b) wear of carbon coating*

2.6 Wear Mechanism

The FESEM images show the wear characteristics of worn surfaces of the developed carbon-based hybrid composite coatings, and shown in Fig. 6a and b. Fig. 6c shows the cross-sectional image of the composite coating after the wear test. FESEM obtained after wear test shows a brittle structure with grains along with the conversion of amorphous to polycrystalline structure of the composite coating. It was quite clear that metallic abrasive particles are entrenched in the developed composite coating or adhesive wear. The carbon-based hybrid composite coating shows ploughing action with the presence of chipped-off particles, rubbing action along with worn out particles were seen during the wear test [33]. It is also noted that the formation of tribofilm and diffusion of carbon particles increases as the test conditions increases [30] and [36].

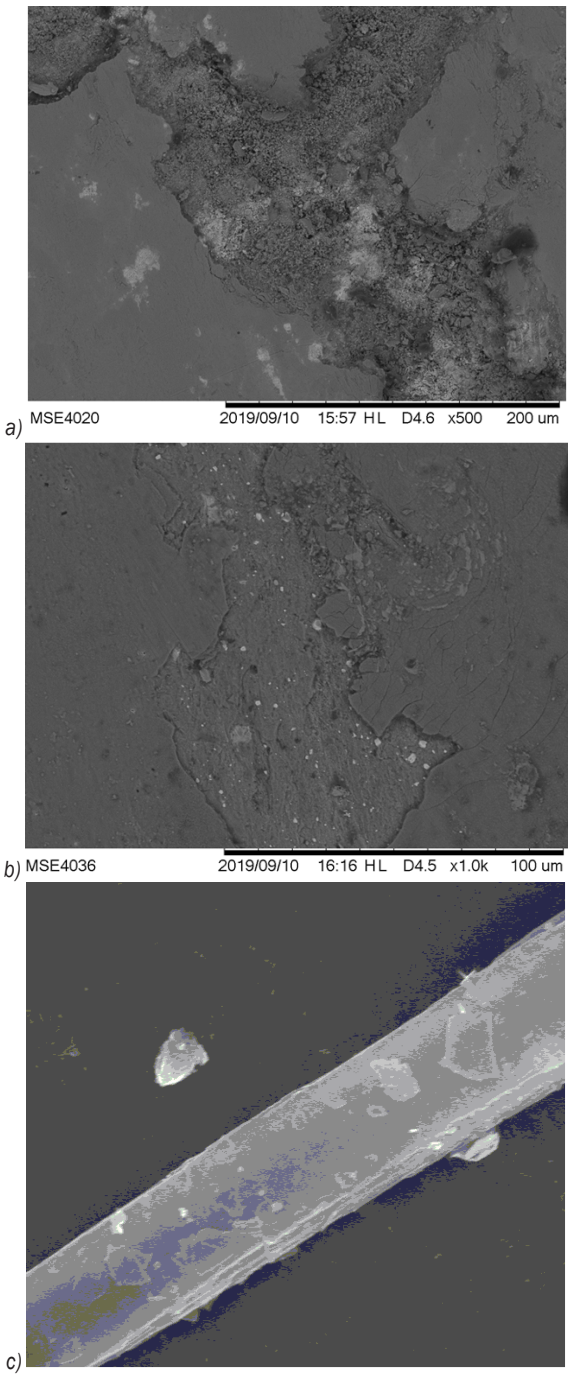

Fig. 6. *a) and b) wear mechanism, and c) coating thickness of carbon coating*

3 CONCLUSIONS

Currently, cost-effective coatings that cause less pollution are in strong demand; to reduce frictional loss, carbon-based hybrid composite coatings have been deposited using an HVOF process. The present work evaluates the microstructure, surface morphology, tribological and mechanical properties of carbon-based hybrid composite coating for wear resistance applications.

The major results of carbon coatings are:

1. FESEM+EDS, HRXED & Raman spectra confirm the deposition of coating, which exhibits typical semi-molten, molten and un-melted grains of composite particles along with the formation of lamellae.
2. The carbon-based hybrid composite coatings exhibit a typical laminar and molten structure, which showed micro-hardness in the range of 380 HV to 680 HV and residual stress from –11 MPa to –50 MPa.
3. The corrosion test result shows that as the test conditions increases, the mass loss decreases from 0.10 g to 0.04 g, when samples were dipped for 1h; when the samples were dipped for 8 h, the mass loss of hybrid composite coating varies from 0.12 g to 0.045 g.
4. The tribological performance was evaluated using a high-temperature tribometer, which showed COF in the range of 0.12 to 0.52, while wear in the range of 45 µm to 120 µm, as the test condition of temperature ranging from 50 °C to 350 °C, load from 60 N to 90 N and sliding velocity from 0.1 m/s to 0.4 m/s, respectively.
5. The tribological test showed a 78.9 % increase in micro-hardness, a 78 % decrease in residual stress, 60 % and 62.5 % decreases in mass loss due to corrosion at 1 h and 8 h, respectively, a 76.9 % decrease in COF and a 62.5 % reduction in the wear at test condition of 350 °C temperature, a sliding velocity of 0.4 m/s and 90 N load.

4 REFERENCES

[1] Basumatary, J., Nie, M., Wood, R.J.K. (2015). The synergistic effects of cavitation erosion– corrosion in ship propeller materials. *Journal of Bio- and Tribo-Corrosion*, vol. 1, no. 12, **DOI:10.1007/s40735-015-0012-1**.

[2] Jasionowski, R., Przetakiewicz, D., Przetakiewicz, W. (2014). Cavitation erosion resistance of alloys used in cathodic protection of hulls of ships. *Archives of Metallurgy and Materials*, vol. 59, **DOI:10.2478/amm-2014-0039**.

[3] Plesset, M.S., Prosperetti, A. (1977). Bubble dynamics and cavitation. *Annual Review of Fluid Mechanics*, vol. 9, p. 145-185, **DOI:10.1146/annurev.fl.09.010177.001045**.

[4] Philipp, A., Lauterborn, W. (1998). Cavitation erosion by single laser-produced bubbles. *Journal of Fluid Mechanics*, vol. 361, p. 75-116, **DOI:10.1017/S0022112098008738**.

[5] Lin, J., Wang, Z., Cheng, J., Kang, M., Fu, X., Hong, S. (2017). Effect of initial surface roughness on cavitation erosion resistance of arc-sprayed Fe-based amorphous/

nanocrystalline coatings. *Coatings*, vol. 7, no. 11, art. ID 200, **DOI:10.3390/coatings7110200**.

[6] Shi, Z., Wang, J., Wang, Z., Qiao, Y., Xiong, T., Zheng, Y. (2018). Cavitation erosion and jet impingement erosion behavior of the NiTi coating produced by air plasma spraying. *Coatings*, vol. 8, no. 10, art ID 346, **DOI:10.3390/coatings8100346**.

[7] Qiao, L., Wu, Y., Hong, S., Cheng, J. (2019). Ultrasonic cavitation erosion mechanism and mathematical model of HVOF sprayed Fe-based amorphous/nanocrystalline coatings. *Ultrasonics Sonochemistry*, vol. 52, p. 142-149, **DOI:10.1016/j.ultsonch.2018.11.010**.

[8] Wood, R.J.K., Herd, S., Thakare, M.R. (2018). A critical review of the tribocorrosion of cemented and thermal sprayed tungsten carbide. *Tribology International*, vol. 119, p. 491-509, **DOI:10.1016/j.triboint.2017.10.006**.

[9] Singh, J., Thakur, L., Angra, S. (2020). Abrasive wear behavior of WC-10Co-4Cr cladding deposited by TIG welding process. *International Journal of Refractory Metals and Hard Materials*, vol. 88, art. ID 105198, **DOI:10.1016/j.ijrmhm.2020.105198**.

[10] Singh, J., Thakur, L., Angra, S. (2020). An investigation on the parameter optimization and abrasive wear behaviour of nanostructured WC-10Co-4Cr TIG weld cladding. *Surface and Coating Technology*, vol. 386, art. ID 125474, **DOI:10.1016/j.surfcoat.2020.125474**.

[11] Gant, A.J., Gee, M.G. (2015). Wear modes in slurry jet erosion of tungsten carbide hard metals: their relationship with microstructure and mechanical properties. *International Journal of Refractory Metals and Hard Materials*, vol. 49, p. 192-202, **DOI:10.1016/j.ijrmhm.2014.07.036**.

[12] Gant, A.J., Morrell, R., Wronski, A.S., Jones, H.G. (2018). Edge toughness of tungsten carbide based hard metals. *International Journal of Refractory Metals and Hard Materials*, vol. 75, p. 262-278, **DOI:10.1016/j.ijrmhm.2017.12.020**.

[13] Zhang, H., Gong, Y., Chen, X., McDonald, A., Li, H. (2019). A comparative study of cavitation erosion resistance of several HVOF-sprayed coatings in deionized water and artificial seawater. *Journal of Thermal Spray Technology*, vol. 28, p. 1060-1071, **DOI:10.1007/s11666-019-00869-x**.

[14] Williamson, E.H., Gee, M., Robertson, D., Watts, J.F., Whiting, M.J., Yeomans, J.A. (2019). Wear performance and characterisation of coatings for nuclear applications: WC-(W,Cr)2C-Ni and hard chromium plate. *Wear*, vol. 430-431, p. 169-182, **DOI:10.1016/j.wear.2019.05.001**.

[15] da Silva, F.S., Cinca, N., Dosta, S., Cano, I.G., Couto, M., Guilemany, J.M., Benedetti, A.V. (2018). Corrosion behavior of WC-Co coatings deposited by cold gas spray onto AA 7075-T6. *Corrosion Science*, vol. 136, p. 231-243, **DOI:10.1016/j.corsci.2018.03.010**.

[16] Rovatti, L., Lecis, N., Dellasega, D., Russo, V., Gariboldi, E. (2018). Influence of aging in the temperature range 250-350 °C on the tribological performance of a WC-CoCr coating produced by HVOF. *International Journal of Refractory Metals and Hard Materials*, vol. 75, p. 218-224, **DOI:10.1016/j.ijrmhm.2018.04.017**.

[17] Cheng, J.B., Liang, X.B., Xu, B.S. (2013). Devitrification of arc-sprayed FeBSiNb amorphous coatings: Effects on wear resistance and mechanical behavior. *Surface and Coatings Technology*, vol. 235, p. 720-726, **DOI:10.1016/j.surfcoat.2013.08.054**.

[18] Hong, S., Lin, J., Wu, Y., Wu, J., Zheng, Y., Zhang, Y., Sun, W. (2020). Cavitation erosion characteristics at various flow velocities in NaCl medium of carbide-based cermet coatings prepared by HVOF spraying. *Ceramics International*, vol. 47, no. 2, p. 1929-1939, **DOI:10.1016/j.ceramint.2020.09.022**.

[19] Ludwig, G.A., Malfatti, C.F., Schroeder, R.M., Ferrari, V.Z., Muller, I.L. (2019). WC10Co4Cr coatings deposited by HVOF on martensitic stainless steel for use in hydraulic turbines: resistance to corrosion and slurry erosion. *Surface and Coatings Technology*, vol. 377 art. ID 124918, **DOI:10.1016/j.surfcoat.2019.124918**.

[20] Ma, N., Guo, L., Cheng, Z., Wu, H., Ye, F., Zhang, K. (2014). Improvement on mechanical properties and wear resistance of HVOF sprayed WC-12Co coatings by optimizing feedstock structure. *Applied Surface Science*, vol. 320, p. 364-371, **DOI:10.1016/j.apsusc.2014.09.081**.

[21] Ding, X., Ke, D., Yuan, C.Q., Ding, Z.X., Cheng, X.D. (2018). Microstructure and cavitation erosion resistance of HVOF deposited WC-Co coatings with different sized WC. *Coatings*, vol. 8, no. 9, art. ID 307, **DOI:10.3390/coatings8090307**.

[22] Cho, T.Y., Yoon, J.H., Kim, K.S., Song, K.O., Joo, Y.K., Fang, W., Zhang, S.H., Youn, S.J., Chun, H.G., Hwang, S.Y. (2008). A study on HVOF coatings of micron and nano WC-Co powders. *Surface and Coatings Technology*, vol. 202, no. 22-23, p. 5556-5559, **DOI:10.1016/j.surfcoat.2008.06.106**.

[23] Wang, X., Ouyang, T., Duan, X., Ke, C., Zhang, X., Min, J., Li, A., Guo, W., Cheng, X. (2017). Improved solar absorptance of WC/Co solar selective absorbing coating with multimodal WC particles. *Metals*, vol. 7, no. 4, art ID 137, **DOI:10.3390/met7040137**.

[24] Al-Mutairi, S., Hashmi, M., Yilbas, B., Stokes, J. (2015). Microstructural characterization of HVOF/plasma thermal spray of micro/nano WC–12%Co powders. *Surface and Coatings Technology*, vol. 264, p. 175-186, **DOI:10.1016/j.surfcoat.2014.12.050**.

[25] Wentzel, E.J., Allen, C. (1997). The erosion-corrosion resistance of tungsten-carbide hard metals. *International Journal of Refractory Metals and Hard Materials*, vol. 15, no. 1-3, p. 81-87, **DOI:10.1016/S0263-4368(96)00016-9**.

[26] Tyagi, A., Walia, R.S., Murtaza, Q. (2019). Tribological behavior of temperature dependent environment friendly thermal CVD diamond coating. *Diamond & Related Materials*, vol. 96, p. 148-159, **DOI:10.1016/j.diamond.2019.05.003**.

[27] Manninen, N.K., Ribeiro, F., Escudeiro, A., Polcar, T., Carvalho, S., Cavaleiro, A. (2013). Influence of Ag content on mechanical and tribological behavior of DLC coatings. *Surface and Coatings Technology*, vol. 232, p. 440-446, **DOI:10.1016/j.surfcoat.2013.05.048**.

[28] Casiraghi, C., Ferrari, A.C., Robertson, J. (2005). Raman spectroscopy of hydrogenated amorphous carbons. *Physical Review B*, vol. 72, no. 8, art. ID 085401, **DOI:10.1103/PhysRevB.72.085401**.

[29] Tyagi, A., Pandey, S.M., Gupta, K., Walia, R.S., Murtaza, O., Krishen, K. (2019). Tribological behavior of sustainable Carbon based Composite coating for wear resistance

applications. *Materials Research Express*, vol. 6, no. 12, **DOI:10.1088/2053-1591/ab52b4**.

[30] Tyagi, A., Pandey, S.M., Walia, R.S., Murtaza, Q. (2019). Characterization and parametric optimization of tribological properties of Mo blend composite coating. *Material Research Express*, vol. 6, no. 8, **DOI:10.1088/2053-1591/ab1d0a.**

[31] Matikainen, V., Koivuluoto, H., Vuoristo, P., Schubert, J., Houdková, Š. (2018). Effect of nozzle geometry on the microstructure and properties of HVAF-sprayed WC-10Co4Cr and Cr3C2-25NiCr coatings. *Journal of Thermal Spray Technology*, vol. 27, p. 680-694, **DOI:10.1007/s11666-018-0717-z**.

[32] Wu, H., Lan, X.D., Liu, Y., Li, F., Zhang, W.D., Chen, Z.J., Zai, X.F., Zeng, H. (2016). Fabrication, tribological and corrosion behaviors of detonation gun sprayed Fe-based metallic glass coating. *Transactions of Nonferrous Metals Society of China*, vol. 26, no. 6, p. 1629-1637, **DOI:10.1016/S1003-6326(16)64271-1**.

[33] Tyagi, A., Walia, R.S., Murtaza, Q. (2019). Tribological behavior of HVOF carbon coating for wear resistance applications. Materials Research Express, vol. 6, no. 12, **DOI:10.1088/2053-1591/ab555d**.

[34] Skordaris, G., Bouzakis, K.-D., Charalampous, P., Kotsanis, T., Bouzakis, E., Lemmer, O. (2016). Effect of structure and residual stresses of diamond coated cemented carbide tools on the film adhesion and developed wear mechanisms in milling. *CIRP Annals*, vol. 65, no. 1, p. 101-104, **DOI:10.1016/j.cirp.2016.04.007**.

[35] Biberger, J., Füßer, H.-J. (2017). Development of a test method for a realistic, single parameter-dependent analysis of piston ring versus cylinder liner contacts with a rotational tribometer. Tribology International, vol. 113, p. 111-124, **DOI:10.1016/j.triboint.2016.10.043**.

[36] Tyagi, A., Pandey, S.M., Murtaza, Q., Walia, R.S., Tyagi, M. (2020). Tribological behavior of carbon coating for piston ring applications using Taguchi approach. *Materials Today: Proceeding*, vol. 25, p. 759-764, **DOI:10.1016/j.matpr.2019.09.004**.

Vsebina

Strojniški vestnik - Journal of Mechanical Engineering
letnik 67, (2021), številka 4
Ljubljana, april 2021
ISSN 0039-2480

Izhaja mesečno

Razširjeni povzetki (extended abstracts)

Strojniški vestnik - Journal of Mechanical Engineering 67(2021)4, SI 21

Prejeto v recenzijo: 2021-02-22
Prejeto popravljeno: 2021-03-30
Odobreno za objavo: 2021-04-07

Študija učinkovitosti rezanja plastike, ojačene z ogljikovimi vlakni, z abrazivnim vodnim curkom

Ahmed A. Hussien[1,*] – Isam Qasem[1] – Pramodkumar S. Kataraki[2] – Wael Al-Kouz[3] – Ayub Ahmed Janvekar[4]

[1] Univerza Al-Balqa, Kolidž Al-Huson, Oddelek za strojništvo, Jordanija
[2] Univerza REVA, Šola za strojništvo, Indija
[3] Nemško-jordanska univerza, Oddelek za strojništvo in vzdrževanje, Jordanija
[4] Univerza VIT, Šola za strojništvo, Indija

Kompozitni materiali kot je plastika, ojačena z ogljikovimi vlakni (CFRP), so se v zadnjih letih močno razširili v industriji medicinskih pripomočkov, pomorstvu ter v letalski in vesoljski tehniki. Razlog je v njihovem ugodnem razmerju med mehanskimi lastnosti in maso ter v drugih lastnostih, kot sta med drugim visoka žilavost in korozijska odpornost. Mnogi raziskovalci se ukvarjajo s težavami pri obdelavi CFRP, zlasti s toplotnimi poškodbami in z nekakovostnimi površinami po obdelovalnem postopku. Kompleksnost obdelave materialov z različnimi toplotnimi in mehanskimi lastnostmi ter nehomogenost in anizotropnost pri CFRP vpliva na izbiro obdelovalnega procesa in orodij. Postopki, ki se uporabljajo za izboljševanje funkcijskih lastnosti po obdelavi CFRP, vključujejo superfiniš, konturno rezkanje, honanje, lepanje, poliranje in vrtanje. Ti postopki pa so povezani z velikimi napori in z visokimi stroški. Za rezanje visokotrdnih materialov brez toplotnih poškodb se zato pogosto uporablja tehnika rezanja z visokotlačnim abrazivnim vodnim curkom (AWJ).

Izzivi zaradi delaminacije in kakovosti površine materialov po obdelavi s tehniko abrazivnega vodnega curka so odvisni od različnih rezalnih parametrov, kot so hitrost premikanja rezalne glave, pretok in tlak vode ter orientacija in debelina kompozitnih materialov. Zato je potrebnih več raziskav za določanje optimalnega razpona teh parametrov, ki izpolnjujejo zahteve glede kakovosti površin. V tej študiji so bili uporabljeni ročno izdelani kompoziti iz plastike in ogljikovih vlaken v različnih orientacijah, ki so bili obdelani z abrazivnim vodnim curkom za analizo površinske hrapavosti in kota reže pri različnih vrednostih rezalnih parametrov, ki vključujejo hitrost premikanja rezalne glave in tlak vode.

Obdelovanec v dimenzijah 300 mm × 300 mm × 7 mm je bil izdelan iz plastike, ojačene z ogljikovimi vlakni. Vsi preizkušanci so bili izdelani z ročnim polaganjem vlaken in po metodi stiskanja. Rezanje je bilo opravljeno na stroju za razrez z abrazivnim vodnim curkom. V pričujoči študiji je bila preučena in ocenjena kakovost površine reza, izdelanega z vodnim curkom pri različnih delovnih parametrih. Preučen je bil vpliv različnih vrednosti hitrosti potovanja glave in vodnega tlaka na kot reže in na površinsko hrapavost. Za vsako meritev je bilo uporabljenih pet različnih vrednosti teh parametrov. Vrednost površinske hrapavosti Ra je bila izmerjena s prenosnim merilnikom hrapavosti RT10. V raziskavi je bil izmerjen tudi vpliv poševnosti površine reza pri različnih rezalnih parametrih.

Najmanjša vrednost *Ra* je bila ugotovljena pri največjem vodnem tlaku (200 MPa) in pri najnižji hitrosti rezalne glave (100 mm/min). Vzrok je v povečanju kinetične energije, ki je povzročilo koncentriranje lomnih sil na ogljikovih vlaknih in polimerni matrici med razmeroma dolgim rezanjem. Odvisnost med kotom reže in hitrostjo glave je sorazmerna, medtem ko je vpliv vodnega tlaka na kot reže obratno sorazmeren. Razlog za to je v povečanju hitrosti rezanja in skrajšanju kontaktnega časa med procesom rezanja in s tem v manjši delaminaciji rezanega materiala.

V prihodnjih raziskavah bo razširjen obseg eksperimentalnega dela in bo poglobljena analiza vpliva različnih parametrov procesa na kakovost površine, kot so oddaljenost rezalne glave od površine, velikost abrazivnih zrn in vrsta materiala.

V eksperimentalni študiji je bila preučena kakovost površin (hrapavost in kot reže) po obdelavi CFRP s tehniko abrazivnega vodnega curka za različne rezalne parametre, kot sta vodni tlak in rezalna hitrost.

Ključne besede: kompozitni materiali, CFRP, rezanje z abrazivnim vodnim curkom, kakovost površin, hrapavost, kot reže

*Naslov avtorja za dopisovanje: Univerza Al-Balqa, Kolidž Al-Huson, Oddelek za strojništvo, Irbid, 21110, Jordanija, ahmed.hussien@bau.edu.jo

Strojniški vestnik - Journal of Mechanical Engineering 67(2021)4, SI 22,

Prejeto v recenzijo: 2020-10-28
Prejeto popravljeno: 2021-02-01
Odobreno za objavo: 2021-02-15

HIL validacija novega realnočasovnega sistema upravljanja z energijo za HEV z brezstopenjskim menjalnikom

Amir Taghavipour* – Ali Alipour
Tehniška univerza K. N. Toosi, Fakulteta za strojništvo, Iran

Raziskovalci se v luči vplivov na okolje zaradi globalnega segrevanja ter usihanja svetovnih zalog fosilnih goriv intenzivno posvečajo rešitvam za zmanjšanje količine energije, ki se rabi za transport. Med komercialnimi rešitvami za izboljšanje učinkovitosti konvencionalnih prenosnikov moči so tudi brezstopenjski menjalniki (CVT). Nove priložnosti se odpirajo v kombiniranju menjalnikov CVT s hibridnimi električnimi prenosniki moči. Potencialna slabost tega pristopa je v zahtevnosti krmilnega sistema, ki je tudi predmet te študije. Za dodatno zmanjšanje porabe goriva pri hibridnih električnih vozilih (HEV) z menjalnikom CVT je predlagan razvoj sistema upravljanja z energijo (EMS) na osnovi prediktivnega večparametričnega modela. Tak pristop ohranja voznost in zagotavlja možnost izvedbe realnočasovnega krmilnika. Zmogljivost krmilnika je bila validirana na platformi dSPACE (HIL – strojna oprema v zanki) in z eksperimentalno preverjenim visokonatančnim modelom Autonomie omenjenega prenosnika moči za tri različne vozne cikle.

Ob upoštevanju inovativnega modela krmiljenja je bil zasnovan eksplicitni model prediktivnega vodenja za optimalno upravljanje z energijo iz različnih virov in sistematično ravnanje z omejitvami. Optimalna rešitev problema je podana s politopi sistema upravljanja z energijo in rezultati skaliranih manipuliranih vhodov v obliki afinih funkcij.

Za validacijo delovanja krmilnika so bili obravnavani trije različni vozni cikli: test porabe goriva na avtocesti (HWFET), novi evropski vozni cikel (NEDC) in globalno usklajeni preskusni postopek za lahka vozila (WLTC). Za predstavitev zmogljivosti predlaganega pristopa je bila narejena primerjava z izhodiščnim krmilnikom Autonomie.

Visokonatančni in bolj realistični model Autonomie zagotavlja realne rezultate za implementacijo predlaganega EMS. Kot je tudi pričakovano za cikel HWFET, je zmanjšanje rabe energije pri višjih hitrostih omejeno, saj je motor učinkovitejši, prehodnih pojavov je manj in podpora električnega pogona je manjša. Predlagani EMS pri mešani vožnji po mestu in avtocesti v ciklih NEDC in WLTC zagotavlja za približno 11 odstotkov manjšo porabo goriva v primerjavi z izhodiščno strategijo. Za celovitejšo primerjavo so bile pregledane tudi podobne študije. V nedavnih raziskavah je bila ugotovljena podobna poraba goriva v ciklu NEDC pri uporabi Gaussovega psevdospektralnega MPC za skrajšanje računskega časa krmilnika na enaki arhitekturi hibridnega vozila in z vrednostmi parametrov, ki so podobne kot pri naši študiji. Tukajšnji EMS pa je za razliko od omenjenega MPC mogoče implementirati v realnočasovni izvedbi in ga ustrezno zmanjšati za komercialno regulacijsko strojno opremo. Njegove zmožnosti in zmogljivost so bile validirane s preizkusi HIL v simulacijskem modelu Autonomie. Iz rezultatov je mogoče sklepati o znatnem zmanjšanju porabe goriva v primerjavi z izhodiščnim krmilnikom in omenjeno študijo. HIL analiza zagotavlja realnočasovno zmogljivost in primernost predlaganega krmilnika za izvedbo v obliki regulacijske strojne opreme. Krmilnik bo v prihodnje mogoče tudi implementirati v realnem hibridnem vozilu za izvedbo potrebnih postopkov kalibriranja.

Ključne besede: hibridno električno vozilo, CVT, Autonomie, sistem upravljanja z energijo, eksplicitno modelno prediktivno vodenje, strojna oprema v zanki

*Naslov avtorja za dopisovanje: Tehniška univerza K. N. Toosi, Fakulteta za strojništvo, Teheran, Iran, ataghavi@uwaterloo.ca

Strojniški vestnik - Journal of Mechanical Engineering 67(2021)4, SI 23

Prejeto v recenzijo: 2020-12-16
Prejeto popravljeno: 2021-03-22
Odobreno za objavo: 2021-04-07

Metoda na osnovi raztezka za ocenjevanje vzdolžne sile v pametni pnevmatiki s fizikalnim modelom

Haichao Zhou[1] – Huiyun Li[1] – Jian Yang[1,*] – Qingyun Chen[1] – Guolin Wang[1] – Tong Han[1] – Jieyu Ren[2] – Te Ma[1]

[1] Univerza Jiangsu, Šola za avtomobilsko in prometno tehniko, Kitajska
[2] Zhejiang Wanxiang Marelli Amortizerji, Kitajska

Pnevmatike niso le nepogrešljiv del vozila, temveč tudi edina komponenta vozila, ki je v stiku z voziščem. Pnevmatike imajo zato ključno vlogo pri stabilnosti krmiljenja ter pri varnosti in udobju vožnje. Vzdolžna sila v pnevmatiki, ki nastane na stiku med pnevmatiko in voziščem, lahko izboljša oprijem in zaviranje ter prispeva k smerni stabilnosti vozila. S točno oceno vzdolžne sile v pnevmatiki je mogoče izboljšati varnost vozila. Pametna pnevmatika je opremljena s senzorji, ki aktivno merijo sile in dinamične parametre pnevmatik ter nadzorujejo interakcijo med pnevmatiko in voziščem. Za izboljšanje univerzalne uporabnosti algoritma pametne pnevmatike so bile določena relacije med signali senzorjev in parametri dinamike pnevmatike na osnovi teoretičnega modela pnevmatike. Z analizo karakterističnih sprememb senzorskega signala je bil razvit ocenjevalni algoritem pametne pnevmatike za realnočasovni nadzor sil v pnevmatiki.

V članku je najprej predstavljen model longitudinalne dinamike pnevmatike na osnovi modela upogljivega obroča in modela krtače. Nato so določene deformacije in raztezki obroča pri različnih vertikalnih in vzdolžnih silah. Radialne deformacije visokotrdne karkase pnevmatike zaradi njene neraztegljivosti ne povzročijo le tangencialne deformacije, ampak tudi obodne napetosti in raztezke. Vzdolžna sila je glavni vzrok za asimetrično porazdelitev radialne deformacije in obodnega raztezka pnevmatike. Večja ko je vzdolžna sila, večja je asimetrija radialne deformacije in obodnega raztezka. Za kvantitativni opis te asimetrije je predlagana razlika v radialni deformaciji in obodnem raztezku med prednjimi in zadnjimi območji. Za preučevanje vplivov vzdolžne sile na deformacijo in raztezek pnevmatike je predlagana uporaba ploščine pod krivuljo razlik radialne deformacije in ploščine pod krivuljo razlik obodnega raztezka.

Rezultati kažejo močno linearno odvisnost med ploščino pod krivuljo razlik radialne deformacije oz. ploščino pod krivuljo razlik obodnih raztezkov in vzdolžnimi silami v pnevmatikah pri različnih vertikalnih obremenitvah in razmerjih spodrsavanja. Ploščino pod krivuljo razlik radialne deformacije in ploščino pod krivuljo razlik obodnih raztezkov je mogoče uporabiti za oceno vzdolžne sile, ki deluje na pnevmatiko. Za določitev relacije med obodnim raztezkom pnevmatike in vzdolžno silo je bil razvit model pametne pnevmatike na osnovi raztezka, ki omogoča ocenjevanje vzdolžne sile. Z razvitim modelom vzdolžne dinamike so bile preučene lastnosti raztezkov pnevmatike v pogojih čistega vzdolžnega spodrsavanja. Razvit je bil algoritem za ocenjevanje vzdolžne sile v pnevmatiki s pridobivanjem značilk in prileganjem podatkov o raztezku pnevmatike. Postavljen je bil tudi model pnevmatike s končnimi elementi za simulacijo vzdolžne sile. Primerjava simuliranih in ocenjenih sil kaže, da lahko predlagani algoritem natančno napove vzdolžno silo v pametnih pnevmatikah in tako zagotavlja uporabne informacije za sisteme upravljanja stabilnosti vozila.

Inovacija tega prispevka je v uporabi modelne analize vzdolžne dinamike tankega obroča za določitev fizikalne veličine, na katero vpliva le vzdolžna sila, ter v določitvi metode za ocenjevanje vzdolžne sile v pametni pnevmatiki. Algoritem ima manj identifikacijskih parametrov in je primeren za različne modele pnevmatik oz. je univerzalno uporaben. Zaradi kompleksnosti sistema pnevmatike pa obstajajo možna področja izboljšav: model pnevmatike v članku ne upošteva vpliva prečne sile, zato ni mogoče določiti relacij med indeksom ocene vzdolžne sile in prečno silo. Zato bo mogoče postaviti še tridimenzionalni model pnevmatike za dodatno analizo signala raztezka. Verifikacija algoritma v članku poleg tega temelji le na analitičnem modelu pnevmatike po metodi končnih elementov. V prihodnjih raziskavah bo algoritem še dodatno verificiran z eksperimentalnimi podatki, določen pa bo tudi položaj senzorja raztezka.

Ključne besede: pametna pnevmatika, model pnevmatike, analiza raztezkov, vzdolžna sila, ocena sile

*Naslov avtorja za dopisovanje: Univerza Jiangsu, Šola za avtomobilsko in prometno tehniko, Kitajska, yangjian@ujs.edu.cn

Strojniški vestnik - Journal of Mechanical Engineering 67(2021)4, SI 24,

Prejeto v recenzijo: 2021-01-23
Prejeto popravljeno: 2021-02-21
Odobreno za objavo: 2021-03-22

Optimizacija energijske učinkovitosti in površinskih lastnosti pri notranjem glajenju

Trung-Thanh Nguyen[1] – Minh-Thai Le[2,*]

[1] Tehniška univerza Le Quy Don, Fakulteta za strojništvo, Vietnam
[2] Tehniška univerza Le Quy Don, Fakulteta za posebno opremo, Vietnam

Cilj predstavljenega dela je optimizacija vplivnih dejavnikov pri notranjem glajenju – hitrosti vretena, podajanja, globine penetracije in števila valjčkov – za najmanjšo rabo energije, najmanjšo hrapavost obdelanih površin in največjo trdoto po Rockwellu.

Glajenje je ekonomičen in učinkovit obdelovalni postopek za izboljšanje lastnosti površin. Izboljševanje kakovosti površin po glajenju je tudi predmet večine objavljenih raziskav. Zaradi visokih stroškov in težavnosti dela pa še ni objavljenih analiz o kompromisih med rabo energije in lastnostmi površine pri notranjem glajenju.

Za ugotavljanje korelacij med vhodi procesa in odgovori pri glajenju je bil uporabljen adaptivni nevro-mehki inferenčni sistem (ANFIS). Za določitev optimalnih parametrov je bila uporabljena optimizacija z rojem delcev z nedominantnim razvrščanjem (NSPSO).

Glavne ugotovitve so:

- Predstavljeni pristop predstavlja zanimivo tehnično rešitev za izboljševanje zmogljivosti procesa glajenja različnih komponent z notranjimi luknjami.
- Optimalna rešitev je pomagala pri zmanjšanju rabe energije za 16,3 %, zmanjšanju površinske hrapavosti za 24,3 % in povečanju trdote po Rockwellu za 4,0 % v primerjavi z izhodiščnimi vrednostmi.

V tem prispevku niso predstavljeni vplivi parametrov glajenja na preostale napetosti, globino prizadetega sloja in na stroške obdelave. V prihodnjih raziskavah bo zato opravljena izčrpnejša optimizacija zmogljivosti obdelave.

Glavni prispevki in vrednost raziskave so:

- Predlagani pristop k optimizaciji z metodama ANFIS in NOPSO je mogoče uporabiti za reševanje optimizacijskih problemov pri različnih gladilnih operacijah in materialih.
- Znanstvene ugotovitve bo mogoče učinkovito uporabiti v prihodnjih raziskavah za optimizacijo operacij glajenja ali za razvoj ekspertnih sistemov za glajenje.
- Optimalne rezultate, pridobljene s pristopom ANFIS-NOPSO, bo mogoče uporabiti za izboljšanje tehničnih parametrov pri notranjem glajenju jekla 40X.

Ključne besede: notranje glajenje, raba energije, površinska hrapavost, trdota po Rockwellu, optimizacija

*Naslov avtorja za dopisovanje: Tehniška univerza Le Quy Don, 236 Hoang Quoc Viet, Ha Noi, Vietnam, thaileminh@lqdtu.edu.vn

Strojniški vestnik - Journal of Mechanical Engineering 67(2021)4, SI 25

Prejeto v recenzijo: 2021-01-21
Prejeto popravljeno: 2021-02-25
Odobreno za objavo: 2021-03-29

Konstruiranje ekstrudorja s podaljšanim grlom za večosno 3D-tiskanje FDM

Hao Liu[1*] – Zhoupeng Liu[1,*] – Siting Hao[2]

[1] Univerza za aeronavtiko in astronavtiko v Nanjingu, Kolidž za strojništvo in elektroniko, Kitajska
[2] Tehniška univerza v Tianjinu, Kolidž za strojništvo, Kitajska

Tehnologija večosnega 3D-tiskanja FDM je v zadnjem času pritegnila veliko zanimanja. Obstoječi ekstrudorji pa so običajno kratki in debeli, kar omejuje možnosti širjenja tehnologije večosnega 3D-tiskanja FDM. Eden od pomembnih trendov pri dodajalni izdelavi je namreč uporaba dolgih in tankih ekstrudorjev, ki preprečujejo trke med ekstrudorjem in obdelovanci med tiskanjem.

V članku je predstavljena konstrukcija ekstrudorja za FDM s podaljšanim vratom, ki omogoča tiskanje delov kompleksnih oblik in detajlov. Zanjo so značilni podaljšan vrat, zmanjšanje velikosti grelnika in vgradnja novega miniaturnega ventilatorja za ekstrudor. Na vročem delu grla so izdelane toplotne pregrade, ki preprečujejo prenos toplote. Na grelnik so prilepljeni trakovi toplotne izolacije.

Predstavljena je metoda toplotne numerične analize za optimizacijo velikosti in oblike toplotnih pregrad, hitrosti zračnega toka mini ventilatorja in števila slojev trakov toplotne izolacije za čim večjo temperaturno razliko vzdolž grla. Numerična analitična metoda razrešuje problem prenosa toplote na stiku tekoče in trdne snovi, kombinira pa računalniško dinamiko fluidov (CFD) za tok zraka v okolici in analizo temperaturnega polja grelnega bloka s končnimi elementi (FEA). Zasnovana je bila eksperimentalna metoda za preverjanje učinkovitosti metode FEA z meritvijo temperature v nadzornih točkah na grlu pri danih delovnih pogojih.

Predstavljen je ekstrudor s podaljšanim grlom, s katerim lahko 5-osni tiskalnik FDM natisne več detajlov in obloži kompleksnejše površine. Za razliko od konvencionalnih ekstrudorjev filamenta za FDM ima ekstrudor s podaljšanim grlom manjši grelni blok s trakovi toplotne izolacije, podaljšano grlo šobe s toplotnimi pregradami in hladilno opremo z nastavljivo hitrostjo zračnega toka. Ekstrudor je bil vgrajen v 5-osni tiskalnik FDM. S tiskalnikom in različnimi vrstami šob je bilo natisnjenih več obdelovancev kompleksnih oblik. Eksperimenti so pokazali, da novi ekstrudor zanesljivo deluje v 5-osnem tiskalniku FDM z različnimi šobami. Izdela lahko različne dele, ki jih s konvencionalnimi ekstrudorji FDM ni mogoče natisniti.

Glavni prispevki pričujočega članka so:

(i) predstavitev nove konstrukcije ekstrudorja s podaljšanim grlom, manjšim grelnim blokom in mini hladilnim ventilatorjem;
(ii) konstruiranje optimiziranega bloka, ki zasede čim manj prostora, z omejitvami na osnovi oblike komponent bloka in rezkalnega orodja;
(iii) zasnova eksperimentalnih in simulacijskih metod za preučitev porazdelitve temperature na grlu za optimizacijo oblike toplotnih pregrad na grlu šob in hitrosti vetra, ki ga ustvarja hladilni ventilator.

Ključne besede: 3D-tiskanje, FDM, ekstrudor, konstruiranje, večosni, grlo

*Naslov avtorja za dopisovanje: Univerza za aeronavtiko in astronavtiko v Nanjingu, Kolidž za strojništvo in elektroniko, 054 Department, No.29 Yudao Street, Nanjing, Kitajska, liuhao-01@nuaa.edu.cn, liuzhoupenga@nuaa.edu.cn

Strojniški vestnik - Journal of Mechanical Engineering 67(2021)4, SI 26

Prejeto v recenzijo: 2021-01-21
Prejeto popravljeno: 2021-02-25
Odobreno za objavo: 2021-03-29

Preostale napetosti, korozijske in tribološke lastnosti trajnostne temperaturno odvisne hibridne kompozitne prevleke na osnovi ogljika, nanesene z visokohitrostnim plamenskim nabrizgavanjem

Ankit Tyagi[1, 2*], Qasim Murtaza[1], Ravinderjit Singh Walia[3]
[1]Oddelek za strojništvo, DTU, Delhi, Indija
[2]Oddelek za strojništvo, Univerza SGT, Haryana, Indija
[3]Oddelek za proizvodni in industrijski inženiring, PEC, Chandigarh, Indija

V današnjem svetu obstaja veliko povpraševanje po cenovno ugodnih prevlekah, ki bi manj obremenjevale okolje. Za zmanjšanje tornih izgub so bile preizkušene hibridne kompozitne prevleke na osnovi ogljika, nanesene po postopku visokohitrostnega plamenskega nabrizgavanja (HVOF). Mikrostrukturne, tribološke, korozijske in mehanske lastnosti novih prevlek so bile okarakterizirane z visokoločljivostno rentgensko difrakcijo (HRXRD), vrstičnim elektronskim mikroskopom s poljsko emisijo – energijsko disperzivno rentgensko spektroskopijo (FESEM-EDS), ramansko spektroskopijo, preizkusi mikrotrdote po Vickersu, μ-360 cos (α) analizatorjem preostalih napetosti, preizkusi korozije in visokotemperaturnim tribometrom. Preostale napetosti, korozijske in tribološke lastnosti pri povišanih temperaturah so bile preučene z visokotemperaturnim tribometrom vrste valjček na disku. Na posnetkih FESEM pri povečavah ×1000 in ×500 so jasno vidne strukture v obliki lusk, kakor tudi na pol raztaljena, raztaljena in neraztaljena zrna kompozitnih delcev ter oblikovanje lamel. Na izdelanih prevlekah so bili ugotovljeni izraženi vrhovi pri 2Θ = 26° do 27°, 2Θ = 35° do 36° in 2Θ = 48° do 48,5°.

Rezultati analize HRXRD potrjujejo oblikovanje karbidnih, oksidnih in sulfidnih faz v prevlekah [26]. Vrhovi ramanskih spektrov na hibridnih kompozitnih prevlekah imajo izražene vrhove pri 1120 cm^{-1} do 1140 cm^{-1}, 1340 cm^{-1} do 1360 cm^{-1} in 1550 cm^{-1} do 1590 cm^{-1}. Rezultati eksperimentalne preiskave trdote prevlek so pokazali, da se trdota v testnih pogojih pri povišanju temperature s 50 na 350 °C, sile s 60 na 90 N in drsne hitrosti z 0,1 m/s na 0,4 m/s hitro poveča s 380 HV na 680 HV. Rezultati eksperimentalne preiskave preostalih napetosti so pokazali, da se v testnih pogojih pri povišanju temperature s 50 °C na 350 °C, sile s 60 N na 90 N in drsne hitrosti z 0,1 m/s na 0,4 m/s preostale napetosti hitro zmanjšajo z –50 MPa na –11 MPa. Tribološke lastnosti so bile okarakterizirane z visokotemperaturnim tribometrom. Rezultati kažejo spremenljive vrednosti količnika trenja od 0,12 do 0,52. Vrednost obrabe je znašala od 45 μm do 120 μm v testnih pogojih s temperaturami od 50 °C do 350 °C, silami od 60 N do 90 N in drsnimi hitrostmi od 0,1 m/s do 0,4 m/s.

Rezultati korozijskih preizkusov so pokazali zmanjšanje masne izgube v območju od 0,10 g do 0,04 g po tem, ko so bili preizkušanci potopljeni 1 h. Ko so bili preizkušanci potopljeni 8 h, se je masna izguba hibridne kompozitne prevleke spreminjala v območju med 0,12 g in 0,045 g. Tribološki testi so pokazali 78,9 %-no povečanje mikrotrdote, 78 %-no zmanjšanje preostalih napetosti, 60 %-no oz. 62,5 %-no zmanjšanje masne izgube zaradi korozije po 1 h in 8 h, 76,9 %-no zmanjšanje količnika trenja in 62,5 %-no zmanjšanje obrabe pri temperaturi 350 °C, drsni hitrosti 0,4 m/s in sili 90 N.

Ključne besede: visokohitrostno plamensko nabrizgavanje ogljikove prevleke, vrstična elektronska mikroskopija s poljsko emisijo, visokoločljivostna rentgenska difrakcija, ramanska spektroskopija, korozija, test obrabe

*Naslov avtorja za dopisovanje: Oddelek za strojništvo, DTU, Delhi, India, tyagiankit10506@yahoo.com

Guide for Authors

All manuscripts must be in English. Pages should be numbered sequentially. The manuscript should be composed in accordance with the Article Template given above. The maximum length of contributions is 12 pages (approx. 5000 words). Longer contributions will only be accepted if authors provide justification in a cover letter. For full instructions see the Information for Authors section on the journal's website: http://en.sv-jme.eu .

SUBMISSION:

Submission to SV-JME is made with the implicit understanding that neither the manuscript nor the essence of its content has been published previously either in whole or in part and that it is not being considered for publication elsewhere. All the listed authors should have agreed on the content and the corresponding (submitting) author is responsible for having ensured that this agreement has been reached. The acceptance of an article is based entirely on its scientific merit, as judged by peer review. Scientific articles comprising simulations only will not be accepted for publication; simulations must be accompanied by experimental results carried out to confirm or deny the accuracy of the simulation. Every manuscript submitted to the SV-JME undergoes a peer-review process.

The authors are kindly invited to submit the paper through our web site: http://ojs.sv-jme.eu. The Author is able to track the submission through the editorial process - as well as participate in the copyediting and proofreading of submissions accepted for publication - by logging in, and using the username and password provided.

SUBMISSION CONTENT:

The typical submission material consists of:

- A **manuscript** (A PDF file, with title, all authors with affiliations, abstract, keywords, highlights, inserted figures and tables and references),
- Supplementary files:
  - a **manuscript** in a WORD file format
  - a **cover letter** (please see instructions for composing the cover letter)
  - a ZIP file containing **figures** in high resolution in one of the graphical formats (please see instructions for preparing the figure files)
  - possible **appendicies** (optional), cover materials, video materials, etc.

Incomplete or improperly prepared submissions will be rejected with explanatory comments provided. In this case we will kindly ask the authors to carefully read the Information for Authors and to resubmit their manuscripts taking into consideration our comments.

COVER LETTER INSTRUCTIONS:

Please add a **cover letter** stating the following information about the submitted paper:

1. Paper **title**, list of **authors** and their **affiliations**. **One** corresponding author should be provided.
2. **Type of paper**: original scientific paper (1.01), review scientific paper (1.02) or short scientific paper (1.03).
3. A **declaration** that neither the manuscript nor the essence of its content has been published in whole or in part previously and that it is not being considered for publication elsewhere.
4. State the **value of the paper** or its practical, theoretical and scientific implications. What is new in the paper with respect to the state-of-the-art in the published papers? Do not repeat the content of your abstract for this purpose.
5. We kindly ask you to suggest at least two **reviewers** for your paper and give us their names, their full affiliation and contact information, and their scientific research interest. The suggested reviewers should have at least two relevant references (with an impact factor) to the scientific field concerned; they should not be from the same country as the authors and should have no close connection with the authors.

FORMAT OF THE MANUSCRIPT:

The manuscript should be composed in accordance with the Article Template. The manuscript should be written in the following format:

- A **Title** that adequately describes the content of the manuscript.
- A list of **Authors** and their **affiliations**.
- An **Abstract** that should not exceed 250 words. The Abstract should state the principal objectives and the scope of the investigation, as well as the methodology employed. It should summarize the results and state the principal conclusions.
- 4 to 6 significant **key words** should follow the abstract to aid indexing.
- 4 to 6 **highlights;** a short collection of bullet points that convey the core findings and provide readers with a quick textual overview of the article. These four to six bullet points should describe the essence of the research (e.g. results or conclusions) and highlight what is distinctive about it.
- An **Introduction** that should provide a review of recent literature and sufficient background information to allow the results of the article to be understood and evaluated.
- A **Methods** section detailing the theoretical or experimental methods used.
- An **Experimental section** that should provide details of the experimental set-up and the methods used to obtain the results.
- A **Results** section that should clearly and concisely present the data, using figures and tables where appropriate.
- A **Discussion** section that should describe the relationships and generalizations shown by the results and discuss the significance of the results, making comparisons with previously published work. (It may be appropriate to combine the Results and Discussion sections into a single section to improve clarity.)
- A **Conclusions** section that should present one or more conclusions drawn from the results and subsequent discussion and should not duplicate the Abstract.
- **Acknowledgement** (optional) of collaboration or preparation assistance may be included. Please note the source of funding for the research.
- **Nomenclature** (optional). Papers with many symbols should have a nomenclature that defines all symbols with units, inserted above the references. If one is used, it must contain all the symbols used in the manuscript and the definitions should not be repeated in the text. In all cases, identify the symbols used if they are not widely recognized in the profession. Define acronyms in the text, not in the nomenclature.
- **References** must be cited consecutively in the text using square brackets [1] and collected together in a reference list at the end of the manuscript.
- **Appendix(-icies)** if any.

SPECIAL NOTES

Units: The SI system of units for nomenclature, symbols and abbreviations should be followed closely. Symbols for physical quantities in the text should be written in italics (e.g. *v*, *T*, *n*, etc.). Symbols for units that consist of letters should be in plain text (e.g. ms^{-1}, K, min, mm, etc.). Please also see: http://physics.nist.gov/cuu/pdf/sp811.pdf .

Abbreviations should be spelt out in full on first appearance followed by the abbreviation in parentheses, e.g. variable time geometry (VTG). The meaning of symbols and units belonging to symbols should be explained in each case or cited in a **nomenclature** section at the end of the manuscript before the References.

Figures (figures, graphs, illustrations digital images, photographs) must be cited in consecutive numerical order in the text and referred to in both the text and the captions as Fig. 1, Fig. 2, etc. Figures should be prepared without borders and on white grounding and should be sent separately in their original formats. If a figure is composed of several parts, please mark each part with a), b), c), etc. and provide an explanation for each part in Figure caption. The caption should be self-explanatory. Letters and numbers should be readable (Arial or Times New Roman, min 6 pt with equal sizes and fonts in all figures). Graphics (submitted as supplementary files) may be exported in resolution good enough for printing (min. 300 dpi) in any common format, e.g. TIFF, BMP or JPG, PDF and should be named Fig1.jpg, Fig2.tif, etc. However, graphs and line drawings should be prepared as vector images, e.g. CDR, AI. Multi-curve graphs should have individual curves marked with a symbol or otherwise provide distinguishing differences using, for example, different thicknesses or dashing.

Tables should carry separate titles and must be numbered in consecutive numerical order in the text and referred to in both the text and the captions as Table 1, Table 2, etc. In addition to the physical quantities, such as *t* (in italics), the units [s] (normal text) should be added in square brackets. Tables should not duplicate data found elsewhere in the manuscript. Tables should be prepared using a table editor and not inserted as a graphic.

REFERENCES:

A reference list must be included using the following information as a guide. Only cited text references are to be included. Each reference is to be referred to in the text by a number enclosed in a square bracket (i.e. [3] or [2] to [4] for more references; do not combine more than 3 references, explain each). No reference to the author is necessary.

References must be numbered and ordered according to where they are first mentioned in the paper, not alphabetically. All references must be complete and accurate. Please add DOI code when available. Examples follow.

Journal Papers:

Surname 1, Initials, Surname 2, Initials (year). Title. Journal, volume, number, pages, DOI code.

[1] Hackenschmidt, R., Alber-Laukant, B., Rieg, F. (2010). Simulating nonlinear materials under centrifugal forces by using intelligent cross-linked simulations. *Strojniški vestnik - Journal of Mechanical Engineering*, vol. 57, no. 7-8, p. 531-538, DOI:10.5545/sv-jme.2011.013.

Journal titles should not be abbreviated. Note that journal title is set in italics.

Books:

Surname 1, Initials, Surname 2, Initials (year). Title. Publisher, place of publication.

[2] Groover, M.P. (2007). *Fundamentals of Modern Manufacturing*. John Wiley & Sons, Hoboken.

Note that the title of the book is italicized.

Chapters in Books:

Surname 1, Initials, Surname 2, Initials (year). Chapter title. Editor(s) of book, book title. Publisher, place of publication, pages.

[3] Carbone, G., Ceccarelli, M. (2005). Legged robotic systems. Kordić, V., Lazinica, A., Merdan, M. (Eds.), Cutting Edge Robotics. Pro literatur Verlag, Mammendorf, p. 553-576.

Proceedings Papers:

Surname 1, Initials, Surname 2, Initials (year). Paper title. Proceedings title, pages.

[4] Štefanić, N., Martinčević-Mikić, S., Tošanović, N. (2009). Applied lean system in process industry. *MOTSP Conference Proceedings*, p. 422-427.

Standards:

Standard-Code (year). Title. Organisation. Place.

[5] ISO/DIS 16000-6.2:2002. *Indoor Air – Part 6: Determination of Volatile Organic Compounds in Indoor and Chamber Air by Active Sampling on TENAX TA Sorbent, Thermal Desorption and Gas Chromatography using MSD/FID*. International Organization for Standardization. Geneva.

WWW pages:

Surname, Initials or Company name. Title, from http://address, date of access.

[6] Rockwell Automation. Arena, from *http://www.arenasimulation.com*, accessed on 2009-09-07.

EXTENDED ABSTRACT:

When the paper is accepted for publishing, the authors will be requested to send an **extended abstract** (approx. one A4 page or 3500 to 4000 characters or approx. 600 words). The instruction for composing the extended abstract are published on-line: http://www.sv-jme.eu/information-for-authors/ .

COPYRIGHT:

Authors submitting a manuscript do so on the understanding that the work has not been published before, is not being considered for publication elsewhere and has been read and approved by all authors. The submission of the manuscript by the authors means that the authors automatically agree to transfer copyright to SV-JME when the manuscript is accepted for publication. All accepted manuscripts must be accompanied by a Copyright Transfer Agreement, which should be sent to the editor. The work should be original work by the authors and not be published elsewhere in any language without the written consent of the publisher. The proof will be sent to the author showing the final layout of the article. Proof correction must be minimal and executed quickly. Thus it is essential that manuscripts are accurate when submitted. Authors can track the status of their accepted articles on http://en.sv-jme.eu/.

PUBLICATION FEE:

Authors will be asked to pay a publication fee for each article prior to the article appearing in the journal. However, this fee only needs to be paid after the article has been accepted for publishing. The fee is 380 EUR (for articles with maximum of 6 pages), 470 EUR (for articles with maximum of 10 pages), plus 50 EUR for each additional page. The additional cost for a color page is 90.00 EUR (only for a journal hard copy; optional upon author's request). These fees do not include tax.

Strojniški vestnik -Journal of Mechanical Engineering
Aškerčeva 6, 1000 Ljubljana, Slovenia, e-mail: info@sv-jme.eu

9 770039 248001
ISSN 0039-2480

http://www.sv-jme.eu

Contents

Papers